Large-scale circuit reconstruction in medial entorhinal cortex

D i s s e r t a t i o n

zur Erlangung des akademischen Grades

D o c t o r r e r u m n a t u r a l i u m

(Dr. rer. nat.)

im Fach Biologie

eingereicht an der

Lebenswissenschaftlichen Fakultät

der Humboldt-Universität zu Berlin

von

M.Sc., Helene Schmidt-Helmstaedter, geb. Schmidt

Präsidentin der Humboldt-Universität zu Berlin

Prof. Dr.-Ing. Dr. Sabine Kunst

Dekan der Lebenswissenschaftlichen Fakultät

Prof. Dr. Bernhard Grimm

Gutachter/innen:

1. Prof. Dr. Michael Brecht
2. Prof. Dr. Dietmar Schmitz
3. Prof. Dr. Richard Kempter

Tag der mündlichen Prüfung: 16. April 2018

To my parents

and my children, Johanna and Jakob.

Abstract

The mechanisms by which the electrical activity of ensembles of neurons in the brain give rise to an individual's behavior are still largely unknown. Navigation in space is one important capacity of the brain, for which the medial entorhinal cortex (MEC) is a pivotal structure in mammals. At the cellular level, neurons that represent the surrounding space in a grid-like fashion have been identified in MEC. These so-called grid cells are located predominantly in layer 2 of the MEC. The detailed neuronal circuits underlying this unique activity pattern are still poorly understood.

This thesis comprises a group of studies contributing to a mechanistic description of the synaptic architecture in layer 2 of the MEC in rat. First, this thesis describes the discovery of hexagonally arranged cell clusters. Furthermore, anatomical data on the dichotomy of the two principle cell types in layer 2 of the MEC is presented.

In the second part of this thesis, the first connectomic study of the MEC is reported which provides a detailed picture of the circuit structure in MEC layer 2. An analysis of the axonal architecture of excitatory neurons revealed synaptic positional sorting along axons, integrated into precise microcircuits. These microcircuits were found to involve interneurons with a surprising degree of axonal specialization for effective and fast inhibition.

Together, these results contribute to a detailed understanding of the circuitry in MEC. They provide the first description of highly precise synaptic arrangements along axons in the cerebral cortex of mammals. The functional implications of these anatomical features were explored using numerical simulations, suggesting effects on the propagation of synchronous activity in layer 2 of the MEC. These findings motivate future investigations to clarify the contribution of precise synaptic architecture to computations underlying spatial navigation. Further studies are required to understand whether the reported synaptic specializations are specific for the MEC or represent a general wiring principle in the mammalian cortex.

Zusammenfassung

Es ist noch immer weitgehend ungeklärt, mittels welcher Mechanismen die elektrische Aktivität von Nervenzellpopulationen des Gehirns Verhalten ermöglicht. Die Orientierung im Raum ist eine wichtige Fähigkeit des Gehirns, für die im Säugetier der mediale entorhinale Teil der Großhirnrinde als entscheidende Struktur identifiziert wurde. Hier wurden Nervenzellen gefunden, die die Umgebung des Individuums in einer gitterartigen Anordnung repräsentieren. Diese sogenannten Gitterzellen befinden sich hauptsächlich in der zweiten kortikalen Schicht des medialen entorhinalen Kortex (MEK). Die genauen neuronalen Schaltkreise, welche diese einzigartige geordnete Nervenzellaktivität ermöglichen, sind noch wenig verstanden.

Die vorliegende Dissertationsarbeit umfasst eine Reihe von Studien, die eine Klärung der zellulären Architektur und der neuronalen Schaltkreise in der zweiten Schicht des MEK der Ratte zum Ziel haben. Zum ersten hat diese Arbeit zur Entdeckung der hexagonal angeordneten zellulären Anhäufungen in Schicht 2 des MEK beigetragen. Weiterhin wurden anatomische Daten zur Dichotomie der Haupt-Nervenzelltypen erhoben.

Im zweiten Teil dieser Arbeit wird erstmalig eine konnektomische Analyse des MEK beschrieben. Die detaillierte Untersuchung der Architektur einzelner exzitatorischer Axone ergab das überraschende Ergebnis der präzisen Sortierung von Synapsen entlang axonaler Pfade. Im Weiteren wurden die neuronalen Schaltkreise, in denen diese Neurone eingebettet sind, studiert. Interessanterweise zeigte sich hier eine starke zeitliche Bevorzugung der hemmenden Neurone.

Im Ergebnis tragen die hier erhobenen Daten zu einem detaillierteren Verständnis der neuronalen Schaltkreise im MEK bei. Im Besonderen enthalten sie die erste Beschreibung überraschend präziser axonaler synaptischer Ordnung – einer Schaltkreispräzision, die für den zerebralen Kortex der Säugetiere nicht zu erwarten war. Die möglichen funktionellen Konsequenzen dieser Schaltkreisarchitektur wurden mittels numerischer Simulationen exploriert und lassen einen Effekt auf die Weiterleitung synchroner elektrischer Populationsaktivität im MEK vermuten. Diese Erkenntnisse legen den Grundstein für weitere Studien, um die Bedeutung präziser neuronaler Schaltkreise für die räumliche Orientierung zu bestimmen. Insbesondere muss geklärt werden, ob es sich um eine Besonderheit des MEK oder ein generelles Verschaltungsprinzip der Hirnrinde des Säugetiers handelt.

Table of Contents

Abbreviations

AChE	Acatylcholinesterase
AP	Action potential
ATUM-SEM	Automated tape-collecting ultramicrotome scanning electron microscopy
BDA	Biotynilated-Dextrane Amine
BSA	Bovine Serum Albumin
C	Caudal
CB	Calbindin
CCK	Cholecystokinin
cFFI	Cellular Feed-Forward Inhibition
CS	Saline Solution
CTB	Cholera Toxin Subunit B
D	Dorsal
DAB	Diaminobenzidine
EM	Electron Microscopy
EPSP	Excitatory Postsynaptic Potential
ExN	Excitatory Neuron
FFI	Feed-Forward Inhibition
FIB-SEM	Focused Ion Beam Milling Scanning Electron Microscopy
GABA	Gamma-Aminobutyric Acid
IN	Interneuron
IPSP	Inhibitory Postsynaptic Potential
L	Lateral
L2, L3, L5	Cortical layers 2,3,5
LEC	Lateral Entorhinal Cortex
M	Medial
MEC	Medial Entorhinal Cortex
MT	Motor Tile
NA	Numerical Aperture
PaS	Parasubiculum
PB	Phosphate Buffer
PFA	Paraformaldehyde
Per	Perirhinal Cortex

pFFI	Population Feed-Forward Inhibition
PLASS	Path Length-Dependent Axonal Synapse Sorting
Por	Postrhinal Cortex
PrS	Presubiculum
PSD	Postsynaptic Density
R	Rostral
ROI	Region Of Interest
RT	Room Temperature
SBEM	Serial Block-Face Scanning Electron Microscopy
s.d.	Standard deviation
SEM	Scanning Electron Microscopy
ssTEM	Serial Section Transmission Electron Microscopy
Sub	Subiculum
TEM	Transmission Electron Microscopy
V	Ventral
VAChT	Vesicular Acetylcholine Transporter

List of Figures

1 General Introduction

Research over the decades has provided substantial information about the molecular and cellular building blocks of the brain. Neurons are the fundamental building units, which transmit information via action potentials, and communicate with each other through chemical or electrical synapses. The morphology of neurons (Peters and Jones, 1984a; Petilla Interneuron Nomenclature et al., 2008; Ramón y Cajal, 1899, 1995), electrical processes of action potential initiation and propagation (Hausser et al., 1995; Hodgkin and Huxley, 1952; Stuart et al., 1997), temporal dynamics of synapses (Fatt and Katz, 1950; Markram et al., 1997b), and dendritic linear or non-linear integration of postsynaptic potentials (Larkum et al., 2009; Larkum et al., 1999; Nevian et al., 2007; Smith et al., 2013; Stuart and Sakmann, 1994). Powerful methods exist to record electrical activity (Brecht and Sakmann, 2002c; Lee et al., 2006; Margrie et al., 2002; Stuart et al., 1993; Tang et al., 2014a) and calcium transients in single cells (Denk et al., 1990; Helmchen et al., 2001; Murayama et al., 2007; Svoboda et al., 1996) as well as population of neurons (Garaschuk et al., 2000; Grewe et al., 2010; Kerr et al., 2005; Komiyama et al., 2010; Mittmann et al., 2011). Despite this anatomical and electrophysiological knowledge, information about circuit structure and an understanding of how the computations that the cerebral cortex performs actually work is still lacking in most cases (Denk et al., 2012).

1.1 Neuronal circuits

From the earliest studies of the cerebral cortex, researchers have been trying to represent components of the brain and their possible synaptic connections in more or less simplified wiring diagrams (Binzegger et al., 2004; Douglas et al., 1989; Felleman and Van Essen, 1991; Lorente de No, 1922, 1992; Lorente de Nó, 1938; Ramón y Cajal, 1899). The

mammalian brain comprises a large number of neurons that are heavily interconnected through chemical synapses to thousands of partner neurons (1 mm^3 of mouse cortex contains about 90.000 neurons, 3 km axons, 300 m dendrites and 700 million synapses, (Braitenberg and Schüz, 1998; Schuz and Palm, 1989), forming neuronal networks with a large number of possible configurations.

Approaches to study the anatomical organization of the cortex range from the macroscopic to the microscopic: from studies of the whole brain (e.g. magnetic resonance imaging or neurotracing methods) to investigations of local circuits (dense reconstruction using electron microscopy).

At the coarse level, light microscopic (LM) methods and neuroanatomical tracers are used to map projection-based connectivity between different brain areas without the possibility of visualizing the underlying synaptic contacts. Specific labeling methods (intracellular labeling by electrode penetration (Feldmeyer et al., 1999; Horikawa and Armstrong, 1988), juxtacellular electroporation (Bonnot et al., 2005; de Kock et al., 2007; Judkewitz et al., 2009; Kitamura et al., 2008; Nevian and Helmchen, 2007; Pinault, 1996), viral vectors (e.g., (Marshel et al., 2010)), transgenic expression of GFP in restricted neuronal types (e.g., (Feng et al., 2000; Okabe et al., 1997)) allow the investigation of cell assemblies with common characteristics (for example a common source or target of axonal projection; or the common expression of proteins or neurotransmitters). Several initiatives, such as the Mouse Brain Architecture Project (http://brainarchitecture.org/) or the Allen Mouse Brain Connectivity Atlas (http://connectivity.brain-map.org/), use these methods to reconstruct efferent and afferent pathways between cortical and subcortical neuronal assemblies of millions of neurons each within the whole mouse brain. However, these approaches are not sufficient to resolve the direct communication between individual neurons.

At the next level of description, the approach of inferring circuits from single cell anatomy (i.e. from reconstructions of complete axons and dendrites of neurons obtained after intracellular recordings in vitro or in vivo, e.g. (Brecht et al., 2003; Brecht and Sakmann, 2002a, b; Feldmeyer et al., 1999; Helmstaedter et al., 2008b; Lubke et al., 2003; Oberlaender et al., 2011)) was applied to the study of interlaminar connectivity (Binzegger et al., 2004; Lubke et al., 2003). The neocortex possesses six layers, which have a thickness of typically 100 - 500 µm in most mammals ((Peters and Jones, 1984b), see (Meyer et al.,

2010b) for data on rat cortex). The axonal trees of individual neurons are often restricted to particular layers or modules in the cortex (e.g., (Helmstaedter et al., 2008b; Lubke et al., 2000; Lubke et al., 2003)), such that the single cell anatomical data could be used for circuit predictions.

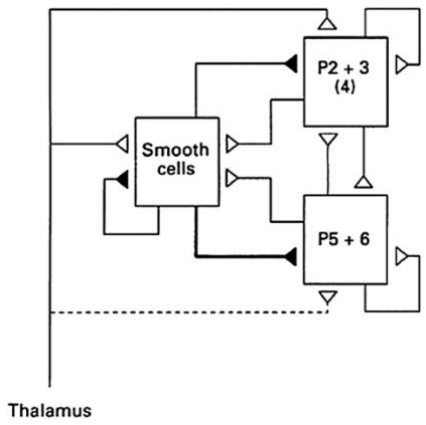

Figure 1.1: Canonical circuit for neocortex based on electrophysiological and modeling work in the cat visual system.
Interaction of three populations of neurons: inhibitory cells (smooth cells), excitatory pyramidal cells in upper layers (P2+3, including layer 4 spiny stellate cells (4)), and deep layer pyramidal neurons (P5+6). Thalamic input mainly targets superficial layers. Recurrent excitation and inhibition is prominent in all layers within cells of the same type and other cell types. From (Douglas and Martin, 1991), reprinted with permission.

Especially work in the cat visual system by Douglas and Martin had the ambition to determine stereotypic rules of wiring (Fig. 1.1). This work described a "canonical" microcircuit for neocortex based on translaminar axonal projections, and implied that the obtained connectivity is general across neocortical areas and mammalian species (Douglas and Martin, 1991, 2004; Douglas et al., 1989). Studies were carried out in various species and sensory cortices ranging from rodents via cats to tree shrews to primates (summarized in (Douglas and Martin, 2004), see for example (Feldmeyer et al., 1999; Ghosh et al., 1987; Gilbert and Wiesel, 1983; Lund et al., 1979; Usrey and Fitzpatrick, 1996)). The fact that the authors found this basic pattern of projections in different cortical areas and in all of these species enforced the notion of generality ("canonical nature") of the circuit.

Still, these circuit diagrams do not reveal direct communication between neurons, but rather reflect an approximation of the main interlaminar pathways. Even the most quantitative approaches of assigning a source to every synapse in these circuits (Binzegger et al., 2004; Lubke et al., 2003; Meyer et al., 2010a), are based on approximations such as Peters' rule (axons connect in direct proportion to the occurrence of all synaptic targets in the neuropil, (Braitenberg and Schüz, 1998)) and the equalization of axonal boutons (detectable as varicosities using light microscopic methods) with synapses (Fig. 1.2).

The precise mapping of point to point connections between neurons at synapses (today called "Connectomics") is achieved in smaller volumes of brain tissue by electron microscopy (EM). This ultrastructural approach is used to study local circuits, such as intralaminar connectivity, on a scale of a few 100 µm. In contrast to fluorescence-based labeling techniques that rely on the sparse labeling of neurons, EM stains result in a relatively unbiased labeling of all membranes and synapses of densely packed neurites (Peters and Palay, 1991). However, only few circuits have so far been mapped comprehensively: The complete reconstruction of the neuronal connectivity in C. elegans (initiated in the 1970s, (White et al., 1986)), was the first and largest such reconstruction for decades. Contemporary initiatives to map local circuits using EM in vertebrate and invertebrate systems, comprise the direction-selective wiring of the mouse retina (Briggman et al., 2011), analysis of the neuropil in rat hippocampus (Mishchenko et al., 2010), mouse primary visual cortex anatomy (Bock et al., 2011), the circuitry in the larval brain of Drosophila (Cardona et al., 2010; Eichler et al., 2017), area HVC of the zebra finch (Kornfeld et al., 2017) and the olfactory bulb of zebrafish (Wanner et al., 2016a), as well as the whole-brain EM in larval zebrafish (Hildebrand et al., 2017).

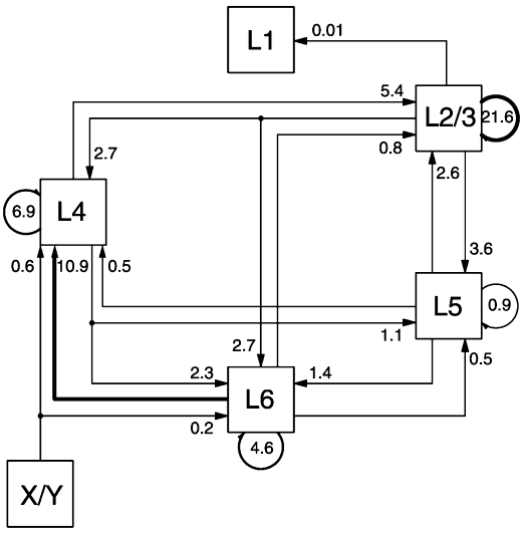

Figure 1.2: Quantitative analysis of excitatory connections between layers in cat visual cortex. Numbers indicate percentages of total excitatory synapses. Thalamic afferents (X/Y) mainly arrive in layer 4 (L4), leading to a signal propagation through layers 2/3 (L2/3), deep layers (L5, L6), and closing the major feed-forward loop with recurrent input back to L4. Note that only ~21% of excitatory synapses are involved in this pathway. Note further that the number of synapses formed in the self-innervation of individual layers is about the same (34%), pointing to self-innervation as an important feature of this circuit. From (Binzegger et al., 2004) with permission.

1.2 Connectomics

Sporns et al. define "For any given nervous system, the complete map of its neural components and their synaptic interconnections corresponds to the connectome" (Sporns, 2013; Sporns et al., 2005). The mapping and interpretation of connectomes, a field today called "connectomics", faces a range of methodological challenges that are described in the following sections.

1.2.1 Volume EM techniques

Modern volume EM methods are either based on wide field transmission electron microscopy (TEM) or scanning electron microscopy (SEM). In serial section TEM (ssTEM, Fig.1.3a, (Harris et al., 2006; White et al., 1986)) individual brain slices are cut with a diamond knife, collected manually onto an electron-transparent support film, and are typically post-stained to enhance contrast. This process generally suffers from variability in section thickness as well as missed and wrinkled slices. The electron beam, accelerated by a high voltage (80 – 120 kV), passes through the specimen onto a phosphor screen where a digital camera is used to capture the image.

In SEM, on the other hand, the specimen is raster scanned by a precisely focused electron beam. The signal is produced by backscattered electrons that are collected by a detector positioned above the sample. Usually low electron energies (1 – 3 kV) are used to limit the penetration depth of the electrons to only the very surface of the sample (Hennig and Denk, 2007). Consecutive images of the sample can be generated either by scanning previously cut ultrathin serial sections, or by the fully-automated, repeating process of imaging a block of tissue and the subsequent removal of its surface. An automated tape-collecting ultramicrotome (ATUM, (Hayworth et al., 2006; Kasthuri et al., 2015)), was developed to automatically pickup serial sections onto a support tape. However, with the use of electron opaque tape, the application of ATUM is mostly restricted to SEM (Fig. 1.3b, (Kasthuri and Lichtman, 2007)). In block-face SEM, the upper layer of tissue is either removed mechanically using a diamond knife (serial block-face SEM, Fig.1.3c, SBEM, (Denk and Horstmann, 2004)) or by milling with a focused ion beam (FIB-SEM, Fig. 1.3d, (Heymann et al., 2006; Knott et al., 2008)). This approach is destructive, since the sections are lost as soon as they are removed (see (Briggman and Bock, 2012)).

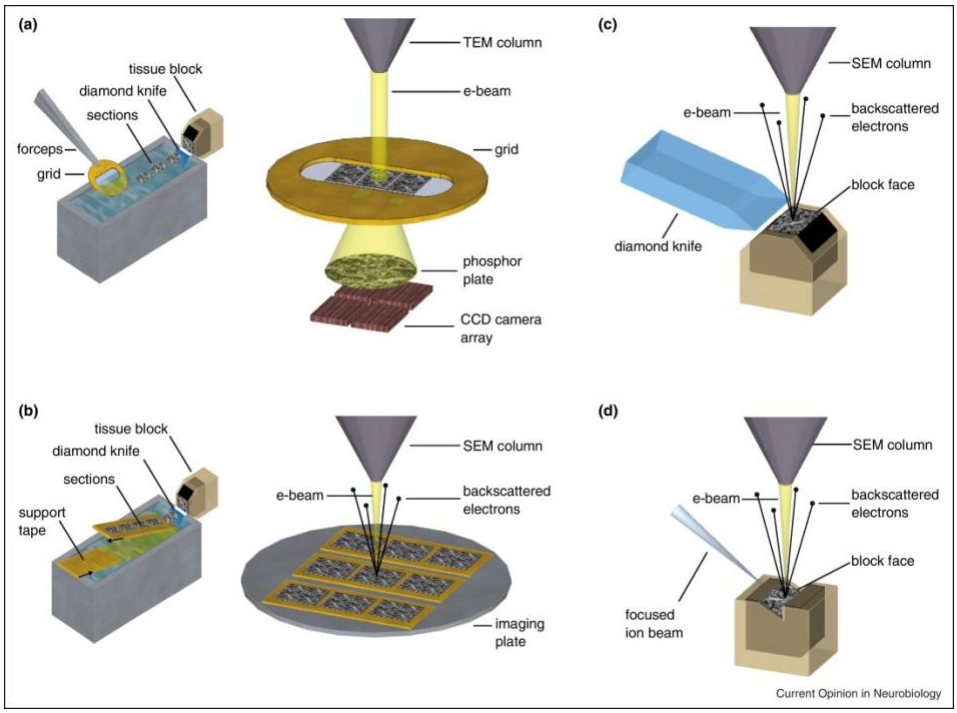

Figure 1.3: Overview of acquisition techniques for volume electron microscopy.
(a) Serial section transmission electron microscopy (ssTEM). **(b)** Automated tape-collecting ultramicrotome scanning electron microscopy (ATUM-SEM). **(c)** Serial block-face scanning electron microscopy (SBEM). **(d)** Focused ion beam milling scanning electron microscopy (FIB-SEM). Adapted from (Briggman and Bock, 2012) with permission.

1.2.2 Imaging resolution

For circuit reconstruction, the minimally required imaging resolution corresponds to roughly half the smallest neurite diameter found in the chosen tissue volume. The thinnest neurites are dendritic spine necks (e.g. 40-50 nm in rat hippocampus, (Harris and Stevens, 1989)). Therefore, the minimal resolution required for most circuits (in mouse and rat) is ~20-25 nm but can be as small as 10-15 nm in certain model system, like the fly (see (Helmstaedter, 2013) for an extended discussion).

The in-plane resolution provided by TEMs is usually 4-8 nm, because electrons of high energy are used. Currently, an x-y-resolution of about 12 nm is used in SBEM and up to 4 nm in FIB-SEM (Helmstaedter and Mitra, 2012). The different acquisition methods vary considerably with respect to their z – resolution. FIB-SEM obtains the highest z-resolution of 5 nm (Knott et al., 2008). SBEM and ATUM-SEM can achieve a cutting thickness of

20 – 30 nm (Briggman and Bock, 2012; Briggman et al., 2011). Manual ssTEM sections are typically limited to 40 – 50 nm (Harris et al., 2006). Thus, data annotation in ssTEM datasets is mostly restricted to in-plane analysis, since the resolution is highly anisotropic (very high x-y-resolution, but up to a factor of 10 less resolution across planes, (Helmstaedter and Mitra, 2012)).

1.2.3 Maximal circuit size

The various EM imaging methods described above are used to study neuronal circuits of various size. Using ssTEM and ATUM-SEM, the extent of the field of view in the plane of imaging can be several millimeters. Therefore, these methods are, in principle, applicable to answer connectivity questions between nearby brain regions or even in whole brains of fruit flies or zebrafish larvae. However, the generation of successive ultra-thin tissue slices (which limits the volume extent in the third dimension) is currently the main caveat.

Even though there are no fundamental technical limitations to image larger volumes, SBEM is currently optimized to tissue blocks of several 100 µm on a side (Denk and Horstmann, 2004). This method is best suited to study moderately sized circuits, for example connectivity within a cortical layer.

Image volumes acquired by FIB-SEM provide the highest 3-dimensional resolution, but are so far limited to about 50 – 100 µm extent. This approach is currently best suited for smaller species (e.g. fruit fly) and questions of very local synaptic circuitry (Briggman and Bock, 2012).

1.2.4 Challenges of high-throughput EM

The processing of nervous tissue for the dense reconstruction of the underlying circuits in volume EM represents a number of considerable challenges. Reliable staining protocols are required to label the densely packed neuropil in brain samples without membrane breakages or artifacts. Especially in SBEM, where post-staining of sections is not possible, penetration of the chemicals into the whole tissue block (en-bloc staining) needs to be guaranteed (Hua et al., 2015).

The completeness of EM-imaged volumes is crucial for the reconstruction of neurites. Consecutive missing sections (due to cutting artifacts, focus instabilities or other failures during the imaging process) increase the probability of ambiguities in the acquired data,

with fine processes like axons, spine necks or small dendrites being lost or confused during data annotation.

After data acquisition, the alignment and stitching of the image series into a 3-dimensional image volume is necessary. The post-processing of ssTEM and ATUM-SEM datasets typically requires complex warping algorithms and non-affine registration to compensate for the folding and stretching of tissue sections. On the contrary, images acquired with SBEM or FIB-SEM are taken from the surface of a tissue block and are therefore already comparably well aligned.

With advances in acquisition stability and speed, larger image volumes can be acquired (currently the datasets are about a dozen terabytes in size, and several petabytes seem possible in the near future) and larger circuits can be reconstructed. In fact, the main challenge in high-throughput 3D EM of neuronal tissue is the analysis of the imaging data. Human annotators provide highly accurate reconstructions of even the smallest neurites, but they are very slow and prone to make attentional mistakes. The development of efficient automated reconstruction methods is therefore essential for large-scale circuit analysis (Helmstaedter, 2013).

The reconstruction of neuronal circuits requires the detection of synapses and the identification of the pre- and postsynaptic neurons. In comparison to the identification of synapses from single 2-dimensional images acquired at high in-plane resolution (typically using TEM, e.g. (Harris et al., 2006; Harris and Stevens, 1988, 1989)), synapse detection in volume EM relies on sequences of typically dozens of images, allowing the identification of relevant synaptic features such as presynaptic vesicles, postsynaptic densities, and the locations of the postsynaptic partners. Automated synapse detection algorithms are available for high-resolution imaging using FIB-SEM (Kreshuk et al., 2011) and are recently also becoming available for SBEM datasets (SynEM, (Staffler et al., 2017); syConn, (Dorkenwald et al., 2017)).

The reconstruction of neuronal processes, however, is still a major challenge. The properties of brain tissue pose substantial problems: tiny neurites, high packing density of the neuropil, and the variety of diameter and local entanglement of neuronal processes. Based on this and the size of neurons, enormous reconstruction times ensue: the reconstruction of a neuron at

the LM level takes dozen of hours; the same procedure would take a factor of 100 longer in EM data (Helmstaedter et al., 2008a). Additionally, neurite continuity needs to be extremely reliable, as assigning synapses to wrong neurons leads to intolerable error rates in the connectivity matrix (Helmstaedter, 2013).

The key approach so far to resolve the reconstruction problem combines human expertise (manual skeletonization, (Helmstaedter et al., 2011)) with automated volume segmentation (for cortex data: SegEM, (Berning et al., 2015)). Human annotation is usually parallelized (i.e. redundant tracing of the same neuronal processes) and a consensus is found to reduce attention related errors (Helmstaedter et al., 2011). Efficient online annotation tools (webKnossos, (Boergens et al., 2017)) enable reconstruction velocities of 1.5 mm/h for axons and 2.1 mm/h for dendrites. In parallel, automated volume segmentation routines are trained and applied to the image data. The resulting piecewise volume segmentation is then combined with the skeleton annotations to result in a full-volume reconstruction of neurons (Berning et al., 2015; Helmstaedter et al., 2013).

1.3 Medial entorhinal cortex

The entorhinal cortex is positioned at the posterior side of the rodent cerebral cortex. It is partly enclosed by the rhinal fissure and surrounded by a number of cortical areas: olfactory and amygdaloid cortices (towards the anterior and lateral borders); parahippocampal formation (to the posterior and medial borders) (Fig. 1.4). Cytoachitectonic and connectional data support a subdivision of the entorhinal cortex into two functionally different regions – the lateral and medial entorhinal cortex (broadly corresponding to Brodmann areas 28a and 28b, (Brodmann, 1909)). Whereas cells in the lateral entorhinal cortex (LEC) are considered to convey olfactory information (Chapuis et al., 2013; Staubli et al., 1984a; Staubli et al., 1984b) and take part in object recognition (Deshmukh and Knierim, 2011) the medial entorhinal cortex (MEC) contains spatially modulated cells (Hafting et al., 2005; Sargolini et al., 2006; Solstad et al., 2008).

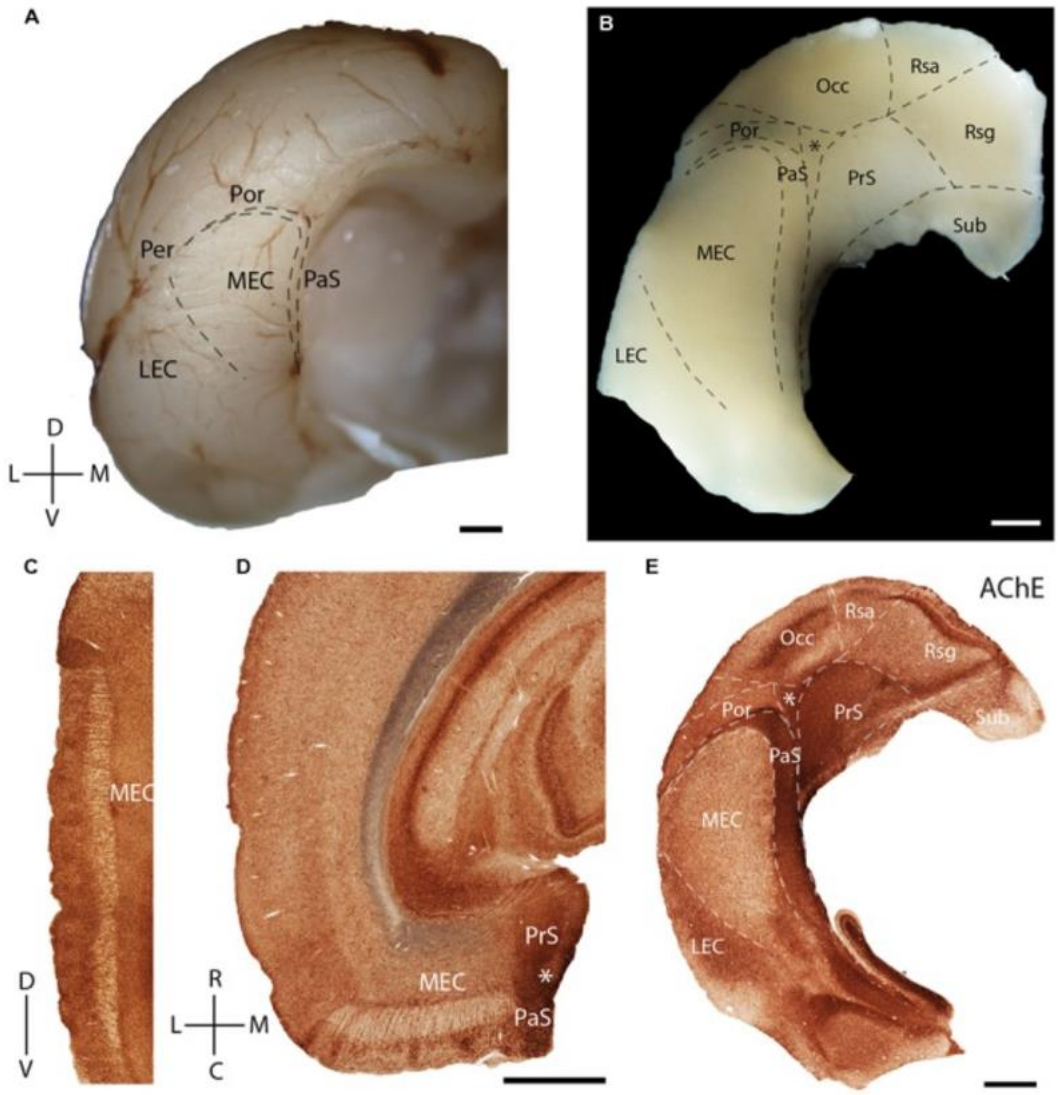

Figure 1.4: Overview of the parahippocampal region in rat. Location of the medial entorhinal cortex and the adjacent cortices.
(A) Posterior view of the left hemisphere. **(B)** Tangential section of the entorhinal cortex. Saggital **(C)**, horizontal **(D)**, and tangential **(E)** section processed for acetylcholinesterase activity.
Scale bars 1mm. MEC – medial entorhinal cortex; LEC – lateral entorhinal cortex; PaS – parasubiculum; Per – perirhinal cortex; Por – postrhinal cortex; Sub – subiculum; Rsg/Rsa – retrosplenial cortex; Occ – occipital cortex; (*) – triangular region; D – dorsal; V – ventral; L – lateral; M – medial; R – rostral; C – caudal. From (Ray et al., 2017).

1.3.1 Layers and cell types

The lamination of the MEC is a transition between the three-layered allocortex and the six-layered neocortex. The outermost layer (L1) is almost free of somata (the remaining somata are GABAergic interneurons), containing a dense band of transversely oriented fibers. Layer 2 consists mainly of densely packed pyramidal and stellate cells (Alonso and Klink,

1993; Germroth et al., 1989). Interneurons within L2 are described as multi- and bipolar neurons, fast spiking basket cells, and chandelier cells. Layer 3 is a broader layer containing loosely arranged pyramidal neurons. The deeper border of L3 is delineated by the lamina dissecans, a fiber-dense layer lacking cell bodies (corresponding to a remnant of layer 4). Layer 5 of the MEC is stratified and can be subdivided into an upper layer of large pyramidal neurons, having a tuft that traverses superficial layers and may reach the pial surface, and a deeper layer of smaller horizontal pyramidal cells with dendritic trees confined to L5 and L6. The deepest layer (L6) contains largely multipolar neurons, whose dendritic trees mainly stay within this layer (Canto et al., 2008).

1.3.2 Extrinsic connectivity

The MEC is often perceived as a major input and output structure of the hippocampal formation, serving a pivotal role in cortico-hippocampal interactions. The superficial layers project to the dentate gyrus and the hippocampus. More precisely, L2 mainly targets the dentate gyrus and hippocampal CA3 / CA2 region (Witter, 2007) whereas L3 predominantly projects to CA1 and subiculum (Steward and Scoville, 1976). The main input to L2 and L3 of the MEC arises from the presubiculum, parahippocampal-postrhinal, and retrosplenial cortices, as well as the prefrontal cortex (Insausti and Amaral, 2008; Kerr et al., 2007). The deep layers of the MEC receive projections from CA1 and subiculum, closing the entorhinal – hippocampal loop (Swanson and Cowan, 1977; Tamamaki and Nojyo, 1995). Entorhinal – cortical connectivity largely arises in these layers, mostly reciprocating the cortical afferents (Canto et al., 2008).

1.3.3 Spatially modulated cells

The MEC comprises a few functionally dedicated cell types that represent position and orientation in the environment: grid cells (Hafting et al., 2005), border cells (Solstad et al., 2008), and head direction cells (Sargolini et al., 2006).

Grid cells encode an animal's location in the environment. They have multiple firing fields that are arranged in a hexagonal manner across the entire environment. The size and frequency of the firing fields as well as their locations (spatial phase) differ between cells, yielding a complete coverage of the environment with only a few cells (Hafting et al., 2005). Notably, the firing pattern of grid cells remains stable irrespective of the speed and head direction of an animal. Border cells on the other hand indicate the animal's distance to

geometric borders. They mostly fire only on one of the borders of a given environment and maintain their activity when the environment size is manipulated (Solstad et al., 2008). Finally, head direction cells reflect the orientation of an animal relative to fixed landmarks in the environment.

1.3.4 Microcircuitry

Layer 2 of the MEC contains the largest fraction of pure grid cells compared to other layers of the MEC (Boccara et al., 2010). Two main principal neuronal types, stellate and pyramidal cells, have been described in L2 (Alonso and Klink, 1993; Germroth et al., 1989), with remarkably distinct electrophysiological features (Alonso and Llinas, 1989; Klink and Alonso, 1997), immunoreactivity (Varga et al., 2010), and projection pattern (Lingenhohl and Finch, 1991).

Accumulating evidence from in vitro studies indicates that stellate and pyramidal neurons engage in cell-type specific microcircuits. Using paired intracellular recordings, no recurrent excitatory connections were found among L2 stellate cells (Couey et al., 2013; Dhillon and Jones, 2000; Pastoll et al., 2013). Instead, Couey et al. report disynaptic inhibition of stellate cells via fast-spiking interneurons. However, monosynaptic excitation among principal L2 neurons was observed (Beed et al., 2010), which potentially arise from predominantly directional connectivity of pyramidal to stellate cells (Winterer et al., 2017). Pyramidal cells were found to receive selective inhibition by cholecystokinin (CCK) - positive interneurons (Varga et al., 2010), as well as a substantially larger fraction of excitatory inputs from deep layers in comparison to stellate cells (Beed et al., 2010), indicating that pyramidal cells can integrate a broader range of inputs from deep layers. Other functional studies provided evidence for a columnar organization of interlaminar connections (Kloosterman et al., 2003; Stensola et al., 2012; Stewart, 1999). It is not known, however, whether signal transformation across layers in MEC is similar to the canonical circuitry described in the visual cortex (Burgalossi and Brecht, 2014).

1.4 Scope of this thesis

This thesis explores the anatomical organization of layer 2 in the medial entorhinal cortex. This is pursued at the level of cellular organization (chapter 2), where the light-microscopically determined arrangement of cell clusters is investigated[1], followed by a detailed connectomic analysis of individual axons and the circuits they form using state-of-the-art 3-dimensional electron microscopy techniques[2] (chapter 3).

[1]This work was first reported in the following journal papers:

(1) Ray, S.*, Naumann, R.*, Burgalossi, A.*, Tang, Q.*, Schmidt, H.*, Brecht, M. „Grid-layout and theta-modulation of layer 2 pyramidal neurons in medial entorhinal cortex“, Science, 2014 (*: equally contributing first authors). This study was performed in a collaborative approach. The author of this thesis contributed to the visualization of pyramidal cell clusters (calbindin stainings), performed retrograde neuronal labelling experiments, and analysed the alignment of the calbindin grid to the parasubiculum, the probability of hexagonal arrangement, as well as the proximity of cholinergic boutons to calbindin-positive dendrites.

(2) Tang, Q., Burgalossi, A., Ebbesen, CL., Ray, S., Naumann R., Schmidt, H, Spicher, D., Brecht, M. “Pyramidal and stellate cell specificity of grid and border representations in layer 2 of medial entorhinal cortex”, Neuron, 2014. The author of this thesis contributed the spine density measurements.

(3) Tang, Q., Burgalossi, A., Ebbesen, C.L., Sanguinetti-Scheck, J.I., Schmidt, H., Tukker, J.J., Naumann, R., Ray, S., Preston-Ferrer, P., Schmitz, D., Brecht, M. “Functional Architecture of the Rat Parasubiculum“, Journal of Neuroscience, 2016. The author of this thesis contributed to the anterograde tracing experiments.

[2]This work was first reported as a journal paper: Schmidt, H., Gour, A., Straehle, J., Boergens, K.M., Brecht, M., Helmstaedter, M. „Axonal synapse sorting in medial entorhinal cortex“, Nature, 2017. The author of this thesis performed all experiments and analyses in this work, with contributions from A.G. to the P90 experiment, and with the exception of the numerical simulations, and co-wrote the paper.

2 Grid-layout of Layer 2 Pyramidal Neurons in Medial Entorhinal Cortex

The work presented in this chapter was first published in:

Ray, S.*, Naumann, R.*, Burgalossi, A.*, Tang, Q.*, Schmidt, H.*, Brecht, M. (2014). Grid-layout and theta-modulation of layer 2 pyramidal neurons in medial entorhinal cortex. Science 343:891-6.

Tang, Q.*, Burgalossi, A.*, Ebbesen, C.L.*, Ray, S., Naumann, R., Schmidt, H., Spicher, D., Brecht, M. (2014). Pyramidal and stellate cell specificity of grid and border representations in layer 2 of medial entorhinal cortex. Neuron 84:1191-1197.

Tang, Q., Burgalossi, A., Ebbesen, C.L., Sanguinetti-Scheck, J.I., Schmidt, H., Tukker, J.J., Naumann, R., Ray, S., Preston-Ferrer, P., Schmidtz, D., Brecht, M. (2016). Functional architecture of the rat parasubiculum. Journal of Neuroscience 36 (7) 2289-2301.

* These authors contributed equally.

This is the authors' version of the work.

2.1 Introduction

Little is known about how microcircuits are organized in layer 2 of the medial entorhinal cortex (MEC). Temporal (Boccara et al., 2010; Mizuseki et al., 2009; Quilichini et al., 2010) and spatial (Hafting et al., 2005) discharge patterns in layer 2 of the MEC are related through phase precession (Hafting et al., 2008) and the correlation of gridness (hexagonal regularity) and theta-rhythmicity (Boccara et al., 2010). Layer 2 principal neurons divide into pyramidal and stellate cells, the latter of which have been suggested to shape entorhinal theta (Alonso and Klink, 1993; Alonso and Llinas, 1989) and grid activity (Hasselmo et al., 2007) by their intrinsic properties. Clustering of grid cells (Stensola et al., 2012) points to spatial organization. It is not clear, how functionally defined cell types correspond to stellate and pyramidal cells (Alonso and Klink, 1993; Germroth et al., 1989), which differ in conductances, immunoreactivity, projections, and inhibitory inputs (Alonso and Llinas, 1989; Canto and Witter, 2012; Klink and Alonso, 1997; Lingenhohl and Finch, 1991; Varga et al., 2010). Here, we aimed for a comprehensive description of the anatomical organization of MEC layer 2 (analysis of modular arrangement, the dichotomy of the two principle cell types, and cholinergic and parasubicular inputs) by combining immunohistochemical stainings with tracing experiments and juxtacellular labeling.

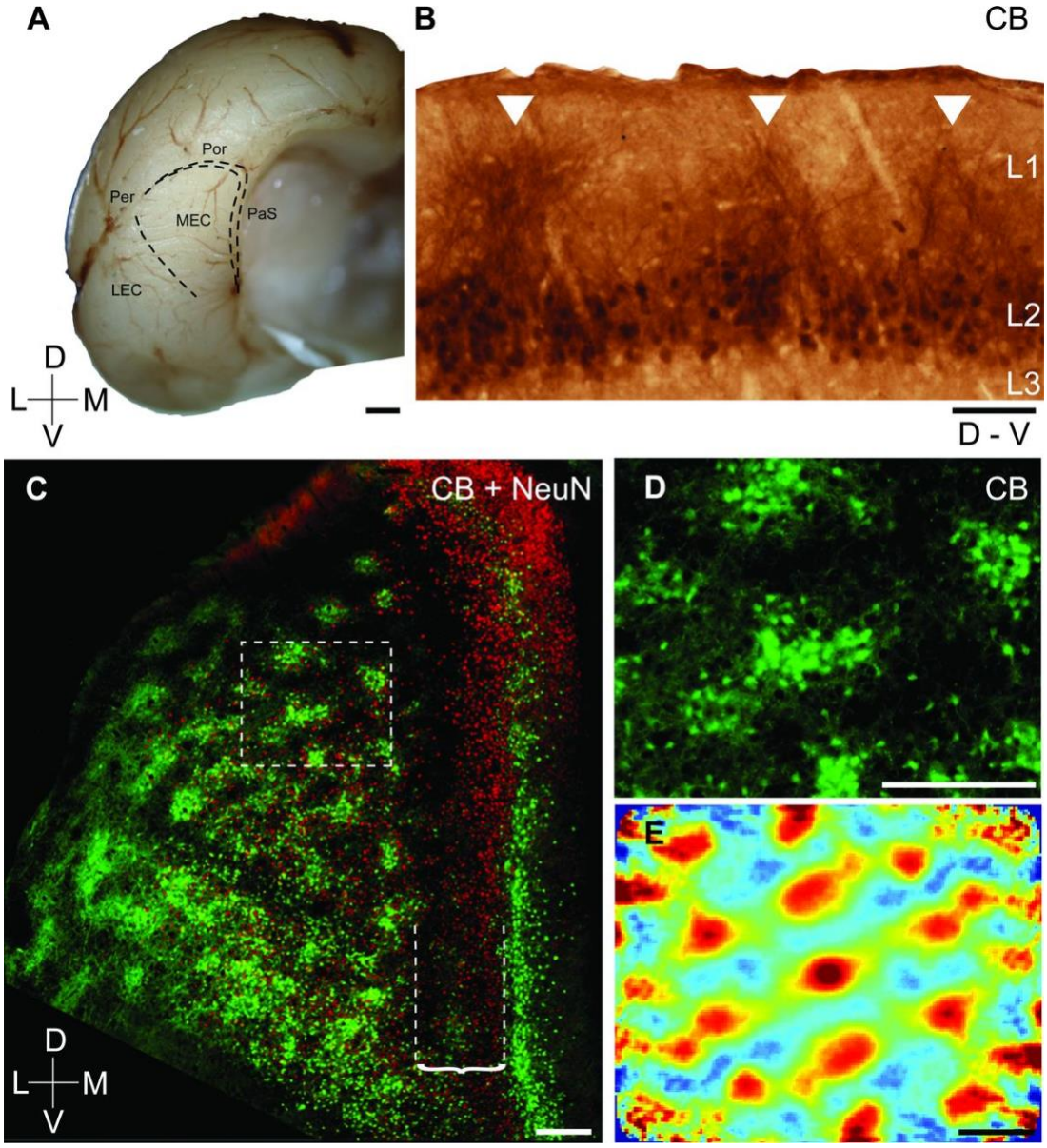

Figure 2.1: Grid-like arrangement of calbindin$^+$ pyramidal cells in the MEC.
(A) Posterior view of a rat cortical hemisphere. LEC, lateral entorhinal cortex; PaS, parasubiculum; Per, perirhinal cortex; Por, postrhinal cortex. **(B)** Calbindin$^-$immunoreactivity (brown precipitate) in a parasaggital section reveals patches with apical dendrites of calbindin$^+$ pyramidal cells forming tents (white arrows) in layer 1. **(C)** Tangential section showing all neurons (red, NeuN-antibody) and patches of calbindin$^+$ neurons (green). Bracket, dashed lines indicate the patch-free stripe of MEC. **(D)** Inset from (C). **(E)** Two-dimensional spatial autocorrelation of (D) revealing a hexagonal spatial organization of calbindin$^+$ patches. Color scale, –0.5 (blue) through 0 (green) to 0.5 (red); grid score is 1.18. Scale bars, (A) 1 mm; (B) 100 µm; (C) to (E) 250 µm. D, dorsal; L, lateral; M, medial; V, ventral. From (Ray et al., 2014).

2.2 Results

Calbindin immunoreactivity (Varga et al., 2010) identifies a relatively homogeneous pyramidal neuron population in MEC layer 2. Parasagittal sections stained for calbindin (Fig. 2.1B) showed that calbindin positive (calbindin$^+$) pyramidal cells were arranged in patches (Fujimaru and Kosaka, 1996). Apical dendrites of calbindin$^+$ pyramidal cells bundled together in layer 1 to form tent-like structures over the patches (Fig. 2.1B). The patchy structure is well defined at the layer 1/2 border, whereas a "salt-and-pepper" appearance of calbindin$^+$ and calbindin$^-$ cells is observed deeper in layer 2 (Fig. 2.2).

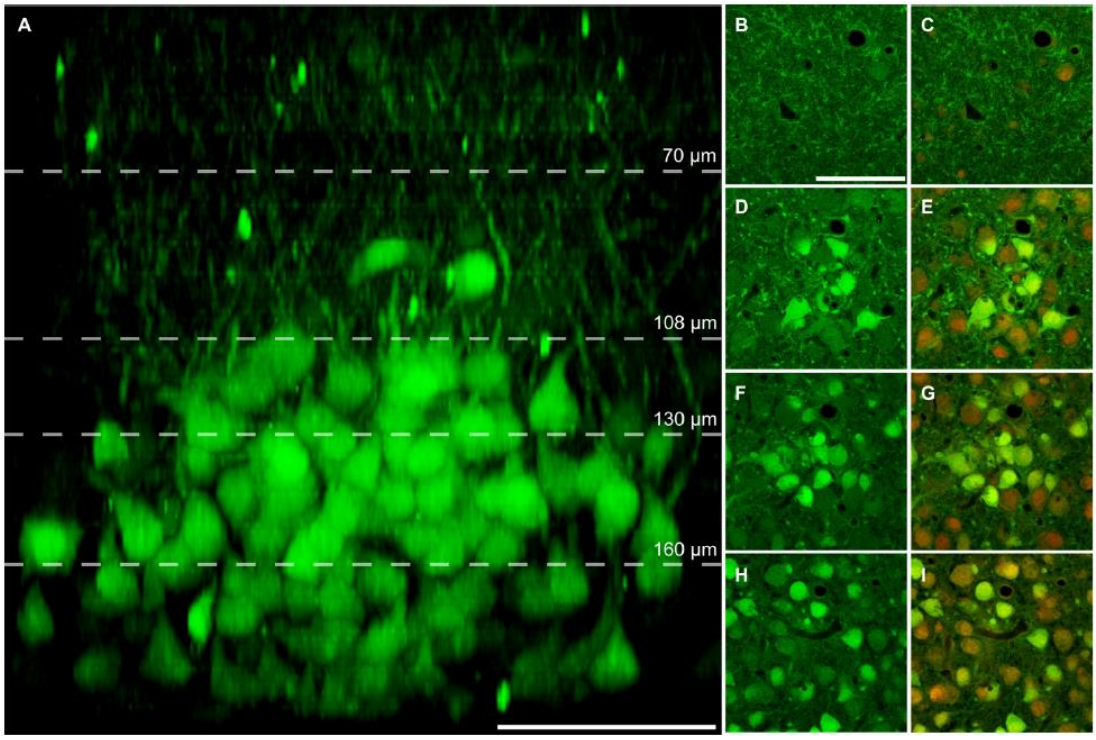

Figure 2.2: Cellular architecture of an individual calbindin patch.
(A) Side view of an optically-cleared patch of calbindin$^+$ cells. Serial optical sections spaced 2 µm apart were taken along the x-z-axis and displayed as maximum intensity projection. **(B-I)** Optical sections at the levels indicated in A, showing calbindin$^+$ cells in green (B, D, F, H) and an overlay of calbindin$^+$ cells in green and red autofluorescence showing all neurons (C, E, G, I). Dashed lines in A indicate the level of the optical sections displayed in (B-I): 70 µm below surface (B, C), 108 µm below surface D, E, 130 µm below surface (F, G) and 160 µm below surface (H, I). Note the increase in patch diameter from the upper to middle levels. At the lower level there is no apparent modular structure of calbindin$^+$ cells. Scale bars: A = 50 µm; B = 50 µm, applies to B-I. From (Ray et al., 2014).

Patches contained 187 ± 70 cells (111 ± 42, ~60% calbindin$^+$; 76 ± 28, ~40% calbindin$^-$ cells; counts of 19 patches from four brains). We double-stained tangential sections for calbindin (green) and the neuronal marker NeuN (red) to visualize patches in the cortical plane. Calbindin$^+$ (green/yellow) patches covered the MEC except for a 400- to 500-µm-

wide patch-free medial stripe adjacent to the parasubiculum (Fig.2.1C). Clustering was not observed in calbindin$^-$ neurons (red) (Fig. 2.1C). We noted a striking hexagonal organization of calbindin$^+$ patches (Fig. 2.1, C and D) and characterized this organization by means of three techniques. (i) We used two-dimensional spatial autocorrelation analysis (4), which captures spatially recurring features and revealed a hexagonal regularity (Fig. 2.1E). (ii) We modified grid scores (Sargolini et al., 2006) to quantify hexagonality also in elliptically distorted hexagons (Barry et al., 2012a), distortions that result from tissue curvature and anisotropic shrinkage. Grid scores range from –2 to +2, with values >0 indicating hexagonality. The example in Fig. 2.1D had a grid score of 1.18, suggesting a high degree of hexagonality. (iii) We assessed the probability of hexagonal patch arrangements given preserved local structure (Krupic et al., 2012) by means of a shuffling procedure. We found that the strongest Fourier component of the sample (Fig. 2.1D) exceeded that of the 99th percentile of shuffled data, suggesting that such hexagonality is unlikely to arise by chance.

We retrogradely labeled neurons from ipsilateral dentate gyrus (Fig. 2.3A) using biotinylated dextran amine (BDA) (Fig. 2.3B) or cholera toxin B (Fig. 2.3C) to investigate the arrangement of layer 2 principal cells with identified projection patterns and immunoreactivity (Varga et al., 2010). Although most retrogradely labeled neurons were stellate cells (Germroth et al., 1989; Tamamaki and Nojyo, 1993), a small fraction had pyramidal morphologies, but these neurons appeared larger than calbindin$^+$ pyramidal cells (Fig. 2.3B). Calbindin$^+$ neurons did not project to the dentate gyrus (only 1 double-labeled out of 313 neurons in Fig. 2.3, C to E) (Varga et al., 2010). Calbindin$^+$ patches were hexagonally arranged (Fig. 2.3, C, D, and F), whereas dentate gyrus– projecting neurons (red) were uniformly distributed (Fig. 2.3, E and G). Reconstructions of calbindin$^+$ and calbindin$^-$ cells labeled in vivo confirmed their pyramidal and stellate morphologies, respectively. Calbindin$^+$ dendrites were largely confined to patches, whereas calbindin$^-$ stellates cells had three times larger dendritic trees (7.6 versus 2.6 mm average total length, $P < 0.03$), which extended unrelated to patches (Fig. 2.3, H and I). Interestingly, the spine density in calbindin$^+$ cells decreased as a function of distance from the soma, whereas the reverse was true for calbindin$^-$ cells (Fig. 2.4). Differentiating layer 2 neurons by calbindin and reelin immunoreactivity confirmed patchy hexagonality of calbindin$^+$ cells and scattered distribution, of reelin$^+$ cells without overlap between these neurons (Fig. 2.5) (Varga et al., 2010).

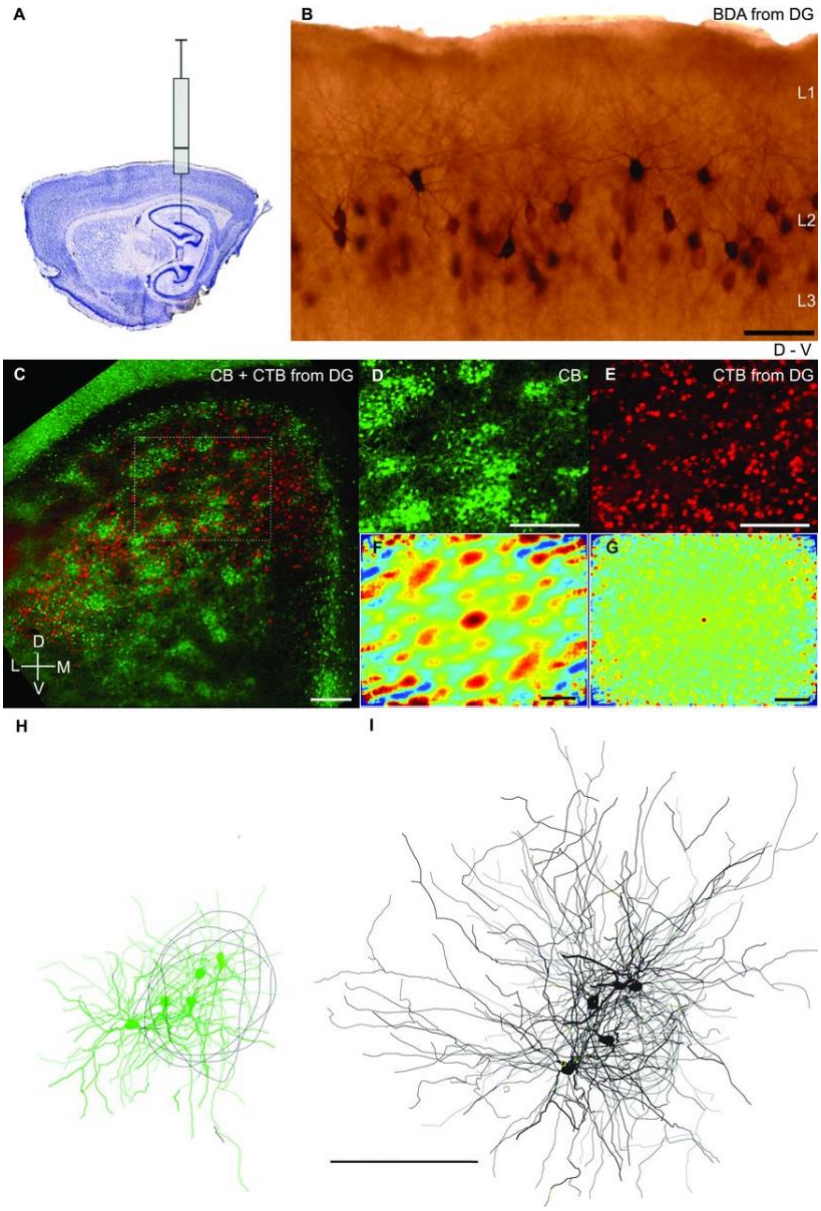

Figure 2.3: Calbindin$^+$ pyramidal but not dentate-projecting stellate neurons form patches.
(A) Schematic of retrograde labeling from dentate gyrus. **(B)** Such retrograde labeling (BDA, brown) stains neurons (most with stellate morphologies) in a parasaggital MEC section. **(C)** Tangential MEC section showing calbindin$^+$ neurons (green) and retrogradely labeled neurons (red) after dentate-gyrus–cholera–toxin-B injection. **(D and E)** Insets from (C). **(F)** Two-dimensional spatial autocorrelation of (D) reveals regular organization of calbindin$^+$ patches; grid score is 0.32. The strongest Fourier component of the sample exceeded that of the 99th percentile of shuffled data confirming hexagonality. **(G)** Two-dimensional spatial autocorrelation of **(E)** reveals no spatial organization; grid score is –0.03. **(H and I)** Superimposed reconstructions of dendritic morphologies of 5 calbindin$^+$ pyramidal (green) and 5 calbindin$^-$ stellate neurons (black) in the tangential plane. Morphologies were "patch-centered" aligned according to orientation and the center of the nearest calbindin$^+$ patch (gray outlines). Scale bars, (B) 100 μm; (C) to (E) and (G) to (I) 250 μm. D, dorsal; L, lateral; M, medial; V, ventral. From (Ray et al., 2014).

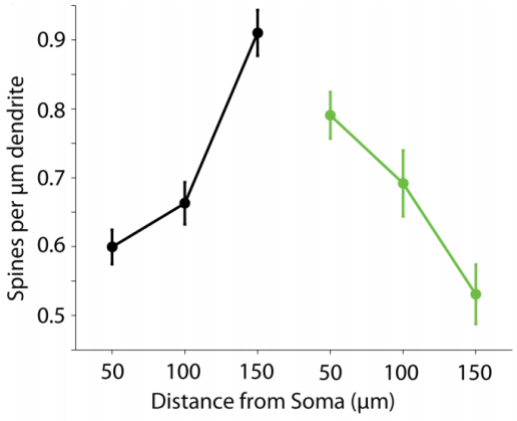

Figure 2.4: Spine distribution differs in calbindin$^+$ (green) and calbindin$^-$ cells (black).
Data refer to ten cells each, for which spine densities in multiple ~30 µm dendrite segments were counted at the distances from the soma specified in the plot. Slopes of spine density differed significantly between calbindin+ cells and calbindin- cells ($P < 0.003$, t-test). Error bars indicate SEM. From (Tang et al., 2014b).

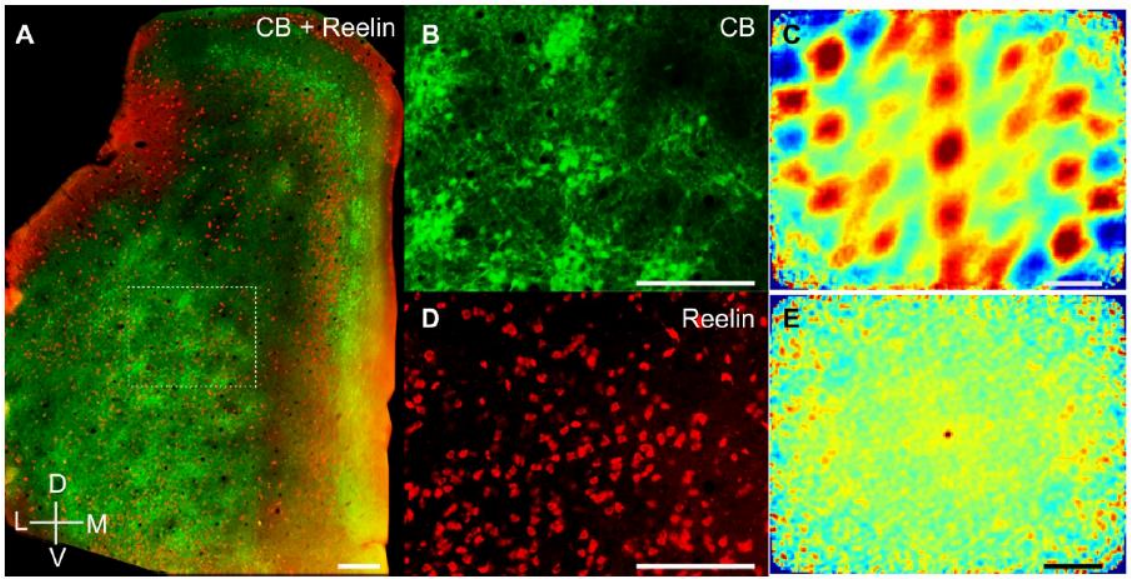

Figure 2.5: Calbindin-positive pyramidal neurons but not reelin-positive cells form patches.
(A) Tangential section of the rat MEC showing calbindin$^+$ pyramidal neurons and neuropil (green) and reelin$^+$, putative stellate, neurons (red). Calbindin$^+$ and reelin$^+$ neurons form two nonoverlapping populations (2 double-labeled neurons in 168 calbindin$^+$ and 405 reelin$^+$ layer 2 neurons) (20). **(B)** Inset from A showing a high magnification of calbindin$^+$ patches. **(C)** Two-dimensional spatial autocorrelation of B illustrating regular spatial organization of calbindin$^+$ patches. The grid score is 0.49. The strongest Fourier component of the sample exceeded that of the 99th percentile of shuffled data, confirming hexagonality. **(D)** Corresponding image section from B showing reelin$^+$ neurons. **(E)** Spatial autocorrelation of D illustrating a lack of spatial organization of reelin$^+$ neurons. The grid score is -0.04. Scale bars: A-E = 250 µm. D = dorsal, L = lateral, M = medial, V = ventral. From (Ray et al., 2014).

To investigate the organization of calbindin^{+} patches across the MEC, we prepared flattened whole-mount preparations. Patches had similar arrangements throughout the dorsoventral extent of the MEC (Fig. 2.6). At the layer 1/2 border, we consistently observed hexagonal arrangements in well-stained specimens. We quantified patch size and spacing in 10 largely complete MEC whole mounts. Patch density was similar throughout the MEC, whereas patch diameter slightly increased toward ventral (Fig. 2.6). We estimated 69 ± 17 patches across the entire MEC (n = 10 hemispheres). Calbindin patches stained also positive for cytochrome-oxidase activity (Burgalossi et al., 2011). However, the two staining patterns were not the same because calbindin patches were more sharply delineated than were spots revealed by cytochrome-oxidase activity, and cytochrome-oxidase staining revealed many more patches than did calbindin staining in the MEC (Burgalossi et al., 2011). Moreover, the staining patterns did not correspond at all in the parasubiculum.

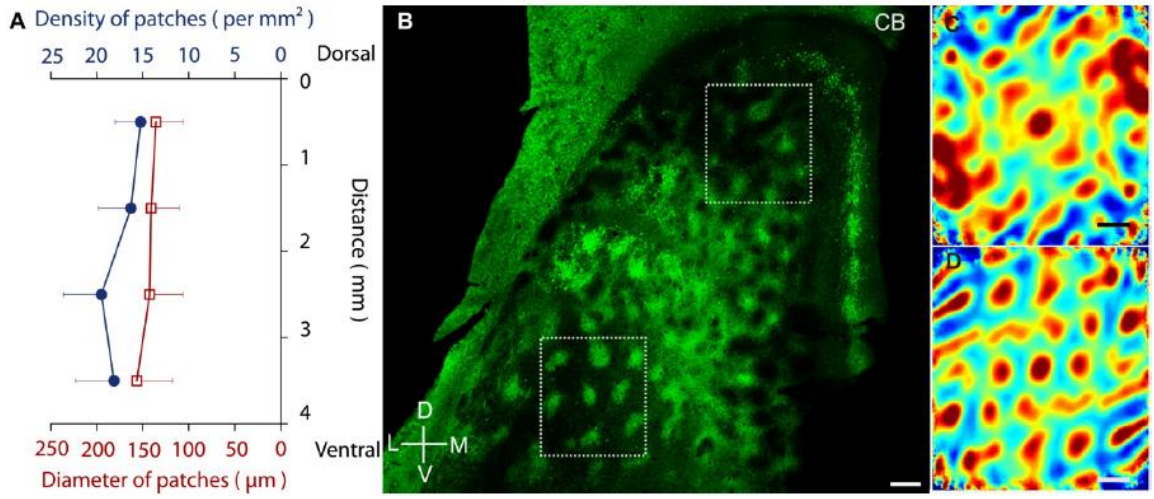

Figure 2.6: Layout of calbindin patches across the extent of medial entorhinal cortex. **(A)** Measurements of mean patch diameter (red) and density (blue) across the dorsoventral extent of the MEC. Measurements refer to ten MEC whole-mounts and did not include the medial patch-free stripe of MEC (see Fig 2.1C). Error bars = SD. **(B)** Tangential section from a flattened cortical preparation processed for calbindin immunoreactivity (green) showing modularity throughout the MEC. The image was flipped around the vertical axis for comparability. **(C)** Two-dimensional spatial autocorrelation of the dorsal inset in A. The grid score is 0.32. The strongest Fourier component of samples C, D exceeded that of the 99th percentile of shuffled data confirming hexagonality. **(D)** Two-dimensional spatial autocorrelation of the ventral inset in A. The grid score is 0.79. Scale bars: B-D = 250 µm. D = dorsal, L = lateral, M = medial, V = ventral. From (Ray et al., 2014).

Calbindin$^+$ patches shared a roughly 60° symmetry of their axes (Fig. 2.7A). One axis runs parallel to the dorsoventral axis of the parasubiculum (Fig. 2.7, A and B). Lines fitted through the dorsoventral axis of the parasubiculum, and the most medial column of calbindin$^+$ patches had the same orientation (Fig. 2.7B). A second consistent axis was tilted ~60° relative to the dorsoventral axis. This calbindin$^+$ patch axis curved ventrally at more lateral positions and aligned with the orientation of overlaying layer 1 myelinated axons (Fig. 2.7, C to F). Thus, the line connecting diagonally neighboring calbindin patches (revealed by spatial autocorrelation) (Fig. 2.7, D and E) aligned with the orientation of layer 1 axons (Fig. 2.7F). We quantified the orientation of axonal segments by a polar plot shown in Fig. 2.7G and confirmed that layer 1 axons share one main orientation in the MEC (Blackstad, 1956; Burgalossi et al., 2011; Witter et al., 1989).

MEC function and grid cell activity (Barry et al., 2012b; Heys et al., 2012) depend on medial septum inputs (Brandon et al., 2011; Koenig et al., 2011) and cholinergic transmission. We observed a patchy pattern of acetylcholinesterase labeling at the layer 1/2 border (Fig. 2.7H), which colocalized with the cores of calbindin$^+$ patches (Fig. 2.7, H to J). Axonal terminals positive for the vesicular acetylcholine transporter (VAChT) were closely apposed to calbindin$^+$ cells, and their density was twofold larger in calbindin$^+$ patches than between patches (Fig. 2.8). We also stained for m1 muscarinic receptors and observed a diffuse labeling without colocalization of these receptors to VAChT puncta. Moreover, we analyzed the apposition and distribution of presynaptic VAChT puncta relative to dendrites of in vivo filled calbindin$^+$ and calbindin$^-$ layer 2 cells by means of confocal microscopy. VAChT puncta were much more abundant around calbindin$^+$ than calbindin$^-$ layer 2 cells, but proximity histograms of VAChT puncta and dendrites did not indicate a direct targeting of calbindin$^+$ cell dendrites by cholinergic synapses (Fig. 2.8). Both the m1 receptor labeling and the dendrite-VAChT puncta colocalization analysis are in line with a volumetric action of acetylcholine in the MEC (Agnati et al., 2006; Hasselmo and McGaughy, 2004; Teles-Grilo Ruivo and Mellor, 2013).

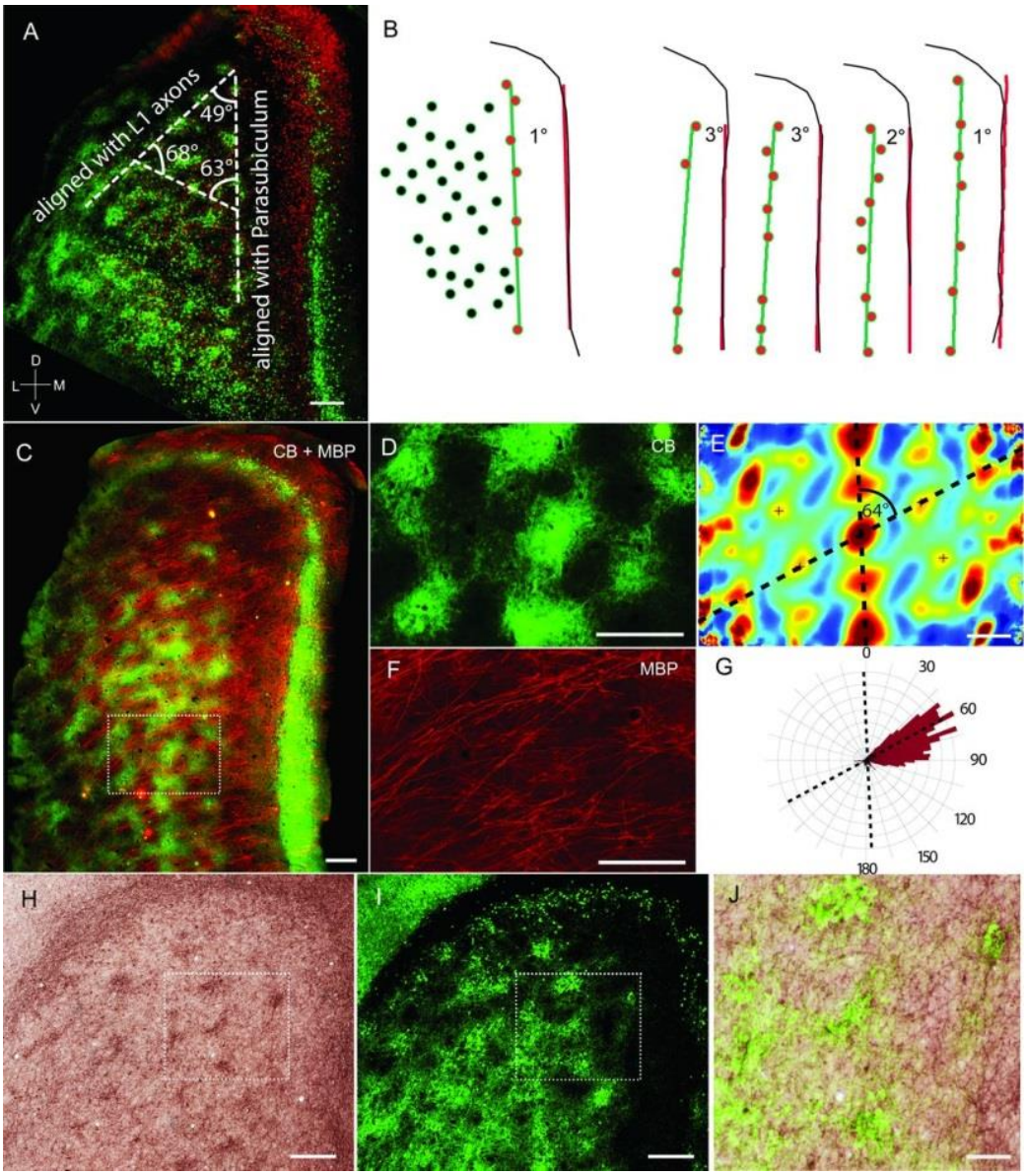

Figure 2.7: Alignment of the calbindin grid to parasubiculum, layer 1 axons, and cholinergic markers.
(A) Section from Fig. 1C. Dashed white lines indicate axes of the calbindin$^+$ grid (angles are indicated). Axes aligned with parasubiculum (B) and layer 1 axons [(C) to (G)]. **(B)** (Left) Schematic of calbindin patches and parasubiculum from (A). The orange line fits the dorsoventral axis of the parasubiculum, and the green line fits the most medial column of patches (red); the angle between these lines is indicated. (Right) Fitted lines and their relative angles for four other brains. **(C)** Tangential section processed for calbindin (green) and myelin basic protein (red). **(D)** Inset from (C). **(E)** Two-dimensional spatial autocorrelation of (D). Dashed black lines indicate grid axes. **(F)** Inset from (C). **(G)** Axonal segments in (F) were manually traced from left to right, and we computed a polar plot (red) of the orientations of the axonal segments. The orientations of axonal segments aligned with one axis of the grid of calbindin patches [superimposed dashed lines from (E)]. **(H)** Tangential section stained for acetylcholinesterase activity. **(I)** Section from (H) costained for calbindin. **(J)** Overlay of (H) and (I) shows overlap between acetylcholinesterase and calbindin staining. Scale bars, (A), (C) to (F), (H), and (I) 250 μm; (J) 100 μm. D, dorsal; L, lateral; M, medial; V, ventral. From (Ray et al., 2014).

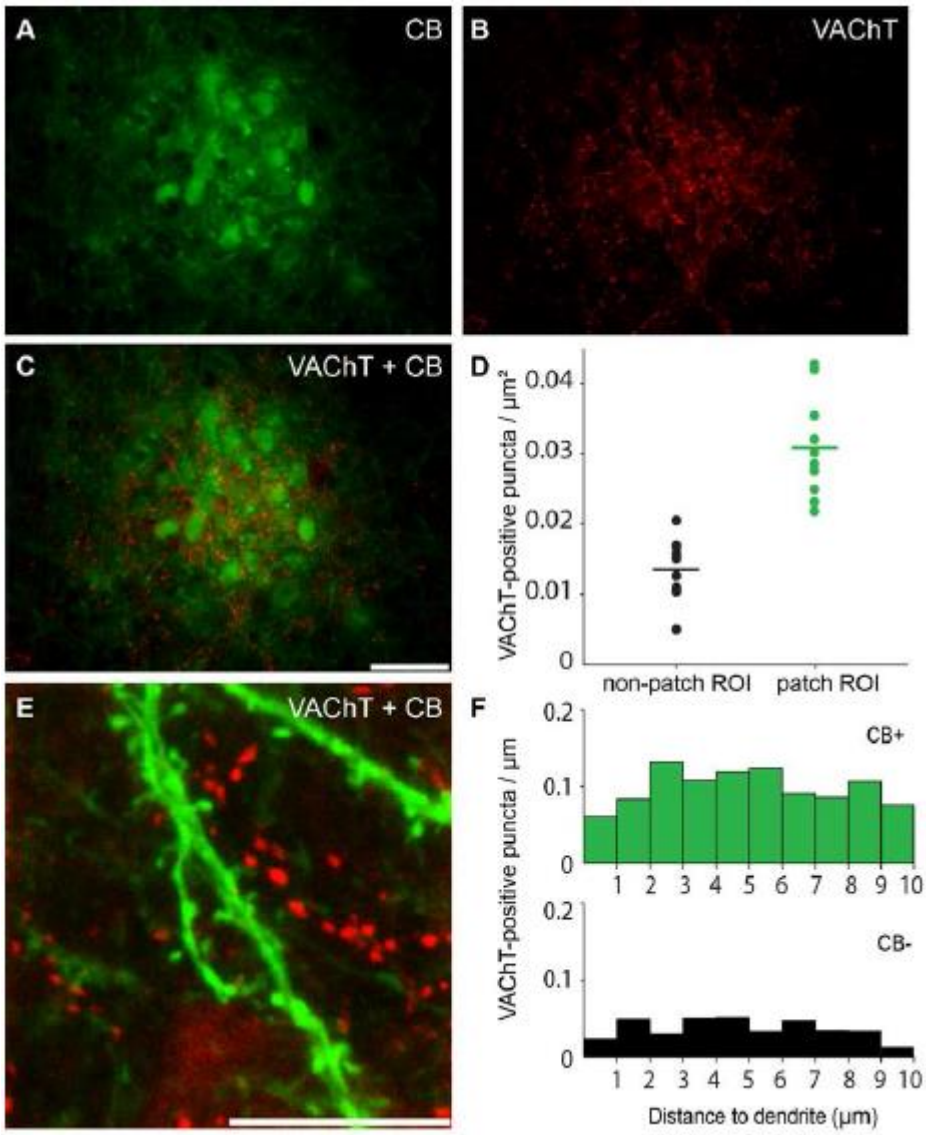

Figure 2.8: Vesicular acetylcholine transporter, calbindin patches and proximity of cholinergic boutons to calbindin-positive dendrites.
(A) Fluorescence micrograph showing one calbindin patch from a tangential section stained for calbindin (green). **(B)** Same section as in A stained for VAChT immunoreactivity (red). Note the higher density of VAChT-positive puncta in the calbindin-patch than in the surrounding area. **(C)** Overlay of A and B. **(D)** Density of VAChT-positive puncta in calbindin patches (green dots) and non-patch areas (black dots) at the layer 1/2 border. In five rats we selected 10 regions of interest (ROI) centered on calbindin patches and 10 ROIs positioned equidistant between calbindin patch centers. Horizontal bars indicate mean values. All VAChT positive puncta in the ROI were counted and divided by area size to obtain puncta density. **(E)** Fluorescence micrograph showing an overlay of a calbindin$^+$ dendrite (green) and nearby VAChT-positive puncta (red). **(F)** Histogram of the closest distance of VAChT-positive puncta to dendrites of calbindin$^+$ (top) and calbindin$^-$ (bottom) cells. We selected 35 dendritic segments of calbindin$^+$ and 25 segments of calbindin$^-$ dendrites and measured the distance of VAChT-positive puncta and dendrites. The histograms were normalized by dendritic length to obtain the number of VAChT-positive puncta per µm. Data refer to 10 (5 each) juxtacellularly stained calbindin$^+$ and calbindin$^-$ neurons. Scale bars: A, B, C = 50 µm; E = 10 µm. From (Ray et al., 2014).

Finally, we were interested in how parasubicular circuits (containing head-direction cells, (Solstad et al., 2008; Tang et al., 2016)) relate to the patchy architecture in layer 2 of MEC. Injections of the anterograde tracer BDA (3000 molecular weight) showed that parasubicular neurons extend long axons throughout the full length of the parasubiculum (Fig. 2.9A), consistent with previous evidence from single-cell microcircuits (Burgalossi et al., 2011). As a consequence of this internal connectivity, a single tracer injection could label the full extent of the parasubiculum (Fig. 2.9B top). Furthermore, we observed heavy staining of layer 2 of the MEC (Fig. 2.9B bottom). To determine whether parasubicular axons target a specific subpopulation of neurons in layer 2 of MEC, we performed fine-scale injections of anterograde tracers in the dorsal parasubiculum, combined with visualization of calbindin patterns (Fig. 2.9C-E). Surprisingly, calbindin^{+} patches were selectively innervated by parasubicular afferents (Fig. 2.9C-D), which targeted the center of patches (Fig. 2.9E). This indicates that parasubicular axons may preferentially provide input to layer 2 pyramidal neurons of MEC, which could convey head-direction information.

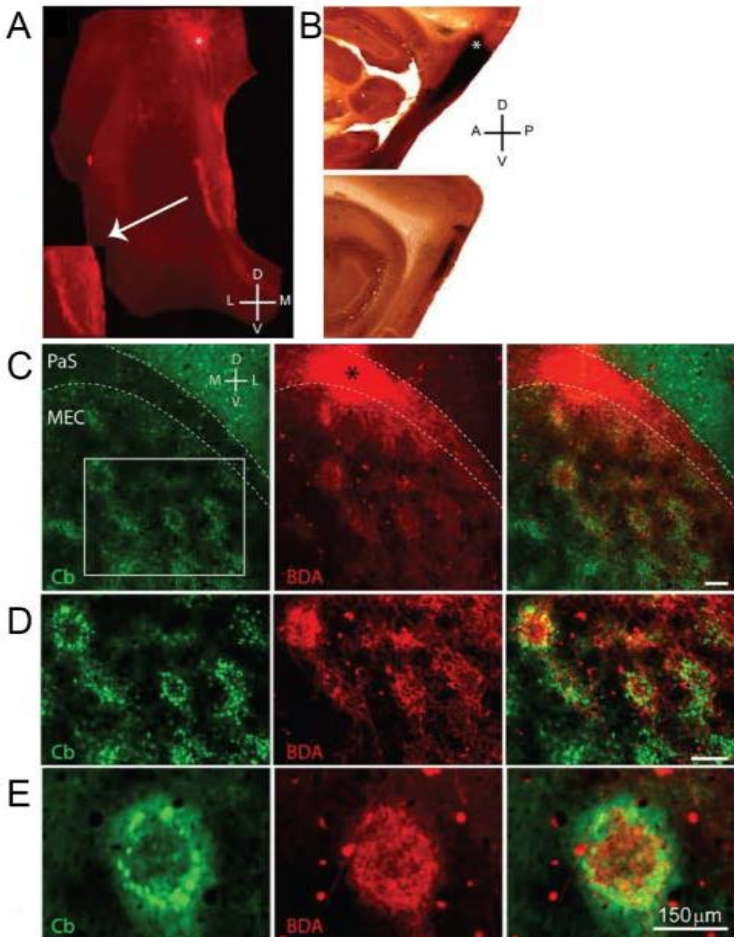

Figure 2.9: Internal structure of the parasubiculum. Parasubicular axons target layer 2 pyramidal cell patches in medial entorhinal cortex.
(A) Tangential sections of the parasubiculum showing the injection site of BDA tracer (red fluorescence) and anterogradely traced circumcurrent axons (according to the terminology of (Burgalossi et al., 2011)), extending throughout the parasubiculum (see also magnified inset, left). **(B)** Parasagittal sections of the parasubiculum (top) and parasubiculum and MEC (bottom) after the injection of larger amounts of BDA (tracer, dark color). The tracer completely fills the parasubiculum and stains layer 2 of the MEC. **(C)** Left, Tangential section stained for calbindin (green) revealing patches of calbindin^{+} pyramidal neurons. Middle, Same section as left processed to reveal the tracer BDA (red). Right, Overlay. **(D)**, Same as C but at higher magnification. **(E)** High-magnification view of a single patch. (*) Location of the parasubicular injection sites. Scale bars, (C) to (E) 150 µm. D, Dorsal; L, lateral; M, medial; V, ventral; A, anterior; P, posterior. Adapted from (Tang et al., 2016).

2.3 Discussion

We studied the arrangement and properties of the two main principal cell types in rat medial entorhinal cortex layer 2. Non–dentate-projecting, calbindin-positive pyramidal cells bundled dendrites together and formed patches arranged in a hexagonal grid aligned to layer 1 axons, the dorsoventral extent of the parasubiculum, and cholinergic and parasubicular inputs. Calbindin-negative, dentate-gyrus–projecting stellate cells were distributed across layer 2 but avoided centers of calbindin-positive patches.

We have hypothesized that calbindin$^+$ neurons form a "grid-cell-grid" (Brecht et al., 2014) - that their hexagonal arrangement might be an isomorphism to hexagonal grid cell activity, much like isomorphic cortical representations of body parts in tactile specialists (Catania et al., 1993; Woolsey and Van der Loos, 1970). However, hexagonality often results from spacing constraints and hence might be unrelated to grid cell activity. Determining the spatial modulation patterns of identified entorhinal neurons will help clarifying whether and how the calbindin$^+$ grid is related to grid cell activity.

The reported morphological differences (dendritic size and shape, inhomogeneous spine distribution), together with clustering of calbindin$^+$ cells in patches and the polarization of their apical dendrites toward the center of calbindin$^+$ patches, likely result in a local and overlapping sampling of inputs in neighboring calbindin$^+$ cells, whereas neighboring calbindin$^-$ stellate cells sample large and non-overlapping input territories. Recognizing the functional dichotomy of pyramidal and stellate cells in layer 2 will help elucidate how spatial discharge patterns arise in cortical microcircuits.

In addition to these anatomical findings, the functional results (not shown here) indicate that the strongly theta-rhythmic parasubicular neurons project selectively into layer 2 pyramidal cell patches (Tang et al., 2016), where neurons show strong entrainment by the theta rhythm (Ray et al., 2014) and where most grid cells might be located (Tang et al., 2014b). This could indicate a focus of grid cell activity in pyramidal cell patches. Results about inter-class connectivity ((Couey et al., 2013; Fuchs et al., 2016; Winterer et al., 2017), see Chapter 3 of this thesis) would however predict that (given inhibitory gating) grid cell activity could spread across the cell types in MEC. It thus still needs to be assessed how these two distinct principal cell networks contribute to grid cell activity.

2.4 Materials and methods

All experimental procedures were performed according to German guidelines on animal welfare.

2.4.1 Brain tissue preparation

For anatomy experiments, male and female Wistar rats (150-400 g) were anesthetized by isoflurane, and then euthanized by an intraperitoneal injection of 20% urethane. They were then perfused transcardially with 0.9% phosphate buffered saline solution, followed by 4% paraformaldehyde (PFA) in 0.1 M phosphate buffer (PB). After perfusion, brains were removed from the skull and postfixed in PFA overnight. They were then transferred into a 10% sucrose solution in PB and left overnight, and subsequently immersed in 30% sucrose solution for at least 24 hours for cryoprotection. The brains were embedded in Jung Tissue Freezing Medium, and subsequently mounted on the freezing microtome to obtain 20-60 µm thick sagittal sections or tangential sections (parallel to the pial surface). Tangential sections of the medial entorhinal cortex were obtained by separating posterior cortices (including the entorhinal cortex) from the remaining hemisphere by a cut parallel to the surface of the medial entorhinal cortex. The tissue was then frozen and positioned with the pial side to the block face of the microtome.

2.4.2 Histochemistry and immunohistochemistry

Acetylcholinesterase (AChE) activity was visualized according to previously published procedures (Ichinohe et al., 2008; Tsuji, 1998). After washing brain sections in a solution containing 1 ml of 0.1 M citrate buffer (pH 6.2) and 9 ml 0.9% NaCl saline solution (CS), sections were incubated with CS containing 3 mM CuSO4, 0.5 mMK3Fe(CN)6, and 1.8 mM acetylthiocholine iodide for 30 min. After rinsing in PB, reaction products were visualized by incubating the sections in PB containing 0.05% 3,3'- Diaminobenzidine (DAB) and 0.03% nickel ammonium sulfate.

Immunohistochemical stainings were performed according to standard procedures. Briefly, brain sections were pre-incubated in a blocking solution containing 0.1 M PBS, 2% Bovine Serum Albumin (BSA) and 0.5% Triton X-100 (PBS-X) for an hour at room temperature (RT). Following this, primary antibodies were diluted in a solution containing PBS-X and 1% BSA. Primary antibodies against the calcium binding proteins Calbindin (1:5000), the extracellular matrix protein Reelin (1:1000), the extrinsic membrane protein Myelin Basic Protein (1:1000), the vesicular acetylcholine transporter (1:1000), and the DNA binding

neuron specific protein NeuN (1:1000) were used. Incubations with primary antibodies were allowed to proceed for at least 24 hours under mild shaking at 4°C in free-floating sections. Incubations with primary antibodies were followed by detection with secondary antibodies coupled to different fluorophores (Alexa 488 and 546). Secondary antibodies were diluted (1:500) in PBS-X and the reaction was allowed to proceed for two hours in the dark at RT. For multiple antibody labeling, antibodies raised in different host species were used. After the staining procedure, sections were mounted on gelatin coated glass slides with Mowiol or Vectashield mounting medium.

In a subset of experiments, primary antibodies were visualized by DAB staining. For this purpose, endogenous peroxidases were first blocked by incubating brain tissue sections in methanol containing 0.3% hydrogen peroxide in the dark at RT for 30 min. The subsequent immunohistochemical procedures were performed as described above, with the exception that detection of primary antibodies was performed by biotinylated secondary antibodies and the ABC detection kit. Immunoreactivity was visualized using DAB staining.

For whole-mount immunohistochemistry we used a variant of the protocol in (Jährling et al., 2008; Sillitoe and Hawkes, 2002). Thick tangential sections (~ 300 µm) containing layer 2 of the MEC were first post-fixed in Dent's fixative overnight at 4°C and then incubated in Dent's bleach overnight at 4°C. They were then dehydrated twice in 100% methanol for 30 min each and then rehydrated for 90 min each in 50% and 15% methanol in PBS at RT. Subsequently, sections were incubated with 10 µg/ml proteinase K for 5 min at RT. Sections were then rinsed three times for ten minutes in PBS at RT and subsequently incubated in PBS-X containing 2% BSA overnight. Primary antibodies were diluted in PBS-X containing 5% DMSO, 1% BSA and incubated for 96 hours at 4°C. After this incubation, whole-mounts were washed in PBS-X three times for 2–3 h each and then incubated overnight in secondary antibodies diluted in PBS-X and 5% DMSO at 4°C. Sections were then washed three times in PBS-X for 2–3 h each and incubated in PBS-X overnight to ensure efficient removal of unbound antibodies. The sections were dehydrated in series of 50%, 80%, and 100% methanol in PBS at RT for 90 min each. Finally, the sections were transferred for at least 2 days into a clearing solution consisting of two parts of benzyl benzoate and one part of benzyl alcohol at RT, until they became transparent.

For histological analysis of juxtacellularly-labeled neurons, neurobiotin was visualized with streptavidin conjugated to Alexa 546 (1:1000). Subsequently, immunohistochemistry for Calbindin was performed as described above and visualized with Alexa Fluor 488. After fluorescence images were acquired, the neurobiotin staining was converted into a dark DAB

reaction product, performed as previously described (Klausberger et al., 2003). This has advantages of being more sensitive than most fluorescent dyes, is permanent and not sensitive to photobleaching (Marx et al., 2012). In general we found similar results for calbindin immunohistochemistry as previous authors (Langston et al., 2010; Varga et al., 2010), who showed that the large majority (~90% in (Langston et al., 2010)) of calbindin+ cells are glutamatergic neurons.

2.4.3 Retrograde and Anterograde Neuronal Labeling

Retrograde tracer solutions containing either Biotynilated-Dextrane Amine (BDA) (10% w/v; 3.000 MW) or Cholera Toxin Subunit B, Alexa Fluor 488 Conjugate (CTB) (0.8 % in PB) were injected in juvenile rats (~150 gr) under ketamine/xylazine anesthesia. Briefly, a small craniotomy was opened above the dentate gyrus at intermediate positions along the septotemporal axis. Animals were placed in a stereotaxic apparatus, and prior to injection, the granule cell layer was localized by electrophysiological recordings, based on characteristic signatures of the local field potential and neuronal spiking activity. Glass electrodes with a tip diameter of 10- 20 μm, filled with CTB or BDA solution, were then lowered unilaterally into the target region. Tracers were either pressure-injected (CTB; 10 injections using positive pressure of 20 p.s.i., 10- 15 s injection duration) or iontophoretically-injected (BDA; 7s on/off current pulses of 1-5 mA for 15 min). After the injections, the pipettes were left in place for several minutes and slowly retracted. The craniotomies were closed by application of silicone and dental cement. The animals survived for 3-7 days before being transcardially perfused. The results from backlabeling agreed with previous authors (Germroth et al., 1989; Peterson et al., 1996; Tamamaki and Nojyo, 1993), who also found that the large majority of retrogradely-labeled neurons from the dentate gyrus had stellate morphologies.

2.4.4 Image acquisition

A microscope equipped with a motorized stage and a z-encoder, was used for bright field microscopy. Images were captured using a MBF CX9000 camera using Neurolucida or StereoInvestigator. Confocal and epifluorescence microscopes with camera were used to image the immunofluorescent sections. Alexa fluorophores were excited using the appropriate filters (Alexa 488 – L5, Alexa 546 – N3, Alexa 633 – Y5). Fluorescent images were acquired in monochrome, and colour maps were applied to the images post acquisition. Whole-mount stainings were imaged using a microscope. Fluorescence images were

acquired with a 25x (1.05 NA) water-immersion objective. A femtosecond laser was used to excite fluorophores at 850 nm. Post hoc linear brightness and contrast adjustment were applied uniformly to the image under analysis.

2.4.5 Cell Counts and Patch Sizes

In the analysis for determining cell numbers and patch sizes, patches in consecutive sections were matched by overlaying them in Adobe Photoshop, and only the ones which could be reliably followed in all the sections under consideration were taken up for further analysis. Image stacks were first converted into .tiff files for different channels and focal planes using ImageJ. These files were then merged back together into a single file using the Neurolucida image stack module. In these patches all cells positive for Calbindin and NeuN were counted manually.

Quantification of patch sizes was done with the Neurolucida software by using the mean of maximum and minimum Feret diameter, defined as the maximum and minimum diameter of the patch, respectively. To correct for overestimation of neurons due to double counting in two adjacent sections, we estimated the number of cells in a section assuming uniform cell density and uniform spherical cell shape in the section and applied a correction factor of s / (s+d) where, s is the section thickness and d is the diameter of a cell, to correct for the cells which would be counted again in an adjacent section.

2.4.6 Quantification of axonal orientation and cholinergic boutons

To quantify the orientation of axonal fibers in layer 1, axon segments from myelin-stained sections were traced using Neurolucida software. The polar histogram in Fig. 2.7G was constructed with angular bins of 3°, and the total length of axons in each angular direction was summed up. Using Stereoinvestigator software we quantified the density of VAChT-positive puncta in calbindin patch and non-patch areas at the layer 1/2 border in tangential sections from five rats. In total, we selected 10 regions of interest (ROI) centered on calbindin patches and 10 ROIs positioned equidistant between calbindin patch centers. All VAChT positive puncta in the ROI were counted manually and divided by area size to obtain puncta density.

To assess the colocalization of VAChT puncta and calbindin+ and calbindin- dendrites, we labeled neurons in vivo juxtacellularly and identified the cells based on their calbindin immunoreactivity. We calculated the proximity histograms of the closest distance between VAChT puncta and dendrite segments (35 calbindin+ and 25 calbindin- segments), at 50

µm and 100 µm from the soma (5 calbindin+ and 5 calbindin- cells from 4 brains). The histograms were normalized by dendritic length to obtain the number of VAChT-positive puncta per µm. The proximity analysis between VAChT puncta and dendritic segments was done in two ways: 1. We measured the closest distance of VAChT puncta to the dendrite shaft. 2. We measured the distance of the VAChT-positive puncta to the closest spine. Both results give rise to the same conclusion. Here, we show the results of analysis 1 only.

2.4.7 Analysis of Spatial Periodicity

To determine the spatial periodicity of calbindin+ patches, we determined spatial autocorrelations and spatial Fourier spectrograms. The spatial autocorrelogram was based on Pearson's product moment correlation coefficient (as in (Sargolini et al., 2006)). Grid scores were calculated as previously described (Schwartz and Coleman, 1981) by taking a circular sample of the autocorrelogram, centered on, but excluding the central peak. The Pearson correlation of this circle with its rotation for 60 degrees and 120 degrees was obtained (on peak rotations) and also for rotations of 30 degrees, 90 degrees and 150 degrees (off peak rotations). Gridness was defined as in (Solstad et al., 2008) as the minimum difference between the on-peak rotations and off-peak rotations. To determine the grid scores, gridness was evaluated for multiple circular samples surrounding the center of the autocorrelogram with circle radii increasing in unitary steps from a minimum of 10 pixels more than the width of the radius of the central peak to the shortest edge of the autocorrelogram. The radius of the central peak was defined as the distance from the central peak to its nearest local minima in the spatial autocorrelogram. The grid score was defined as the best score from these successive samples (Solstad et al., 2008).

Grid scores reflect both the hexagonality in a spatial field and also the regularity of the hexagon. To disentangle the effect of regularity from this index, and consider only hexagonality, we transformed the elliptically distorted hexagon into a regular hexagon (Barry et al., 2012a) and computed the grid scores. A linear affine transformation was applied to the elliptically distorted hexagon, to stretch it along its minor axis, till it lay on a circle, with the diameter equal to the major axis of the elliptical hexagon. The grid scores were computed on this transformed regular hexagon. The spatial Fourier spectrogram was calculated by implementing a two-dimensional discrete Fourier transform and determining its power (Krupic et al., 2012).

To determine the probability that the patches present in the selected area would be arranged hexagonally, we employed a shuffling procedure and compared the maximum Fourier power of the block pattern representing the original image, to the 99th percentile of the power of a shuffled one with the same blocks (representing the patches) being randomly distributed in the same area without overlapping. This shuffling was performed on all samples on a sample-by-sample basis until the 99th percentile of the maximum power Fourier component converged to a constant.

2.4.8 Spine density measurement

To assess the spine density of calbindin+ and calbindin- dendrites, we labeled neurons in vivo juxtacellularly and identified the cells based on their calbindin immunoreactivity. We counted spines of fluorescent and DAB converted cells (10 calbindin+ and 10 calbindin- neurons) at 50 µm, 100 µm and 150 µm from the soma. The spine counts were normalized by dendritic length to obtain the number of spines per µm.

3 Axonal Synapse Sorting in Medial Entorhinal Cortex

This work was first published in:

Schmidt, H., Gour, A., Straehle, J., Boergens, K., Brecht, M., Helmstaedter, M. (2017). Axonal synapse sorting in medial entorhinal cortex. Nature, 549 (7673) :469-475.

This is the authors' version of the work.

3.1 Introduction

Ultrastructural analysis of cortical synaptic connectivity by electron microscopy has typically been limited to small volumes of tens of micrometers in extent (Ahmed et al., 1997; Genoud et al., 2006; Holtmaat et al., 2006; Kasthuri et al., 2015; Koganezawa et al., 2015; Mishchenko et al., 2010; van Haeften et al., 2003). Similarly, connectivity analysis using mutliple intracellular electrical recordings in brain slices is typically limited to testing small numbers of connections within an individual brain slice (Couey et al., 2013; Feldmeyer et al., 1999; Feldmeyer et al., 2002; Fuchs et al., 2016; Helmstaedter et al., 2008d; Jiang et al., 2015; Markram et al., 1997a; Markram et al., 1997b). Only recently, larger-scale high resolution 3-dimensional imaging of neuronal circuits using electron microscopy has become feasible in volumes extending to several hundred micrometers in at least two dimensions (Bock et al., 2011; Briggman et al., 2011; Helmstaedter et al., 2013; Lee et al., 2016; Wanner et al., 2016b), which was previously unique to electrical recordings. These approaches allow studying locally complete synaptic in- and output maps. Especially for mapping synapses along axons, the path length of the reconstructed axon is the key constraining factor – and this is limited by the smallest of the 3 imaged and reconstructed dimensions (40-52 µm in previous studies in cortex, (Bock et al., 2011; Kasthuri et al., 2015; Lee et al., 2016), see (Helmstaedter, 2013)).

Here we used serial blockface scanning electron microscopy (SBEM, (Denk and Horstmann, 2004)) and skeleton-based connectomic data analysis (Helmstaedter et al., 2011) to investigate the neuronal circuitry in layer 2 of rat medial entorhinal cortex (MEC) in 3-dimensional EM datasets whose smallest dimensions were 274 µm (juvenile 25-day old rat) and 101 µm (adult 90-day old rat).

Previous electrical recording studies of MEC (Couey et al., 2013; Fuchs et al., 2016) had found connectivity between excitatory neurons to be absent (Couey et al., 2013) or sparse (Fuchs et al., 2016), suggesting types of attractor models in MEC based on purely inhibitory connectivity between excitatory neurons (Couey et al., 2013). We find that at least 30% of the output synapses of excitatory neurons are made onto other excitatory targets. This excitatory connectivity was distance-dependent: when investigating the output synapses of excitatory neurons in L2 along the neurons' axons, we find that inhibitory neurons are targeted first, offset by about 120 µm along the path length of the axon to the innervation of excitatory neurons (path length-dependent axonal synapse sorting, PLASS). We

furthermore find that axons frequently provide multiple innervations to the same postsynaptic dendrites in close proximity, further enhancing the ability to activate the postsynaptic neurons at high temporal precision in a cellular feedforward inhibition circuit. These results reveal a new level of synaptic specialization in the cerebral cortex beyond average cell-to-cell connectivity and emphasize the need for high-resolution connectomic circuit mapping. Using numerical simulations, we show that this circuit could enhance spike timing precision, and could control the propagation of synchronized activity.

3.2 Results

3.2.1 Tree-dimensional electron microscopy experiment

We acquired and densely reconstructed (Fig. 3.1a-c) two 3-dimensional EM datasets: one sized (424 x 429 x 274) μm^3 from the medial entorhinal cortex (MEC) of a P25 male rat (Fig. 3.1b,c) at a voxel size of (11.24 x 11.24 x 30) nm^3 (increased to (11.24 x 11.24 x 50) nm^3 for the final 56 µm of the dataset) and one sized (183 x 137 x 158) μm^3 from MEC of a P90 male rat (Fig. 3.2a; note that analysis of the P90 dataset was already performed when 101 µm in the third dimension had been acquired) at a voxel size of (11.24 x 11.24 x 30) nm^3 using a serial blockface scanning EM (SBEM, (Denk and Horstmann, 2004)). For the acquisition of the large P25 dataset, the EM was equipped with a custom-built microtome that we modified for continuous stage movement, which increased the effective acquisition speed to about 6 MVx/s (Fig. 3.2d-h, for details see section 3.4 Methods; the P90 dataset was acquired using conventional mosaic-based imaging). The tissue blocks were stained using enhanced en-bloc staining (Hua et al., 2015) to provide high image contrast over the entire tissue block size. The tissue adjacent to the sample was stained for Calbindin immunoreactivity (Fig. 3.2b,c), confirming the location in dorsal MEC and the relationship to the patches of pyramidal neurons in MEC layer 2 (Kitamura et al., 2014; Ray et al., 2014).

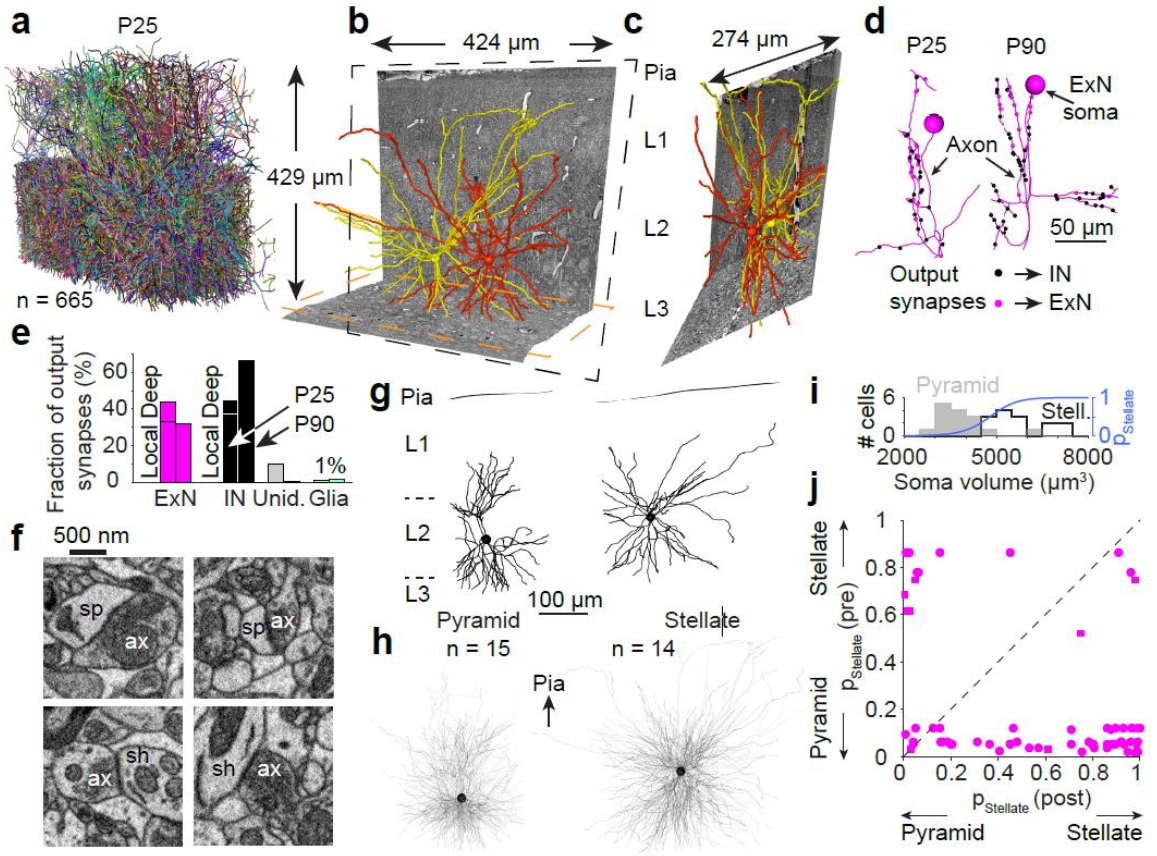

Figure 3.1: EM-based connectomic analysis in rat medial entorhinal cortex (MEC).
(**a-c**) 665 neurons in cortical layers 2,3 (L2,L3) skeleton-reconstructed (Boergens et al., 2017) (a) to analyze local circuitry within a 3D EM dataset of MEC L2 of a P25 rat (b,c). Reconstruction of 2 example excitatory neurons in L2 (yellow, red) together with raw EM data and dataset boundaries (dashed lines). (**d**) Example reconstruction of somata and axons with all local output synapses targeting interneurons (INs, black) and excitatory neurons (ExNs, magenta) from the P25 dataset (left, see a-c) and for an additional 3D EM dataset obtained from a 90 day old rat (P90, right, Fig. 3.2a). (**e**) Target distribution of output synapses (n=310 in P25, n=284 in P90) of ExNs (n=15 in P25, n=7 in P90); local: local target; deep: dendrite from deep layers; unid.: unaccounted spines for which the continuation to the target dendrite was not uniquely identifiable; Glia: glial targets. **(f)** Example EM micrographs of excitatory synapses made from presynaptic axons (ax) onto spines (sp, top) and shafts (sh, bottom), for criteria of synapse identification in SBEM, see (Staffler et al., 2017). (**g**) Classification of ExNs into pyramidal neurons (left) and stellate cells (right) based on dendritic morphology. (**h**) Superposition of soma and dendrites of pyramidal (left, n=15) and stellate (right, n=14) neurons for which expert consensus of cell type classification was reached (see Fig. 3.3). (**i**) Distribution of soma volume for consensus-classified pyramidal (gray) and stellate cells (black) in (h) and ensuing likelihood to encounter a stellate cell given soma volume ($p_{stellate}$, blue). (**j**) Map of synaptically connected ExN-to-ExN cell pairs (circles, P25; squares, P90) and the respective $p_{stellate}$ (pre: presynaptic; post: postsynaptic). Scale bars: 50 µm (d), 500 nm (f), 100 µm (g,h). From (Schmidt et al., 2017).

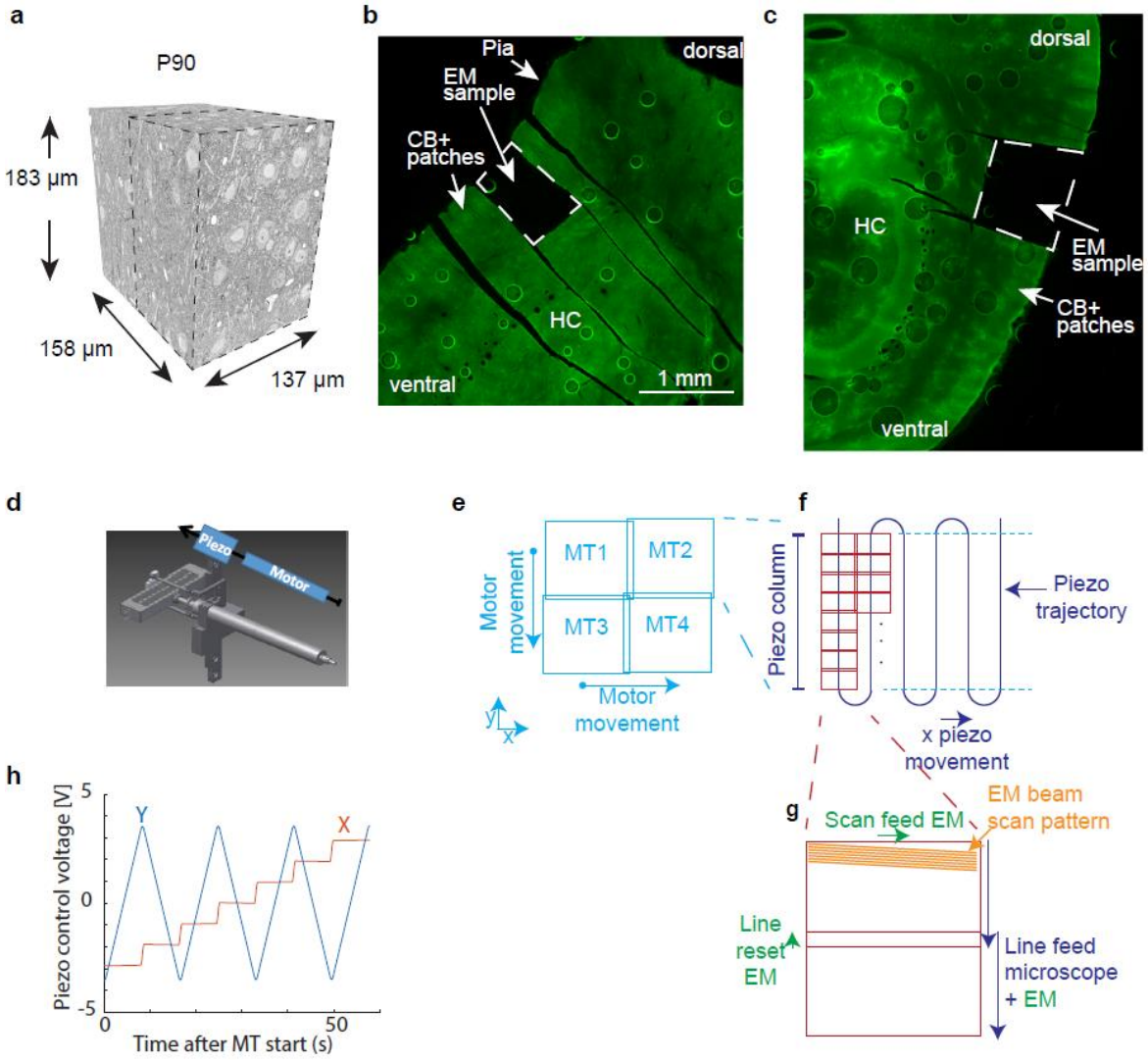

Figure 3.2: P90 dataset, Calbindin immunohistochemistry and continuous serial block-face electron microscopy imaging (SBEM).
(**a**) Dimensions of the P90 SBEM dataset (pia, top). Dashed bounding box: initial 101 µm in z after which analysis was started. (**b,c**) Confirmation of sample location in dorsal MEC. Post-hoc CB+ staining of the remaining tissue after EM sample extraction for P25 dataset (b) and P90 dataset (c). CB+ patches are visible close to the pia. HC: hippocampus. (**d-h**) Continuous SBEM imaging. (d) Sketch of microtome with piezo actor installed in-line with the geared motor. (e-g) Sketch of stage movement and imaging setup in continuous SBEM imaging. (h) Piezo actor command voltages during one motortile acquisition. See section 3.4 Methods for details. From (Schmidt et al., 2017).

3.2.2 Reconstruction of excitatory neurons

We then used the in-browser data annotation software webKnossos (Boergens et al., 2017) for neurite reconstruction. In the P25 dataset, dendrites could be followed through the entire dataset, and axons could be followed in large parts of the image volume (see section 3.4 Methods). In the P90 dataset dendrites and axons could be followed throughout (for calibration of traceability by multiple experts, see section 3.4 Methods). We first identified neuronal cell bodies in the datasets, asked a team of 24 student annotators to skeleton-reconstruct the dendrites of all these neurons (n=665 in P25, Fig. 3.1a-c, n=91 in P90; total traced path length 2.89 m, average redundancy 2.0, i.e. 1.45 m unique neurites reconstructed within 3654 work hours total using orthogonal tracing mode in webKnossos (Boergens et al., 2017). We first identified 22 excitatory neurons (ExNs, 15 in P25 and 7 in P90), for which we reconstructed their local axons (examples in Fig. 3.1d), yielding an average axonal path length per neuron of 555.4 µm (8.33 mm total) at P25 and 921.1 µm (6.44 mm total) at P90. Along these proximal axons, we identified all outgoing synapses (n=594 (P25: 310, P90: 284), Fig. 3.1d-f), their postsynaptic targets, and matched these to the reconstructed neurons in the dataset. If the synaptic target was a dendrite that had not yet been traced, we added this dendrite to the reconstruction (113 and 135 additional dendrites at P25 and P90, respectively; dendrite classification was based on rate of spines, calibrated to be >0.6 per µm for ExNs and <0.2 per µm for INs, see section 3.4 Methods). In the P25 dataset, 44% of these synapses were made onto excitatory neurons (ExNs), 45% onto interneurons (INs) (1% of the targets were glial cells; for the remaining 10% of synapses, the postsynaptic structure was identified to be a spine that could not be followed back to the respective dendrite). In the P90 dataset, 32% of synapses were made onto ExNs, 67% onto INs, and 1% onto glia. The fraction of synapses made onto INs is noteworthy, since interneurons (13% of the neuron population) are ~7 times less common than excitatory cells (87% of the neuron population) in medial entorhinal cortex (Tang et al., 2014b); this prevalence for IN targeting is in agreement with findings from paired intracellular recordings in brain slices of MEC (Couey et al., 2013; Fuchs et al., 2016). To confirm that synapse detection in SBEM data is identifying the expected range of synapse sizes, and is in particular not biased towards larger synapses, we measured the volume of a random subset of postsynaptic spines in the data (0.13±0.12 μm^3, n=20, P90 dataset), which is well in the range of so-far reported values (Kasthuri et al., 2015; de Vivo et al., 2017). It is noteworthy that studies using TEM appear to find smaller synapse sizes than those using SEM (compare data in (Harris et al., 1989; Arellano et al., 2007; Bopp et al., 2017) to

(Kasthuri et al., 2015; de Vivo et al., 2017; Staffler et al., 2017) and this study; one methodological caveat may be the precise determination of cutting thickness for volume estimates).

To investigate how the connectivity between ExNs related to the at least two main types of excitatory neurons in layer 2 of MEC, pyramidal and stellate cells (Fig. 3.1g), we first searched for neurons with a very clear dendritic morphology allowing a unanimous classification as either pyramidal (single apical dendrite pointed towards the pia, denser plexus of basal dendrites, Fig. 3.1g, see also Fig. 3.3) or stellate (multiple large primary dendrites without clear angular preference; independently assessed by two experts). We then evaluated previously proposed (Fuchs et al., 2016) morphological classification criteria on these two morphological classes (overlay in Fig. 3.1h) and found that in fact, the volume of the cell body was a strong predictor of cell type (n=15 (pyramidal) vs 14 (stellate); volume 3,837 ± 869 μm^3 vs 5,673 ± 934 μm^3, mean ± s.d., t-test, $P<10^{-5}$; Wilcoxon rank test, $P<10^{-4}$ Fig. 3.1i), yielding a simple "stellate probability" $p_{stellate}$ based on soma size for each neuron. When analyzing the ExN-to-ExN connectivity in relation to the likely cell type of the pre- and postsynaptic neurons, respectively (Fig. 3.1j, analyzed for those targets that had a soma in the dataset), we find strongest evidence for connections from pyramidal to stellate cells (n=30 of 54 for $p_{stellate}(pre)<0.25$ and $p_{stellate}(post)>0.75$), and stellate to pyramidal cells (n=5 of 9 for $p_{stellate}(pre)>0.75$ and $p_{stellate}(post)<0.25$), and some examples of pyramidal-to-pyramidal (n=12 of 54) and of stellate-to-stellate (n = 2 of 9) (see (Beed et al., 2010; Couey et al., 2013; Fuchs et al., 2016)). When analyzing the arrangement of output synapses of ExNs in more detail, though, we found the following surprising results, which were unrelated to the types of excitatory neurons.

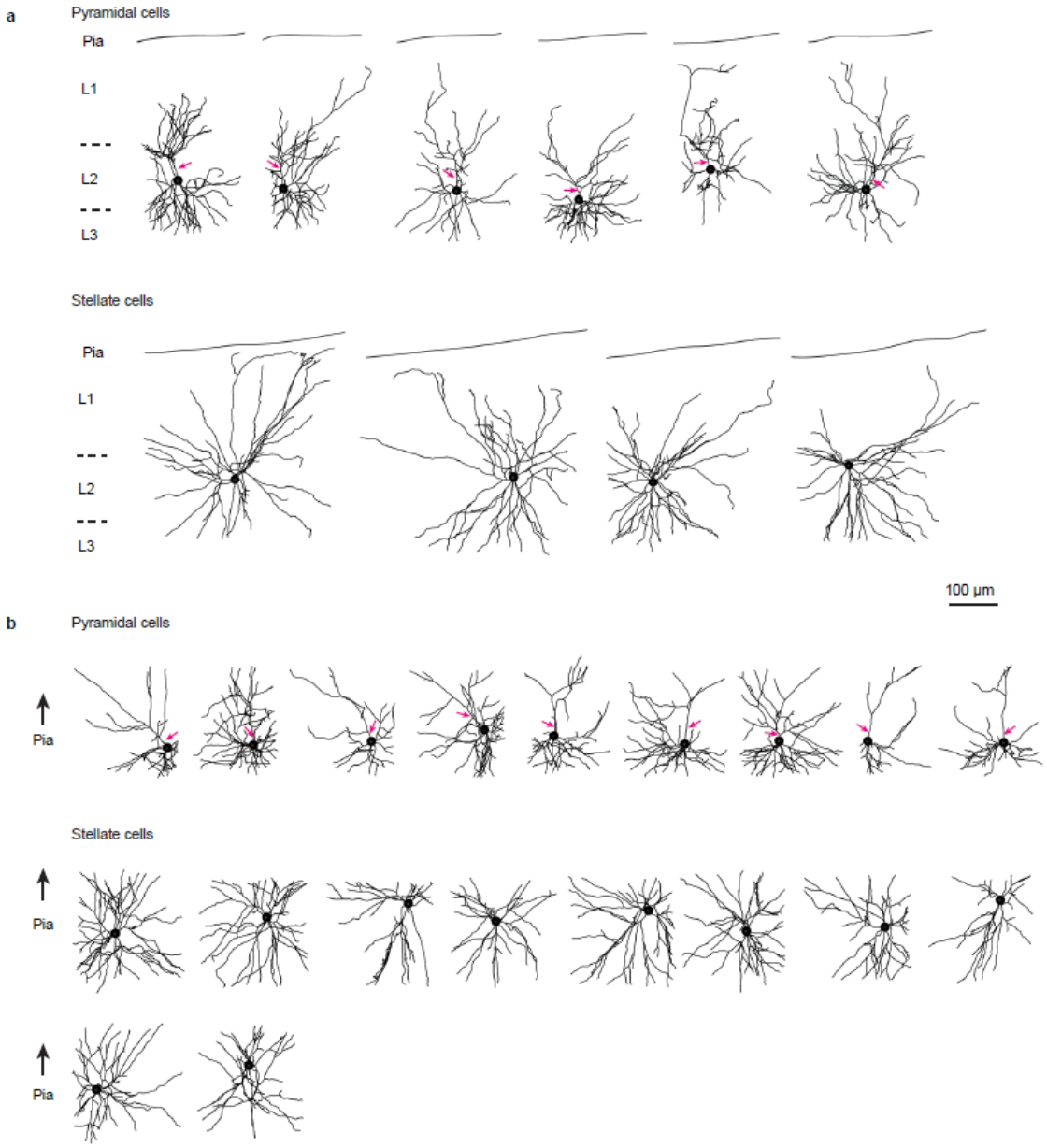

Figure 3.3: Gallery of EM-based reconstructions from P25 dataset.
(**a**) Pyramidal cells (top) and stellate cells (bottom) for which expert consensus was reached about cell type classification. Note apical dendrites (magenta arrows) and denser plexus of basal dendrites for pyramidal cells, and lack of a clear apical dendrite for stellate cells. (**b**) Same for locally reconstructed neurons. Scale bar 100µm (a and b). From (Schmidt et al., 2017).

3.2.3 Path length-dependent axonal synapse sorting

We investigated the relationship between synapse position along the presynaptic excitatory axon and the type of synaptic target (Fig. 3.4). We found that synapses targeting interneurons were made first along the path of the axon, while synapses targeting excitatory neurons were made later. This was the case for excitatory neurons both in the P25 (Fig. 3.4a-c, n=15 axons, n=136 (synapses onto excitatory) vs. n=140 (inhibitory targets), 264 ± 67 µm vs 215 ± 69 µm, mean ± s.d., t-test and Wilcoxon rank test, $P<10^{-8}$; randomization test, $P<10^{-3}$, Fig. 3.4c) and P90 dataset (Fig. 3.4d-f, n=7 axons, n=90 (synapses onto excitatory) vs. n=189 (inhibitory targets), 247 ± 43 µm vs 210 ± 45 µm, mean ± s.d., t-test and Wilcoxon rank test, $P<10^{-8}$; randomization test, $P<10^{-3}$, Fig. 3.4f) and was irrespective of the type of presynaptic excitatory neuron (Fig. 3.5a).

Could this unexpected axonal synaptic sorting be related to an inhomogeneous availability of postsynaptic targets in the neuropil surrounding the presynaptic neurons? To test for this, we first analyzed the distribution of output synapse targets when reported over their radial distance to the cell body of origin instead of their axonal path length distance (Fig. 3.4g). This analysis showed that the radial distances of output synapses were indistinguishable for excitatory (n=136) vs inhibitory (n=140) targets (82 ± 34 µm vs 85 ± 31 µm; mean ± s.d.; t-test, P=0.39 and Wilcoxon rank test, P=0.21, Fig. 3.4g). Similarly, the positional bias of synapses was not explained by distance to the centers of the presumed modules in L2 of MEC ("patches" in L2 of MEC (Ray et al., 2014), Fig. 3.5d-f). Next, we investigated the distribution of output synapses along the radial cortex axis (pointing from white matter to pia, Fig. 3.4h). In fact, output synapses to inhibitory targets were biased towards the bottom part of L2, while synapses to excitatory targets were biased towards the upper part of L2 (Fig. 3.5b). We therefore measured the relative density of inhibitory dendrites and excitatory dendrites in 7 volumes sized $(10\ \mu m)^3$ each, positioned at different cortical depths within L2 (Fig. 3.5b,c). While the fraction of smooth dendrite path length decreased from 26% to 13% from lower L2 to upper L2, this difference could not account for the imbalance in synapse targets (Fig. 3.4h, fraction of IN targeting synapses dropping from about 80% to about 20% from lower L2 to upper L2). The about 4-fold (Fig. 3.4h) proximal bias of synapses onto INs thus cannot be achieved by a specific trajectory of the axon together with an innervation rule that is homogeneous along the axon. Rather, these findings indicate an explicit target preference of proximal axonal synapses for interneurons.

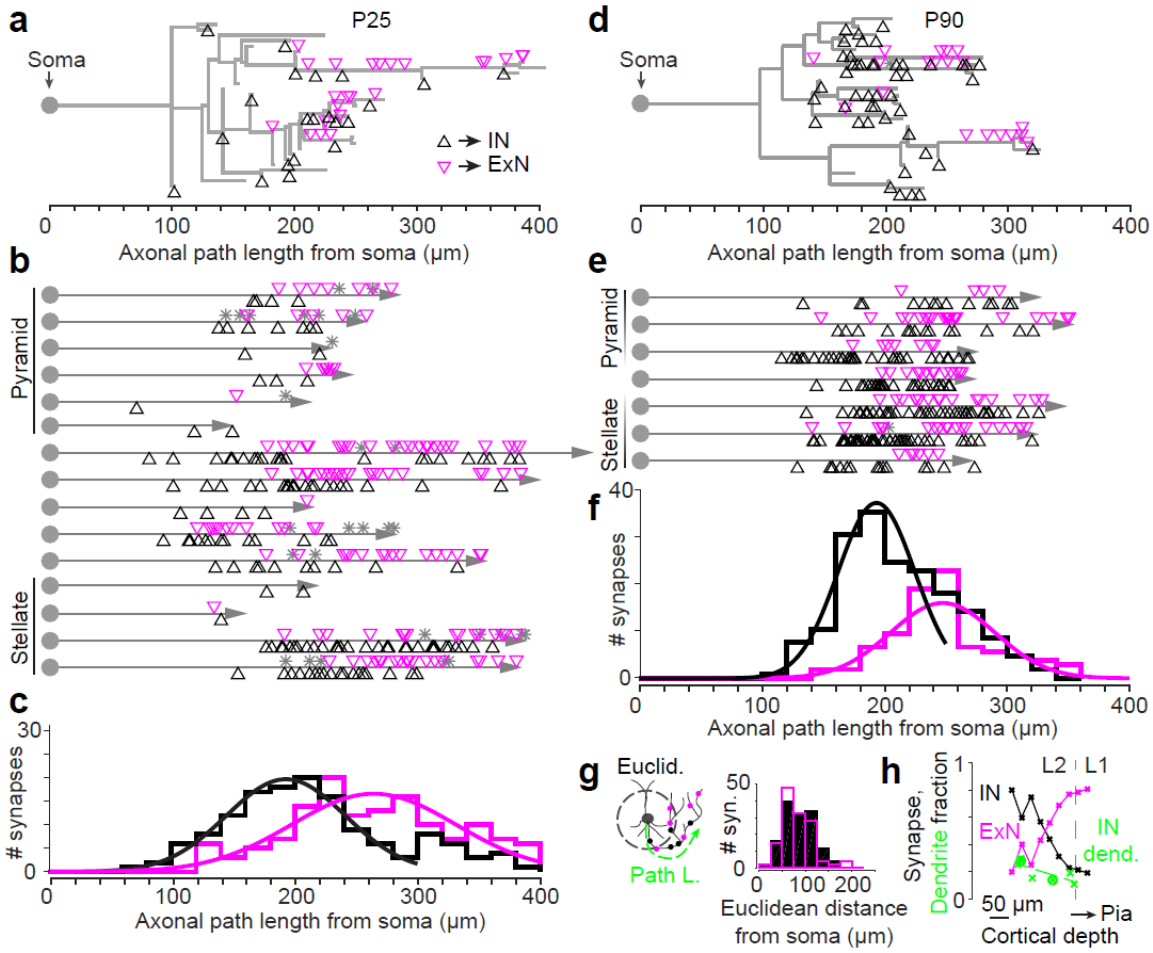

Figure 3.4: Path length-dependent axonal synapse sorting (PLASS) in medial entorhinal cortex.

(**a**) Example axonogram of one ExN with output synapses (triangles) onto INs (black) and ExNs (magenta), reported over axonal path length from soma. (**b,c**) Distribution of output synapses (n=307) over axonal path length to soma (15 ExN axons, P25) shows shift of inhibitory targets towards more proximal locations along the axon (n=136 (synapses onto excitatory) vs. n=140 (inhibitory targets)). Asterisk in b: unidentified synapses onto spine heads. Lines in c: Gaussian fits to the initial peaks of the distributions. See Fig. 3.5a for cell-type specific analysis. See also Fig. 3.11e. (**d-f**) Corresponding to a-c, for the P90 dataset. Cells in e sorted by increasing $p_{stellate}$ (top to bottom, see Fig. 3.1i and Fig. 3.3). (**g**) Summed distribution of output synapses along P25 ExN axons (as in c) analyzed over Euclidean (radial) distance to ExN soma at which the axon originates. Note the Euclidean distance distribution is indistinguishable for excitatory (magenta, n=136) vs inhibitory (black, n=140) targets, indicating the synaptic sorting is specific to the axonal path length (c,f). (**h**) Fraction of ExN output synapses made onto dendritic shafts (black) vs spines (magenta) over cortical depth (see Fig. 3.5b). The fractional path length of smooth dendrites sampled at 7 different cortical locations is also shown (green, Fig. 3.5c). Note that while the fraction of smooth dendrites is about 2-fold higher in lower L2 than in upper L2, its gradient cannot account for the about 4-fold bias of output synapses onto INs in lower L2 (black vs green lines). Green dashed line: linear fit to the IN dendrite fractions sampled as indicated in Fig. 3.5b,c (n=7). From (Schmidt et al., 2017).

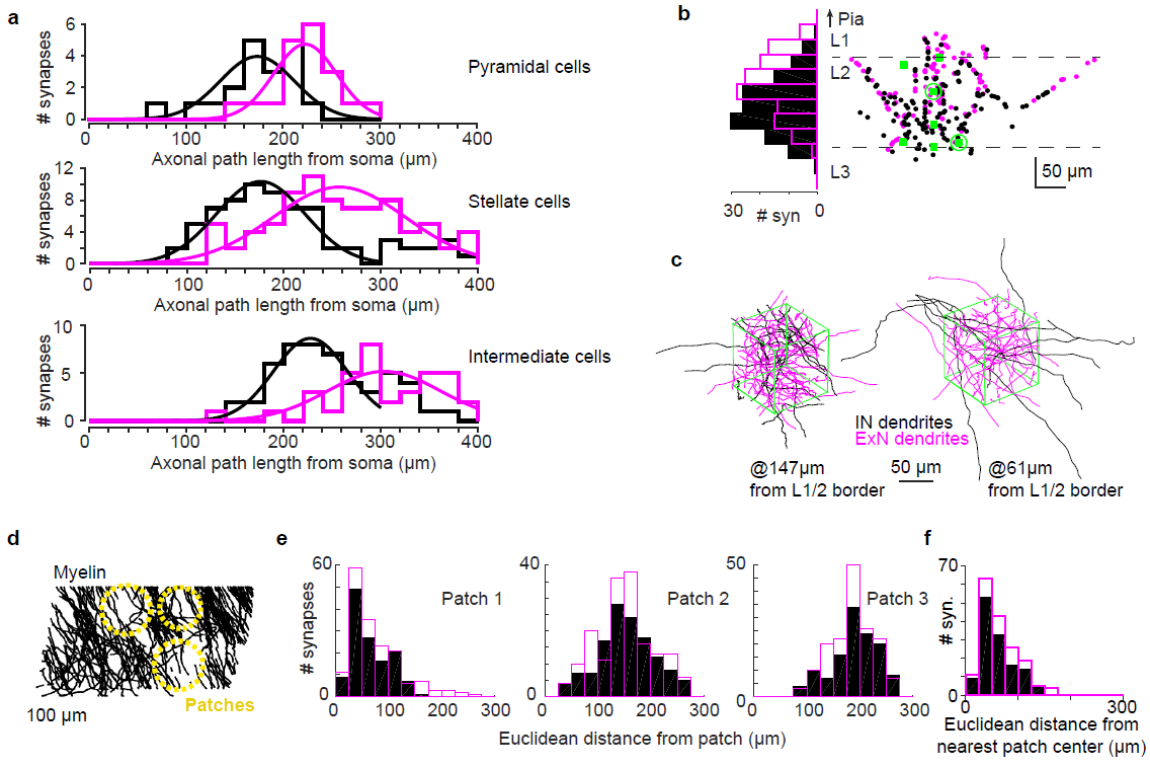

Figure 3.5: PLASS in dependence of cell types and synapse positions in relation to the cortical axis of MEC and patches.

(**a**) Position of output synapses along presynaptic ExN axons analyzed separately for consensus pyramidal cells (top, n=6 axons, n=19 (synapses onto excitatory) vs. n=19 (inhibitory targets), 222 ± 32µm vs 173 ± 38µm, mean ± s.d., t-test, Wilcoxon rank test and randomization test, $P<10^{-3}$), stellate cells (middle, n=4 axons, n=36 (synapses onto excitatory) vs. n=51 (inhibitory targets), 303 ± 58µm vs 249 ± 53µm, mean ± s.d., t-test, Wilcoxon rank test, randomization test, $P<10^{-4}$; randomization test, $P<10^{-3}$) and intermediate types (bottom, n=5 axons, n=81 (synapses onto excitatory) vs. n=70 (inhibitory targets), 257 ± 68µm vs 202 ± 75µm, mean ± s.d., t-test, Wilcoxon rank test, randomization test, $P<10^{-5}$; randomization test, $P<10^{-3}$). Note that all ExNs exhibit PLASS. (**b**) Output synapses along radial cortex axis (cortical depth, histogram on the left) and in paracoronal plane of MEC (right, plane of imaging, see Fig. 3.1a). Synapse distribution along cortical depth shows a bias of inhibitory targets towards deeper L2 (n=15 axons, n=136 (synapses onto excitatory) vs. n=140 (inhibitory targets), 223 ± 47µm vs 189 ± 45µm, mean ± s.d., t-test, $P<10^{-8}$; note that offset of depth values is close to the lower end of dataset, thus higher values mean closer to pia). Green, location of 7 cubes sized 10x10x10 μm^3 each in which dendrites were densely reconstructed. Green circles: dense reconstructions shown in c. (**c**) Skeleton reconstructions of all dendrites within a 10x10x10 μm^3 cube sampled at about 150µm (top) and about 60µm (bottom) from L1/2 border. IN dendrites, black; ExN dendrites, magenta. (**d**) Reconstruction of all myelinated axons (black) in L1 and upper L2, projected in the tangential plane. Yellow: circular areas of low myelin density previously identified with the patches of calbinbin$^+$ neurons in MEC (Ray et al 2014). (**e,f**) Distribution of distance of synapses to each of the 3 patch centers (e) and to the nearest patch center (f). Note that no distance bias for IN (black) vs ExN (magenta) targeting synapses can be seen. Scale bar, 50µm (b, c), 100µm (d). From (Schmidt et al., 2017).

3.2.4 Cellular feed-forward inhibition

What is the potential circuit context in which PLASS operates? We investigated the inhibitory neurons that receive input from the proximal output synapses of the excitatory axons (Fig. 3.6). Specifically, we wanted to know whether the PLASS-activated interneurons also target the very same excitatory neurons that the source neuron targets (Fig. 3.6a) – or whether these interneurons would exclude the subset of excitatory neurons that were targeted by the excitatory source neuron (Fig. 3.6b). The latter would amount to an exclusive opponent or lateral inhibition, the former would constitute cellular feed-forward inhibition in the PLASS target circuit. Such a cellular feedforward inhibitory circuit has so far not been demonstrated in cortex and could allow precise control of spike timing in the postsynaptic neuron (see below).

Fig. 3.6c shows the soma and dendrite of one presynaptic ExN together with all its 11 local excitatory target neurons. The PLASS-activated interneuron is also shown. In fact, 10 of 11 of these targets were also innervated by that very interneuron. In the entire population, 76% (32 of 42) connections between excitatory neurons were matched by PLASS-activated interneuron innervation involving one to three interneurons (Fig. 3.6d, a total of n=54 cFFI circuit motifs), showing a high prevalence of cellular feedforward inhibition in MEC L2. Given that we are biased in 3D EM imaging of limited volumes to miss synaptic connectivity due to incomplete axonal reconstructions, this data refutes an opponent inhibition model at $p<10^{-7}$ under biological wiring noise of up to 30% (see section 3.4 Methods). Even a random wiring between INs and ExNs is refuted at $p<10^{-3}$, yielding the cFFI model as the most likely explanation of the data.

But what is the potential functional significance of cellular feedforward inhibitory circuits? Feedforward inhibition has been described in several pathways in the mammalian brain, notably for the thalamocortical input to layer 4 (Bruno and Simons, 2002; Cruikshank et al., 2007), the mossy fiber input to cerebellar granule cells (Eccles et al., 1964; Kanichay and Silver, 2008), and non-local input to pyramidal cells in hippocampus (e.g. (Alger and Nicoll, 1982; Buzsaki, 1984)). In the latter circuit, feedforward inhibition was shown to enhance the precision of postsynaptic spike timing in CA1 pyramidal cells when activating the presynaptic excitatory axons (Pouille and Scanziani, 2001). However, in all of these settings, the presynaptic neuronal population was activated by bulk electrical stimulation, such that it could not be determined whether presynaptic neurons activating the postsynaptic

excitatory neuron were exactly the same ones as those activating the interneurons, or rather from the same population, but not identical at the single-cell level (population feedforward inhibition, pFFI, Fig. 3.6e). In the cerebellar circuit, recent data points to such a disjunct pFFI configuration (Duguid et al., 2015). By contrast, the cFFI configuration as found here in MEC (Fig. 3.6g) implies that the very same presynaptic neurons innervate both the postsynaptic ExN and in parallel the INs that provide FFI.

We therefore studied whether this cFFI circuit could further enhance spike timing precision when compared to the pFFI circuit (Fig. 3.6e-k). We performed numerical simulations of a circuit involving a presynaptic population of 60 ExNs that innervate 7 INs, which converge onto an ExN (Fig. 3.6e, the convergence and pool sizes were estimated from the connectivity reported in Fig. 3.1, see section 3.4 Methods). We modeled action potentials (APs) in the presynaptic population (using Poisson statistics and yielding about 2.5 APs per cell within 30 ms, Fig. 3.6f) and recorded the occurrence of APs in the INs (Fig. 3.6f middle). Then, both the excitatory and inhibitory presynaptic AP sets were used to model synaptic convergence in the postsynaptic ExN, and the time points of APs occurring in the postsynaptic ExN were recorded (Fig. 3.6f right; synaptic delays were set to 1 ms and were the same for IN and ExN targets). When only providing ExN input (no inhibition), the postsynaptic neuron was strongly activated (2.85 ± 0.02 APs per neuron per trial, Fig. 3.6i,k). When matched by pFFI, AP generation was reduced (Fig. 3.6i,k), and spike timing precision was enhanced (Fig. 3.6i,j). When however implementing the very same FFI circuit in the cellular FFI configuration (Fig. 3.6g), using the exact same presynaptic AP sequences to activate INs and ExN, not only statistically equivalent AP sequences as in the pFFI case (cf Fig. 3.6f), we found that APs in the postsynaptic ExN were about 2-fold rarer (0.16 ± 0.02 (cFFI) vs. 0.33 ± 0.04 APs / cell / trial (pFFI), mean ± s.d., t-test, $P<10^{-22}$, Fig. 3.6h,i,k), and the distribution of spike times further sharpened by about 2 ms (width of spike time histogram 7.9 ± 1.2 ms (cFFI) from 9.7 ± 1.1 ms under pFFI, mean ± s.d., n=4 different postsynaptic neuron models, n=2000 trials per cell, t-test, $P<10^{-4}$, Fig. 3.6i,j). Note that the model was equivalent in all parameters between pFFI and cFFI, only the presynaptic APs were drawn from the same statistics twice in pFFI (one for input to INs, one for input to ExNs) but only once for cFFI (exact same presynaptic population innervates INs and ExNs). This effect was stable for a large range of presynaptic pool sizes (spike time sharpening: stable for 50-80 ExNs and 5-10 INs, Fig. 3.7b; substantial spike rate reduction: stable for 30-80 ExNs, 7-10 INs, Fig. 3.7c). Thus cFFI can further enhance spike timing precision in

local circuits of MEC L2 under conditions of transiently substantial population activity (50-90 Hz presynaptic activity, Fig. 3.7d).

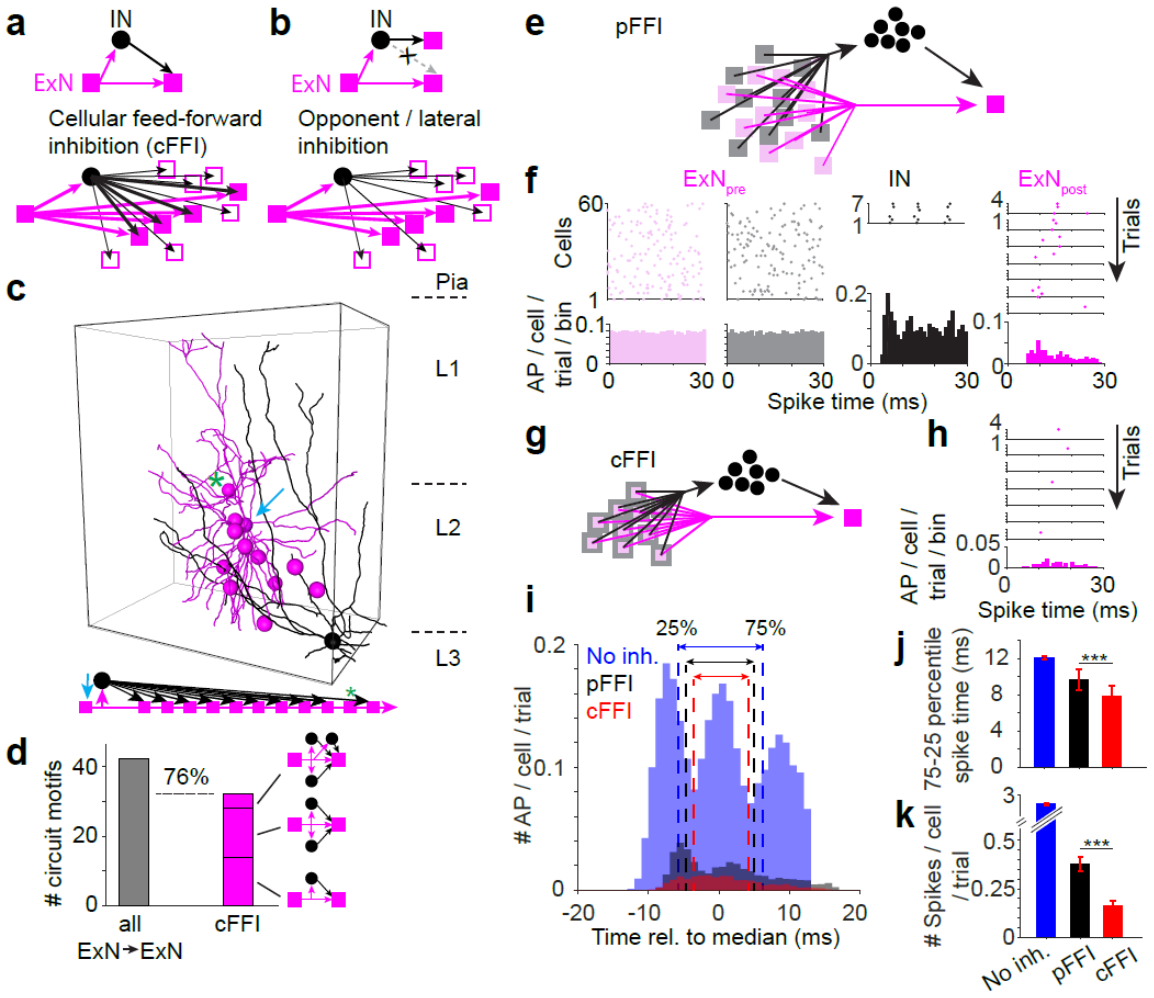

Figure 3.6: Local circuit patterns in layer 2 of medial entorhinal cortex.
Possible configuration of the PLASS circuit in MEC: INs targeted by the more proximal synapses of ExN axons could either target the very same ExNs (**a,** cellular feedforward inhibition, cFFI) or exclusively a different population of ExNs than the source ExN targets (**b,** opponent or lateral inhibition). (**c**) Example innervation of one presynaptic ExN (likely pyramidal cell, blue arrow; soma and dendrites shown) that targets 11 other ExNs (magenta, sequential positions in the bottom circuit sketch correspond to the ranked position of first established synapse along the presynaptic axon). Before targeting the ExNs, this ExN axon innervates an IN (black, soma and dendrites shown) that in turn innervates 10 of the same 11 ExN targets, providing direct evidence for cFFI in MEC. (**d**) Frequency of cFFI circuit motifs in the local connectome. cFFI motifs involving one to three INs are found in 76% (32 of 42) of ExN-to-ExN connections. Opponent inhibition was refuted (also see section 3.4 Methods). (**e**) Sketch of example circuit converging onto a postsynaptic ExN (magenta square) in population feedforward inhibition (pFFI) comprising a pool of presynaptic ExNs (light magenta) that target the postsynaptic ExN, in parallel to a pool of presynaptic ExNs (gray) from the same presynaptic population that target a pool of INs which in turn converge onto the postsynaptic ExN. Note that in the case of pure pFFI, the two sets of presynaptic neurons are disjunct (light magenta vs gray). (cont. next page)

(**f**) Simulated AP spike histograms for the presynaptic populations (left), the resulting simulated spike distribution in the IN population (single neurons, top, summed histogram over 100 trials, bottom) and the resulting simulated spike distribution in the target ExN (right top, 4 example cells). Note that statistics of spiking in presynaptic population are indistinguishable between both presynaptic populations (left). (**g**) Sketch of example circuit configured as cFFI. Note that presynaptic neurons that innervate the postsynaptic ExN are the exact same ones that innervate the pool of INs (as found in panels e-h). (**h**) Example simulated spike distribution (top: 4 modeled neurons, 6 repititions shown) and average spike histogram per stimulus (bottom) in cFFI configuration. The spike distribution of the presynaptic ExN population was as in f, gray panel; and thus the IN spike distribution as in f, black panel. Note the more narrow distribution and lower spike rate compared to pFFI (f, right). (**i**) Average simulated spike histogram of 4 cells (aligned to median per cell), 2000 trials each, for the conditions: no inhibition (blue), pFFI (black), cFFI (red). Arrows indicate width between 25th and 75th percentile. (**j,k**) Quantification of cFFI vs pFFI effects on the width of the postsynaptic AP timing distribution (j) and number of APs (k). Note that cFFI further suppresses AP rate compared to pFFI (by 2-fold, 0.16 ± 0.02 (cFFI) vs. 0.33 ± 0.04 APs / cell / trial (pFFI), mean ± s.d., t-test, ***P<10^{-22}) and narrows AP timing (by 1.8 ms, width of spike time histogram 7.9 ± 1.2 ms (cFFI) from 9.7 ± 1.1 ms under pFFI, mean ± s.d., n=2000 trials per cell, t-test, ***P<10^{-4}). See Fig. 3.7 for sensitivity of these effects on presynaptic neuronal pool sizes and presynaptic firing rates. Error bars: mean ± s.d (j,k). From (Schmidt et al., 2017).

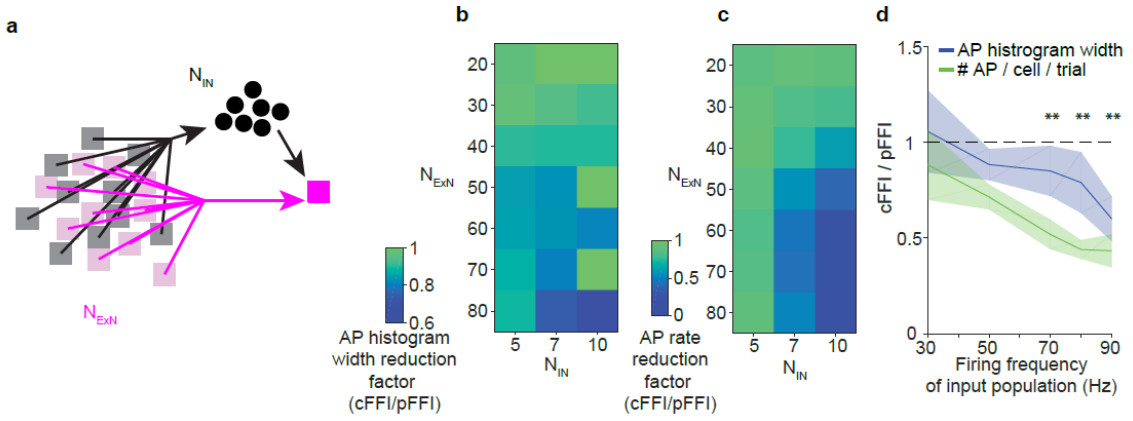

Figure 3.7: Comparison of population and cellular feed-forward inhibition with respect to postsynaptic spike timing and spike rate reduction, and presynaptic firing frequency.
(**a**) Sketch of example circuit converging onto a postsynaptic ExN (magenta square) in population feedforward inhibition (pFFI) comprising a pool of presynaptic ExNs (light magenta) that target the postsynaptic ExN, in parallel to a pool of presynaptic ExNs (gray) from the same presynaptic population that target a pool of INs which in turn converge onto the postsynaptic ExN. Note that in the case of pure pFFI, the two sets of presynaptic neurons are disjunct (light magenta vs gray). (**b**) cFFI effect on spike timing measured as the decrease in spike histogram width; relative reduction in 75th-to-25th percentile width is reported for cFFI vs pFFI, p<0.01 for N_{ExN} =50..80 and N_{IN} =5..7, t-test over 1000 trials per postsynaptic cell). (**c**) Relative reduction of spike rate in cFFI compared to pFFI. Note that spike rate reduction is most substantial (more than 2-fold) for presynaptic pool sizes of N_{ExN} = 60..80 and N_{IN} = 7..10 (p<10^{-5} for N_{ExN} =30..80 and N_{IN} =7,10; p<0.05 for N_{IN} =5; t-test over 1000 trials per postsynaptic cell). (**d**) Effect of presynaptic spike rate on cFFI effects. Note that for a range of 50..90 Hz presynaptic activity, both AP time histogram width and spike rate are significantly reduced compared to pFFI (**: p<0.01 for AP histogram width; p<10^{-6} for AP rate; one-sided t-test against 1). From (Schmidt et al., 2017).

3.2.5 Clustered postsynaptic innervation

We next asked whether the precise synapse positioning along the excitatory axons might be matched by a positional preference of these synapses on the target neurons' dendrites (see examples of such clustered innervation in (Kasthuri et al., 2015)). We found that the presynaptic excitatory axons in fact target the postsynaptic excitatory dendrites (Fig. 3.8a,b) as well as the postsynaptic inhibitory dendrites (Fig. 3.8c,d) with multiple closely spaced synapses. Quantified over all connections with more than one synapse ("multi-hit", Fig. 3.8e, P25 and P90), 76% (185 of 242) synapses were spaced at less than 10 µm distance from each other, and 82% (199 synapses) were spaced at less than 20 µm. Fig. 3.8c shows an extreme example of two presynaptic excitatory axons making each 8 and 10 synapses within about 52 µm onto the postsynaptic interneuron dendrite. Clustered synapses were on average 3.7 µm (onto ExNs) and 4.8 µm (onto INs) apart (inset in Fig. 3.8e). When also considering synaptic connections with just one synaptic contact (Fig. 3.8f; note that the number of synapses in these connections is most likely artificially reduced by axonal pruning based on 3D sample size), dendritic clustering occurs in at least 18% of all single- and multi-hit connections (12% for excitatory and 24% for inhibitory targets). This is more frequent than previously reported for supragranular layers of mouse V1 (Lee et al., 2016), where 9% of all connections were multi-hit connections, and an unreported fraction of these clustered (our multi-hit fraction was in contrast 21%).

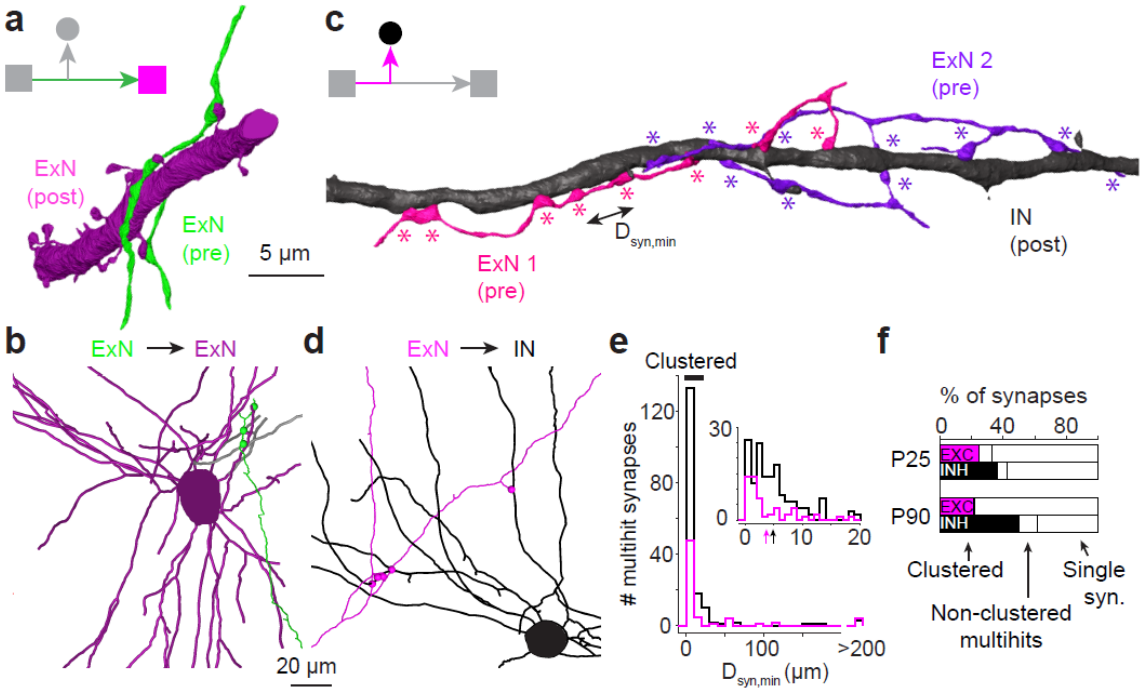

Figure 3.8: Dendritic synapse clustering in medial entorhinal cortex.
(**a,b**) Examples of connections between ExNs (green) to ExNs (violet) in which synapses are in close proximity (less than 10-20 µm distance between synapses of the same presynaptic axon) along the same postsynaptic dendrite (P25 dataset). (**c,d**) Examples of connections between ExNs (magenta, violet) and INs (black) in which synapses are in close proximity (less than 10-20 µm distance $D_{syn,min}$ between synapses of the same presynaptic axon) along the same postsynaptic dendrite (P90 dataset). Note that the example in (c) depicts the innervation of an IN dendrite by two ExN axons from two ExNs converging with n=10 (violet) and n=8 (magenta) clustered synapses. (**e**) Quantification of dendritic clustering in MEC: minimal inter-synaptic distances $D_{syn,min}$ along the postsynaptic dendrite (see indication in c) between synapses of the same presynaptic ExN axon for all connected cell pairs in P25 and P90 datasets that involved multiple synapses per cell pair (multi-hit). Synapses with $D_{syn,min}$ < 20 µm were considered clustered. Note that the large majority of such synapses has even less than 10 µm minimal inter-synaptic distance $D_{syn,min}$ (inset; arrows: mean, 3.7 µm (onto ExNs) and 4.8 µm (onto INs)). (**f**) Fraction of synapses involved in multi-hit connections and clustered connections. Note that at least 12% of all ExN-ExN connections and at least 24% of all ExN-IN connections involve dendritic synapse clustering. Scale bars: 5 µm (a,c); 20 µm (b,d). From (Schmidt et al., 2017).

3.2.6 Axonal properties of feed-forward interneurons

Having found cFFI with PLASS in the excitatory branch of the circuit (Fig. 3.6), we next investigated the inhibitory branch of this circuit. We first measured the path length distribution of output synapses along the interneurons' axons (Fig. 3.9a-c; Fig. 3.10a, n=3 INs P25), which showed no evidence for a positional bias of the cFFI synapses compared to all synapses (n = 884 IN synapses vs n = 131 cFFI synapses, 334 ± 55 vs 331 ± 47 µm, mean ± s.d., t-test, P>0.5, Fig. 3.9c). We however noticed that the IN axons are frequently myelinated before establishing the output synapses (Fig. 3.9a), with myelination of all axonal branches in a P90 IN (Fig. 3.9d,e). Furthermore, the diameter of the IN axons appeared very large compared to the axon diameter of the excitatory axons in the cFFI circuits (Fig. 3.9f). When quantifying cross-sectional diameters of inhibitory and excitatory axons (Fig. 3.9g,h), we find that in fact the inhibitory axons show a 2.5-fold wider diameter along their path from after the axon initial segment to the distance at which most output synapses are formed (n=15 (excitatory) vs n=18 (inhibitory path to synapse), 0.29 ± 0.11 vs 0.72 ± 0.11 µm, mean ± s.d., t-test, $P<10^{-11}$, Wilcoxon rank test, $P<10^{-5}$, Fig. 3.9h, see section 3.4 Methods and Fig. 3.10b). This was a truly remarkable finding, since we had expected IN axons if anything to be smaller than ExN axons. Accordingly, a recent study had found strong myelination of IN axons in supragranular layers of V1 (Micheva et al., 2016), but axon diameters of INs were not substantially larger than for ExN axons in that study. Together, the finding of up to 100% myelinization and 2.5-fold wider axonal diameters in the inhibitory branch of the cFFI circuit could provide accelerated AP transmission from the IN to its targets.

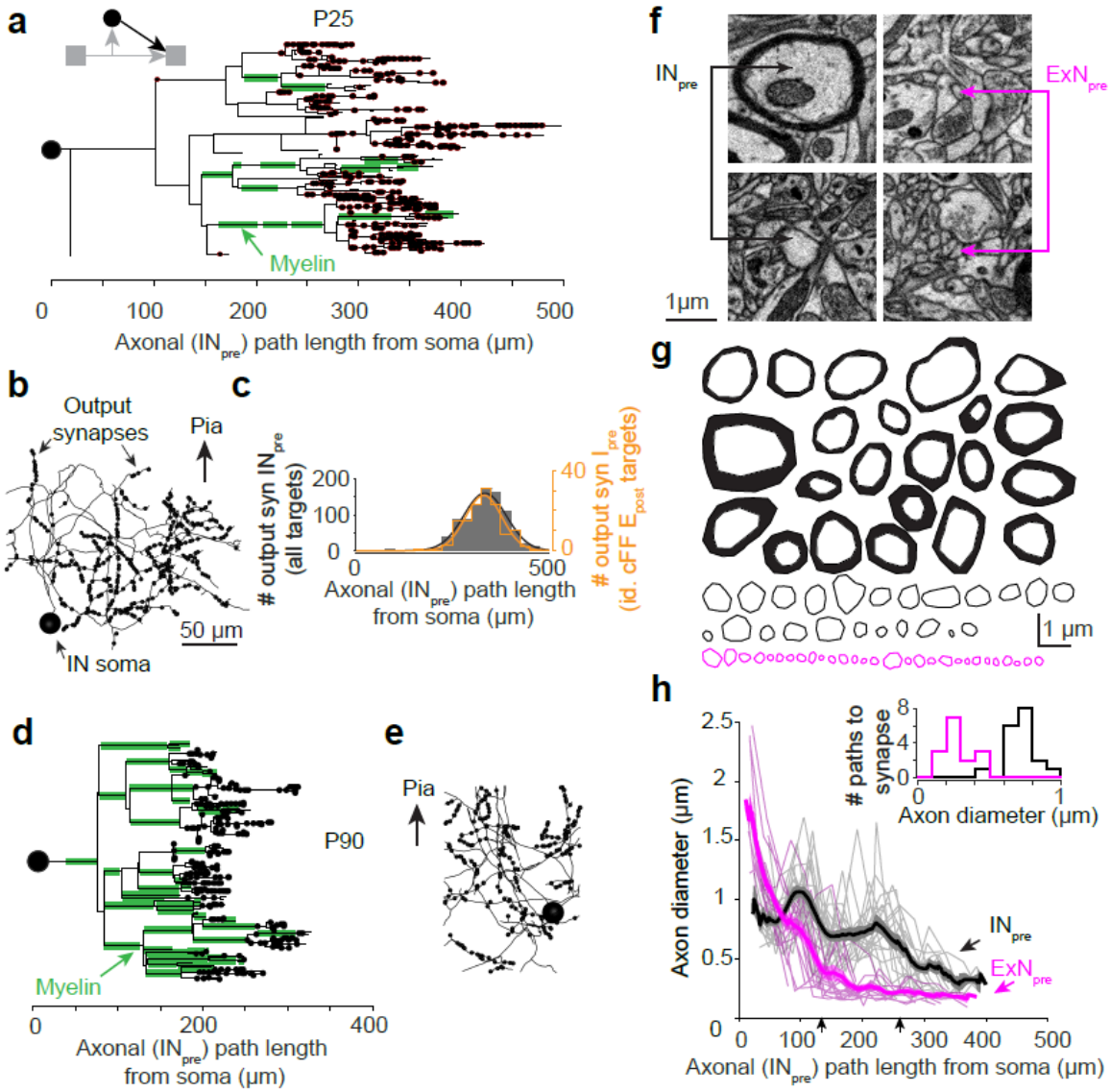

Figure 3.9: Axonal properties of interneurons involved in cellular feedforward inhibition (cFFI).

(**a**) Axonogram of one IN (P25) with n=401 output synapses. Note stretches of myelinization before output synapses are established (green). (**b**) 2-D projection of the same axon (4.5mm path length) with synapse positions. (**c**) Distribution of IN output synapses along axonal path length of 3 INs (Fig. 3.10a) for all their output synapses (n=884, black) and those synapses involved in the cFFI circuits (n=131, orange). (**d**) Axonogram of one IN (n=270 synapses, P90) showing complete myelinization before synapses are established. (**e**) 2-D projection of the same axon with synapse positions (3.7mm reconstructed axonal path length). (**f**) Example cross-sections of IN (left) and ExN axons (right) showing substantial diameter differences. (**g**) Overview of cross section contours of IN axons (black, top, n=45 sampled at 170 µm from the soma of 4 INs; thickening indicates myelinization) and 29 cross sections of ExN axons (magenta, bottom, n=29 sampled at 170 µm from the soma of 6 ExN). (**h**) Change of axon diameters (mean and s.e.m. at intervals of 25 µm) along the trajectory between soma and distal synapses for 3 INs (n=18 synapses, gray traces) and for 4 ExNs (n=16 synapses, magenta traces) (P25; P90 in Fig. 3.10b). Note the about 2.5-fold larger diameter of IN axons between about 130-260µm path length (black arrows). Inset: Distribution of the mean axon diameter, (over interval between black arrows) for 15 excitatory (magenta) and 18 inhibitory (black) axonal trajectories (0.29±0.11 µm vs 0.72±0.11 µm, mean±s.d., t-test, $P<10^{-11}$, Wilcoxon rank test, $P<10^{-5}$). Scale bars: 50 µm (b,e); 1µm (f,g). From (Schmidt et al., 2017).

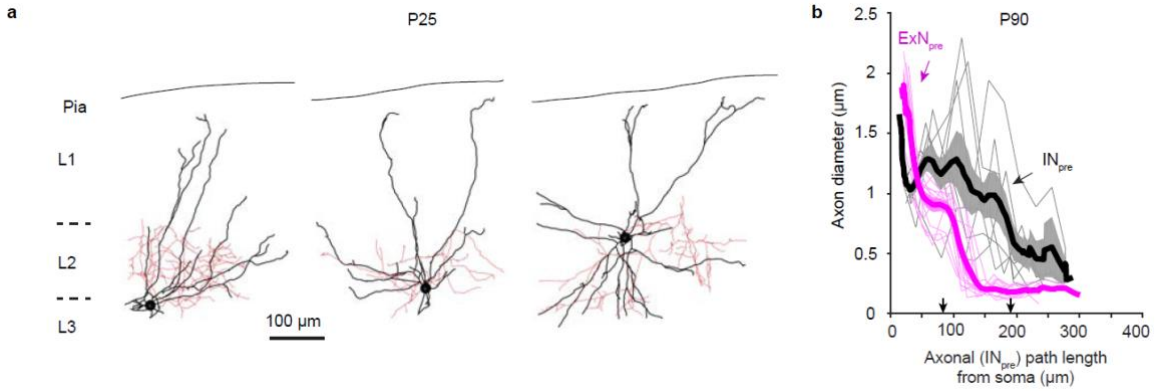

Figure 3.10: Morphology of interneurons involved in cellular feed-forward inhibition and change of axon diameters along the axon from soma to synapses for the P90 dataset.
(**a**) Morphologies of three INs involved in cFFI circuits. From left to right: 4.5, 2.3, and 3.6 mm reconstructed axonal path length, respectively. Scale bar 100µm. (**b**) Development of axon diameters along the trajectory between soma and distal synapses for one IN (n=7 synapses, gray traces) and for 3 ExNs (n=12 synapses, magenta traces) from P90 dataset. Mean and s.e.m. at intervals of 25 µm distance shown (based on linear interpolation between diameter measurement locations). Note the about 2.7-fold larger diameter of IN axons between about 83 and 188µm path length distance (indicated by black arrows, n=12 (excitatory) vs n=7 (inhibitory path to synapse), 0.4 ± 0.1µm vs 1.09 ± 0.46µm, mean ± s.d., t-test, $P<10^{-3}$, Wilcoxon rank sum, $P<10^{-4}$). From (Schmidt et al., 2017).

3.2.7 PLASS and cellular feed-forward inhibitory circuits

We finally studied the subcellular arrangement of the converging inhibitory and excitatory synapses on the postsynaptic excitatory neurons (Fig. 3.11a,b). In the cFFI circuits we find that the imbalance of inhibitory synapses converging onto the postsynaptic neuron over the number of converging excitatory synapses is on average $N_{syn}(IN) / N_{syn}(ExN) = 2.2 \pm 1.7$ (n=54 cFFI circuits, mean ± s.d., right tailed t-test against 1, $P<10^{-5}$, Fig. 3.11c). Furthermore, the position of these synapses on the postsynaptic dendrites is biased such that excitatory inputs in the cFFI circuits are more distal than inhibitory inputs (Fig. 3.11b,d; n=54 cFFI circuits, 75.3 ± 35.8 µm for ExN vs 45.4 ± 18.2 µm for IN synapses, mean ± s.d., paired t-test, $P<10^{-6}$, Fig. 3.11d), allowing for powerful inhibition of excitatory inputs in the cFFI configuration. Finally, we measured the PLASS distance for each of the cFFI circuits (Fig. 3.11e): synapses onto excitatory neurons were on average 117.4 ± 79.7 µm more distally positioned along the presynaptic axon than those onto interneurons (n=54 circuits, mean path length of synapses onto excitatory 269 ± 57.5 µm vs inhibitory 151.6 ± 59.2 µm targets, mean ± s.d., paired t-test, $P<10^{-17}$, Fig. 3.11e).

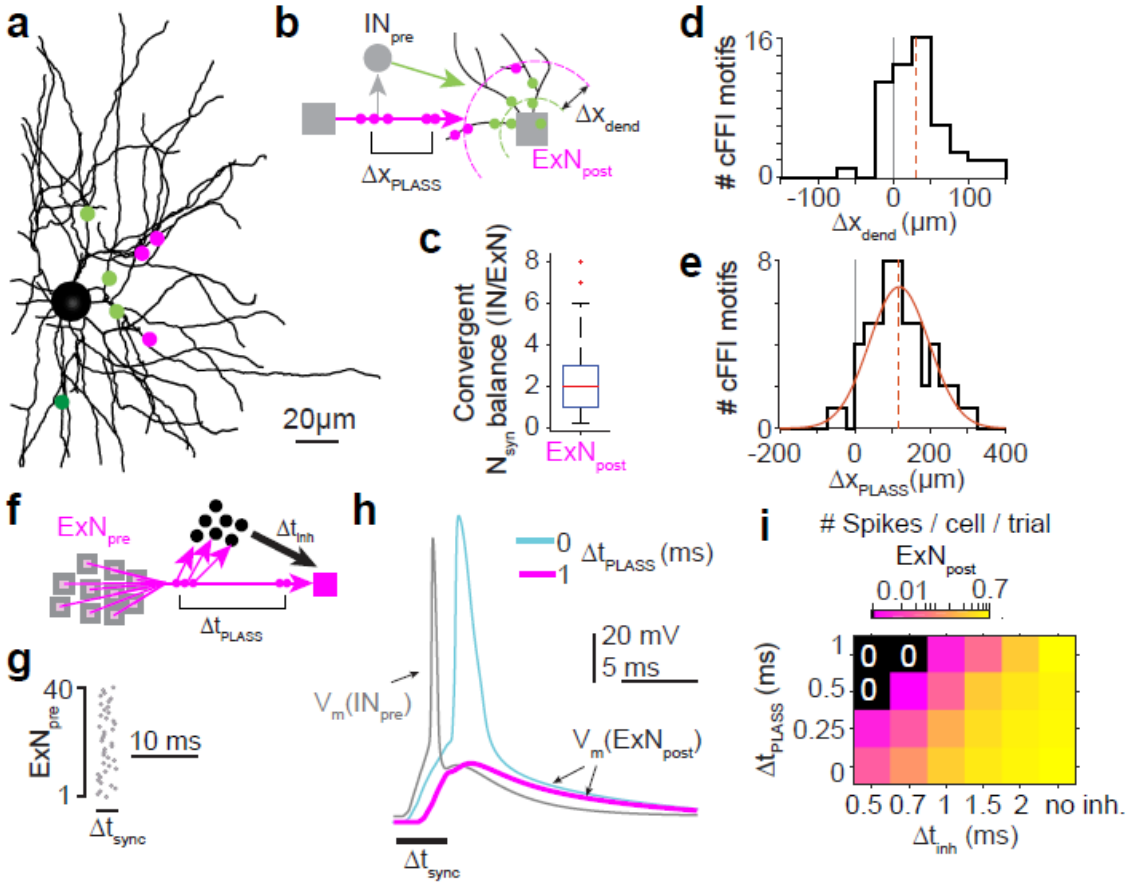

Figure 3.11: Convergence of the cellular feedforward inhibition (cFFI) circuit and effects of path-length dependent axonal synapse sorting (PLASS) on propagation of synchronous excitatory activity in medial entorhinal cortex.
(**a**) Example reconstruction of a postsynaptic ExN (black) with cFFI synapse positions on the postsynaptic dendrites (colored circles; from INs, green; from ExN, magenta). (**b**) Sketch of the relevant geometric dimensions: postsynaptic dendritic synapse distance between ExN and IN inputs Δx_{dend}; presynaptic axonal synapse offset due to PLASS (Δx_{PLASS}), see d,e. (**c**) Relative number of inhibitory vs excitatory synapses converging onto E_{post} in 54 cFFI circuits (on average 2.2±1.7-fold excess of IN synapses, mean±s.d.). (**d**) Average offset of ExN synapses (more distal) and IN synapses (more proximal) on postsynaptic dendrites (Δx_{dend} = 30±40µm, n=54 cFFI circuits, dashed line). (**e**) Average distance of synapses involved in cFFI along the presynaptic ExN axon (Δx_{PLASS}): Excitatory synapses onto ExNs are 117.4±79.7µm (dashed) more distal than the corresponding synapses onto INs (n=54 circuits). (**f**) Sketch of cFFI circuit indicating AP conduction delay based on PLASS (Δt_{PLASS}) and inhibitory delay combining AP conduction time and synaptic release (Δt_{inh}). (**g**) Example of simulated synchronous presynaptic population activity (1 AP per neuron within Δt_{sync}=3ms) in PLASS-cFFI circuit (f). (**h**) Example of simulated membrane potential transients following a synchronous presynaptic activiation (g) in the IN (gray) and the postsynaptic ExN with (magenta) and without (cyan) PLASS-based presynaptic delay Δt_{PLASS}. Note that for such synchronous presynaptic activity, the cFFI circuit alone cannot suppress the postsynaptic ExN to discharge an AP, but cFFI with a PLASS-based delay of Δt_{PLASS}=1ms can. (**i**) Quantification of postsynaptic AP suppression upon brief synchronized presynaptic population activity in dependence of PLASS-based delay (Δt_{PLASS}) and delay of inhibitory axon conduction and release (Δt_{inh}). Note that for a regime of Δt_{inh}=0.5…0.7ms and Δt_{PLASS}=0.5…1ms, faithful suppression of postsynaptic AP discharge is possible. See Fig. 3.12. Scale bar: 20µm (a). From (Schmidt et al., 2017).

We finally explored possible functional implications of the precise subcellular arrangement of synapses in this cFFI circuit. We had found five main features of the circuit: (1) PLASS in the excitatory axon (Fig. 3.4, Fig. 3.11e, synapse offset of about 120 µm); (2) Small-diameter ExN axons (Fig. 3.9f-h); (3) dendritic synapse clustering, especially onto IN dendrites (Fig. 3.8); (4) Highly myelinated large-diameter IN axons (Fig. 3.9f-h); (5) About 2-fold excess of IN synapses, positioned closer to the soma than ExN synapses on the cFFI target neurons (Fig. 3.11a-d). While each of these findings alone would make an interpretation in terms of the timing of AP propagation unlikely because the involved temporal delays seemed too small, when acting in concert, these mechanisms could possibly allow for precisely timed inhibitory control of postsynaptic APs. To study this quantitatively, we performed numerical simulations of the cFFI circuit (as in Fig. 3.6), this time implementing the additional subcellular findings (1)-(4) as listed above. In particular, we varied the temporal delays possibly contributed by PLASS (findings (1) and (2), summarized as Δt_{PLASS}) and the conduction and synaptic transmission delays contributed by the inhibitory axon (finding (4), Δt_{inh}, Fig. 3.11f).

We speculated that precise millisecond timing might be critical in cases when the presynaptic population is active in tight synchrony. To emulate this, we activated the presynaptic excitatory neurons to discharge one AP within 3 or 10 ms (Fig. 3.11g, Fig. 3.12a) and investigated the postsynaptically converging PSPs (Fig. 3.11h). Without PLASS ($\Delta t_{PLASS}=0$) the synchronous activity could not be completely blocked from propagation, and APs still occurred postsynaptically (Fig. 3.11h). When adding PLASS yielding a delay of $\Delta t_{PLASS}=1$ ms (corresponding to a conduction velocity of 120 µm/ms in the ExN axon given the measured PLASS offset Δx_{PLASS}, Fig. 3.11e), however, the inhibitory cFFI input arrived in time to completely suppress the postsynaptic AP (Fig. 3.11h, shown for inhibitory delay of $\Delta t_{inh} = 0.7$ ms). When screened over varying PLASS delays Δt_{PLASS} and inhibitory conduction delays Δt_{inh}, we find that PLASS in fact allows full suppression of action potentials after highly synchronous presynaptic acitivtiy for $\Delta t_{PLASS} \geq 0.5$ ms (at $\Delta t_{inh} = 0.5$ ms inhibitory delay) and $\Delta t_{PLASS} = 1$ ms at $\Delta t_{inh} = 0.7$ ms inhibitory delay. Also for $\Delta t_{inh} = 0.7$ ms and $\Delta t_{PLASS} = 0.5$ ms, postsynaptic activity is reduced about 200-fold (from 0.58 to 0.0025 spikes per cell per trial, Fig. 3.11i). In previous studies in rat cortex, the latency between AP peak in local cortical interneurons and the onset of the IPSP in postsynaptic excitatory cells has been found to be between 0.5 and 1.1 ms (Hoffmann et al., 2015; Koelbl et al., 2015). Given the strong myelination and wide diameter of the IN axons we found in

MEC, it is thus plausible that Δt_{inh} is in a regime (Fig. 3.11i) in which the PLASS-cFFI circuit can faithfully block the propagation of highly synchronous excitatory activity. This was the case for synchronous bursts of 3 and 10 ms length (Fig. 3.11i, Fig. 3.12a; note that in none of 4000 sampled presynaptic AP patterns a postsynaptic spike could be elicited; this is in contrast to the effects on spike timing in the pFFI/cFFI comparison, which are only obvious in the average AP activity, Fig. 3.6). Furthermore, the synchrony block was stable to additional background activity (Fig. 3.12b,c), and activity propagation could be unblocked by an additional postsynaptic gating input, Fig. 3.12d-h.

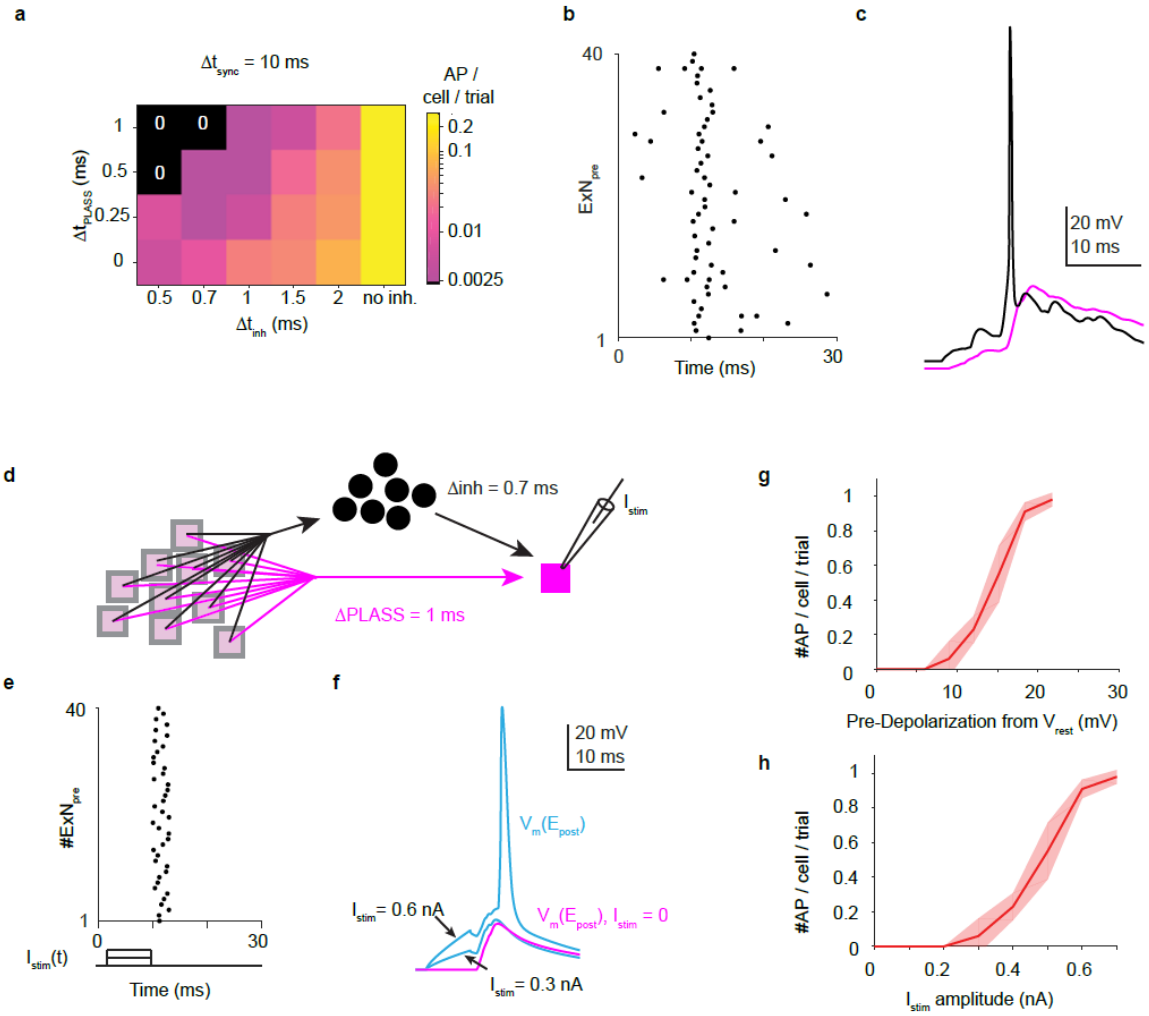

Figure 3.12: Numerical simulations of the PLASS-cFFI circuit motif.
(**a**) Effect of PLASS on suppression of synchronized activity, for synchronization interval Δt_{sync} of 10 ms (cf. Fig. 3.11g,i). (**b,c**) Effect of additional background activity on PLASS-based suppression of synchronized activity propagation. Example shows 20 Hz background activity, under which PLASS-based suppression is still effective for synchronization intervals 3 and 10 ms. (**d-h**) Effect of an additional postsynaptic pre-depolarization on recovery from PLASS-supression. (**d**) Emulated current injection in postsynaptic neuron for PLASS circuit at 0.7 ms inhibitory delay and 1 ms PLASS delay. (**e**) Presynaptic synchronized activity and 8 ms-long rectangular pre-depolarizations in the postsynaptic neuron. (**f**) Simulated membrane potential transients in the postsynaptic excitatory neuron. Note spike suppression by PLASS (magenta, no additional stimulation), that can be gradually recovered from by current injections of increasing amplitude I_{stim}. (**g,h**) Titration of PLASS recovery over stimulus strength and effective pre-depolarization before the synchronized input activity. A pre-depolarization of 10-20 mV is sufficient for recovery from PLASS; this could be achieved by underlying membrane potential modulation or an additional gating input to the postsynaptic excitatory neuron, for example at its apical dendrites in layer 1. From (Schmidt et al., 2017).

3.3 Discussion

We discovered path length-dependent sorting (PLASS) of output synapses along the axons of excitatory neurons in rat medial entorhinal cortex, a novel level of specificity in neuronal circuits of the mammalian cerebral cortex. We found that PLASS acts in a cellular feed-forward inhibition circuit, in which synapses are frequently clustered, in particular on the postsynaptic interneuron dendrites. The inhibitory branch of the circuit appears to be shaped for fast action potential transmission using myelinated, large-diameter axons. Together, this high-precision circuit in MEC may be in place to sharpen AP timing, and to control the propagation of highly synchronous activity in a cortex occupied with spatial sequence analysis.

Our data is the first to demonstrate the positional sorting of output synapses in the mammalian cortex. However, in hindsight, data from mouse V1 cortex (Bock et al., 2011) and from CA1 (Takacs et al., 2012) can be interpreted as an indication that PLASS may operate in various cortices. In these studies, it had been noted that the fraction of synapses targeting interneurons was higher than expected on average. Since the studies were limited in EM-reconstructed volume (with an extent of 45µm in the third dimension in V1), the reconstructed axons were necessarily only very proximal. The fact that our volume was at least 3-fold larger in the third dimension made it possible to detect PLASS as a transition from IN-dominated to ExN-dominated targeting within the same excitatory axons, and determine the properties of the local cFFI circuit. Future studies are required to investigate whether PLASS is a general principle of cortical wiring in mammals.

Data on axonal conduction velocity (Helmstaedter et al., 2008d; Kress et al., 2008; Schmidt-Hieber et al., 2008) and latencies of local inhibition in cortex (Hoffmann et al., 2015; Koelbl et al., 2015) make it plausible that the described circuit can prevent the propagation of highly synchronous activity in L2 of rat MEC as shown in Fig. 3.11f-i (for this, AP propagation along the axon would have to be between 120-240 µm/ms and local inhibitory AP-to-IPSP latencies 0.5-1 ms). This is especially noteworthy since so far, feedforward inhibition circuits have rather been interpreted to selectively propagate synchronous, but not asynchronous activity (e.g. (Bruno, 2011)). The PLASS-cFFI circuit, in contrast, can act as a synchrony block. At the same time, if the postsynaptic neuron was to receive additional excitatory input or be modulated by an additional underlying membrane potential modulation such as the theta-frequency oscillation found in MEC (Alonso and Klink, 1993;

Alonso and Llinas, 1989), the PLASS-cFFI circuit could allow a controlled, predictive gating of synchronous activity propagation (Fig. 3.12d-h). The same would be possible by disinhibition of the involved interneurons.

Our data show a novel high-precision wiring motif in cortex, revealing an unexpected level of structural specialization in local cortical circuits. We explored possible functional implications of these structural findings, pointing towards an effect on spike timing precision and the control of synchronized activity propagation. Connectomic analysis of other cortices will allow us to determine if path length-dependent axonal synapse sorting constitutes a general cortical wiring principle in mammals.

3.4 Methods

3.4.1 Animal experiments

All experimental procedures were performed according to the law of animal experimentation issued by the German Federal Government under the supervision of local ethics committees and according to the guidelines of the Max-Planck Society.

3.4.2 Brain tissue preparation

A male P25 Chbb:THOM (Wistar) rat (45 g) was anesthetized with Isoflurane. It was then perfused transcardially with ~25ml 0.15 M Cacodylate buffer, followed by ~160 ml of fixation solution (2.5% PFA, 1.25% Glutaraldehyde, 2 mM CaCl in 0.08 M Cacodylate buffer) at 15 ml/min. After perfusion, the brain was removed from the skull and left in the fixation solution for 24h at 4°C. Then, three consecutive parasagittal brain slices (thickness: 70 µm, 550 µm, 70 µm, respectively) containing the medial entorhinal cortex were cut from the right brain hemisphere using a vibratome (Microm HM650 V, Thermo Scientific). Next, vertical vibratome cuts were performed on the 550 µm slice to extract a ~500 µm (dorso-ventral) times ~700 µm (anterio-posterior) tissue sample containing the upper layers of the medial entorhinal cortex. This sample was further processed for en bloc EM staining.

After extraction of the EM sample, the 550 µm – thick slice was transferred into a 10% sucrose solution in PB overnight followed by an incubation in 30% sucrose solution for 24h for cryoprotection. After that, the brain slice was embedded in Jung Tissue Freezing Medium (Leica Microsystems Nussloch, Germany) and cut into 60 µm thick sagittal slices with a freezing microtome (Leica 2035 Biocut). These, as well as the 70 µm – thick brain slices obtained in the previous step, were subsequently processed for Calbindin immunoreactivity for confirmation of sample location within MEC (Fig. 3.2b).

To obtain the P90 sample the same procedure was applied. In brief, a 90 days old Wistar rat (235 g) was anesthetized with Isoflurane, then perfused transcardially with ~75ml 0.15 M Cacodylate buffer, followed by ~250 ml of fixation solution at 15 ml/min. The ~600 x 700 µm sample was extracted from a 500 µm thick parasaggital brain slice containing the upper layers of the MEC and processed for EM (see below). After sample extraction, the slice was processed for Calbindin immunoreactivity for confirmation of sample location within the MEC (Fig. 3.2c). The staining for Calbindin immunoreactivity was performed as described in section Histochemistry and Immunohistochemistry 2.4.2.

3.4.3 Sample preparation for electron microscopy

En-bloc staining for EM was performed as in Hua et al 2015. Briefly, the tissue was stained with a reduced osmium tetroxide solution (2% OsO_4 in 0.15 M cacodylate buffer) followed by incubation with ferrocyanide (2.5% KFeCN in 0.15 M cacodylate buffer) and an incubation in saturated aqueous thiocarbohydrazide solution. Then, the sample was first transferred into 2% OsO_4 (in H_2O) for amplification and then left over night at 4°C in a solution containing 2% uranyl acetate (in H_2O). Then, the tissue was incubated in 0.02 M lead (II) nitrate. Dehydration and resin embedding was performed as in (Briggman et al., 2011). Briefly, the sample was dehydrated with propylene oxide and ethanol, infiltrated with 50%/50% propylene oxide/Epon and embedded in Epon (using the Epon substitute embedding medium kit, Sigma Aldrich) at 60°C for 24h. For the P90 sample, embedding was as in (Hua et al., 2015).

3.4.4 Continuous imaging

The P25 sample was imaged using a Magellan scanning electron microscope (FEI Company, Hillsboro, OR) equipped with a custom-built SBEM microtome (courtesy of W. Denk). To allow continuous image acquisition, piezo actors (P-602 Physik Instrumente, Karlsruhe, Germany) were added to the microtome setup to operate in line with geared motors (M-230, Physik Instrumente; Fig. 3.2d) for movements in the plane of imaging (x and y directions).

The plane of imaging was divided into 4 overlapping regions (motortiles, MTs) sized 217 µm in x and 216 µm in y, each (note that the radial cortex axis corresponded to the horizontal (x) axis during image acquisition). The stage movement between the MTs was executed using the geared motors (Fig. 3.2e). Within each MT, stage movement was executed using the piezo actors and configured as follows: The vertical stage movement (y Axis, Fig. 3.2e) consisted of a brief acceleration to 34.2 µm/s followed by a plateau continuous movement for 7.5 s, followed by a linear deceleration to –34.2 µm/s (see the piezo control voltage transients during one MT, Fig. 3.2h). This corresponded to continuous alternating down- and up-wards movements ("piezo columns"), interleaved by direction inversion strokes. The horizontal stage movement (x Axis, Fig. 3.2e) was executed during the direction inversion strokes (Fig. 3.2f), yielding step-wise right-ward movements in x after each piezo column that shifted the piezo columns by 31.4 µm. After each piezo column, the image orientation was rotated by 90° using the image rotate option in the FEI control software.

After acquisition of the first MT, the stage was moved rightwards by 217 µm, and then the 2nd MT was executed, this time starting from the bottom right of the MT area (Fig. 3.2f) such that the positions of the piezo actor did not have to be changed between the end of MT1 and the beginning of MT2. Then, MT3 and MT4 were executed analogously (Fig. 3.2e).

Image acquisition was configured as follows: during the piezo column movements, 10 images sized 2048 x 3072 voxel each were acquired continuously (without delay between image acquisitions) using a custom-written C# library (K Boergens, B Lich and P Potocek). Image acquisition was started 0.59 s after initiation of the piezo column movement. To compensate for the line feed introduced by the y piezo movement, the EM scanning line feed was reduced to 7.1% by activation of the "tilt" mode (set to 85.9°). The reset movement of the EM beam after image acquisition thus amounted to a beam position jump antiparallel to the current y piezo movement, creating overlap between consecutive images in the y axis that could be later used for image alignment (see below). After image acquisition during one piezo column movement, image acquisition was paused for 1.08 s to allow the x piezo movement to be executed. The resulting image columns had a variable offset along the y axis (Fig. 3.2e), which was compensated by an overlap between the motortiles of about 8 µm, such that complete coverage of the blockface was assured.

7 consecutive piezo columns were spaced in x such that neighboring columns overlapped by about 9% in the horizontal direction. MT were set to overlap by about 5.5 µm in x. Dwell time was set to 100 ns, and the effective data acquisition speed including all movement overheads was 5.9 MVx/s.

3.4.5 Conventional mosaic imaging

The P90 sample was imaged using a Quanta scanning electron microscope (FEI, Quanta 250 FEG) equipped with a custom built SBEM microtome (courtesy of W. Denk). Image acquisition was performed in the conventional mosaic-based mode. The plane of imaging was devided into 4 x 2 overlapping regions, each sized 46 x 69 µm^2. The stage movement between these mosaics was performed using geared motors (M-227.25, Physik Instrumente). Overlap between mosaic positions was set to 1.1-2 µm. Dwell time was set to 2.3 µs, and the effective data acquisition speed including movement overheads was 0.4 MVx/s.

3.4.6 Dataset acquisition

For the P25 dataset, the sample position was centered to L2 judged by distance to pia in low-resolution overview images, acquisition in continuous mode (see above) was started. 8372 consecutive image planes were acquired, interleaved by microtome cuts set to 30 nm cutting thickness. For the final 56 µm of the dataset, cutting thickness was set to 50 nm, thus the total extent of the dataset in the cutting direction was approximately 274 µm (see next section). The incident electron energy was set to 2.5 keV for the first 561 slices, then increased to 2.8 keV. The beam current settings were chosen to yield 3.2 nA nominal beam current (resulting in a dose of ~16 electrons/nm^2). Focus and astigmatism were constantly monitored and adjusted using custom-written autofocus routines. Focus was frequently unstable, likely due to cutting debris accumulating around the sample and in the vacuum chamber. This was compensated by frequent manual skeleton reconstruction in about 3h intervals during the course of the experiment to monitor axon traceability. The position of the field of view was shifted 4 times during the course of the experiment to compensate for a tilt of the sample in the tangential plane (shifts along the radial cortex axis towards white matter by 17.5 µm from plane 1816 onwards, by 21.6 µm from plane 3146, by 43.1 µm from plane 4336 and by 24.8 µm from plane 6375).

The field of view of the P90 sample was centered to L2 of the MEC, containing parts of L3. In low-resolution overview images, the beginning of L2 is clearly distinct from the almost cell free L1. 5545 consecutive image planes were acquired, interleaved by microtome cuts set to 30 nm cutting thickness. For the final 262 slices of the dataset, the field of view was shifted by ~112 µm toward the pia to compensate for a slight tilt of the sample in the tangential plane. The incident electron energy was set to 2.8 keV. The beam current settings were chosen to yield 0.16 nA nominal beam current (resulting in a nominal dose of ~ 22.27 electrons/nm^2). Focus and astigmatism were constantly monitored and adjusted 2-4 times / day.

3.4.7 Image Alignment

First, all images obtained from one image plane and motortile (i.e., 10 x 7 = 70 images sized 2048 x 3072 voxels each) were aligned separately using Speeded Up Robust Features (SURF) detected on the overlap regions of neighbouring image pairs (P25). For the P90 dataset, in – plane alignment was performed with FIJI/ImageJ using the 'Grid/Collection stitching' plugin (Preibisch et al., 2009).

To match aligned images from consecutive planes, a region sized 70% of the horizontal MT size and 50% of the vertical MT size, located at the MT center, was cross-correlated with the same region from the next image plane. The translation vector between the cross-correlation peaks was applied to the second image, respectively. In 565 slices (P25), debris from previous cuts was present on the block surface. These slices were excluded from alignment, yielding a total of 7807 slices that were used for reconstruction. For the P90 dataset, the first 3399 slices were used for reconstruction (24 slices excluded because of debris, yielding a total of 3375 slices).

After alignment, the four resulting 3D image stacks for each of the four motortiles (referred to as MT1 to MT4 in the following) of the P25 dataset, as well as the aligned image stack for the P90 dataset, were each converted to the KNOSSOS data format (Helmstaedter et al., 2011; www.knossostool.org) by splitting into data cubes sized 128 x 128 x 128 voxels each. This data was then uploaded to the online data annotation software webKnossos (Boergens et al., 2017) for in-browser distributed data visualization, neurite skeletonization and synapse identification.

3.4.8 Reconstruction of axons and dendrites

First, we identified 665 neuronal cell bodies in all four MTs of the P25 dataset and reconstructed all dendrites with the help of 24 undergraduate students using webKnossos. Annotators were instructed to reconstruct all dendrites starting from the soma without spines, be especially cautious as not to miss branches and place comments whenever the dendrite reached a MT border for subsequent matching of neurites across MTs. All students were trained on at least 3 neurons including 1-2 cells from this MEC dataset (total training time about 10 hours per student). Only after successfully finishing training the annotators were allowed to continue with new tasks. The same procedure applied to the reconstruction of the 91 identified neuronal cells in the P90 dataset.

All axons in the P25 dataset were reconstructed by one expert annotator; one axon was independently reconstructed by two additional expert annotators, whose results agreed with the original annotation. Axons were terminated either at the border of the dataset, by an axonal termination (found always in an end bouton synapse) or could not be followed further due to focus issues.

All axons in the P90 dataset were reconstructed independently by two expert annotators and 10 undergraduate students. The two expert tracers then formed a consensus reconstruction based on these 12 annotations per axon.

To match dendrites and axons across motortiles of the P25 dataset the following procedure was applied. First, the dendrite or axon was identified in the overlap region of the adjacent motortile. Prominent processes like myelinated fibers, somata and large-diameter dendrites in the same cutting plane were used as landmarks to constrain the search region. The first node of the continuing process was then placed at the same position within the neurite. The difference between the coordinates of these two matching points was then used to transform the skeletons into one coordinate system for further analysis. This procedure was repeated whenever the tracing reached an MT border. All axons and all dendrites of the 15 neurons and 3 inhibitory cells (shown in Fig. 3.3a, Fig. 3.4, Fig. 3.9, and Fig. 3.10a) were reconstructed completely across all motortiles.

3.4.9 Synapse identification and target classification

Synapses were identified by following the trajectory of axons in webKnossos (Boergens et al., 2017). First, vesicle clouds in the axon were identified as accumulations of more than about 10 vesicles. Then, the most likely postsynaptic target was identified by the following criteria: direct apposition with vesicle cloud; presence of a darkening and broadening of the synaptic membrane, indicative of a postsynaptic density (PSD); vesicles very close to membrane at site of contact (see Fig. 3.1 for examples). Synapses were classified as uncertain whenever the signs of a broadened and darkened stain at the synaptic membrane (resembling a PSD) could not be clearly identified. All analyses in this study were conducted on synapses classified as certain, only. To measure inter-expert variability in synapse annotation, 3 additional experts annotated all synapses and their targets for 1 of the ExN axons (Fig. 3.4, 7th row). For each of the 4 expert annotations, independently, PLASS was found (the path length distribution of synapses onto spines and synapses onto shafts was significantly different, $p<0.02$, 0.01, 0.04, 0.03, respectively). 39/44 synapses were identified as certain by all 4 annotators, 3 additional synapses by 3 of 4 annotators, and 2 by 2 of 4 annotators. In the P90 dataset, two additional experts independently annotated 30 randomly selected synapses (agreement with the initial expert annotator: 28/30 and 30/30 for the two experts, respectively).

The postsynaptic targets of axonal synapses (n=310, P25; n = 284, P90) were classified as ExN, IN, or glia (for each apparent postsynaptic spine head, the corresponding dendritic trunk was searched to distinguish from glial targets). For this, the target dendrites were identified by the corresponding soma, which had been reconstructed before and classified as ExN or IN. For the classification as ExN or IN, dendrite morphology and the origin of the axon was evaluated. ExN axons exited the soma towards the white matter, while IN axons frequently originated from dendrites. For the remaining targets, the postsynaptic dendrites were classified as smooth *vs*. spiny by reconstructing them at least in one MT/ whole volume (P90) and measuring the rate of spines on two 10 µm – long dendritic segments. Dendrites were either clearly spiny or carrying few spines and filopodial protrusions without a clear spine head, or lacking spines entirely. We used dendrites of clearly identified INs and ExNs to calibrate spine density, yielding a definition of spiny dendrites with a spine density of ≥0.6 per µm, and smooth dendrites with a spine density of ≤0.2 per µm.

3.4.10 Dense dendritic reconstruction, dendrite density measurement, classification of smooth and spiny dendrites

For the measurement of IN dendrite density in the P25 dataset, 7 regions sized $(10\ \mu m)^3$ each were selected along the radial cortex axis within L2 (Fig. 3.4h, Fig. 3.5b,c). Regions were chosen to avoid cell bodies or blood vessels. Within these regions, all dendritic shafts were densely skeleton-reconstructed. Then, each dendrite was classified as smooth or spiny based on the above criteria. When a dendrite did not show spines locally, it was followed for at least 10 µm. If none or 1-2 spines were found, the dendrite was continued for at least 30-40 µm to assure the lack of spiny regions. Only then the dendrite was classified as smooth / IN. Dendrite path length was measured from the reconstructed shaft skeletons (thus excluding spine path length).

3.4.11 Pyramidal and stellate cell classification

Two previously reported (Fuchs et al., 2016) parameters for classification of pyramidal vs. stellate cells in MEC L2 were investigated: the number of primary dendrites and the size of the cell body. First, two experts were asked to assign the morphology of dendritic reconstructions as clear pyramidal, clear stellate, or unsure. For 29 of 67 reconstructions, both experts agreed in the assignment to the high-confidence categories. For these neurons, soma volume (Fig. 3.1i,j) was measured by placing 2 nodes in each of the three orthogonal

viewports in webKnossos to mark the extent in the three main axes, of which the geometric mean was used for volume approximation. Also, the number of primary dendrites was counted for a subset of 15 neurons (6 clear pyramidal cells, 4 clear stellates, 5 intermediate cells, Fig. 3.4b), but not found to be distinctive. The more distinct distributions of soma size (Fig. 3.1i) were each fitted by a Gaussian, and the simple probability of a neuron belonging to the clear stellate cell class $p_{Stellate}$ calculated by dividing the Gaussian fit to the stellate cells by the sum of both fits.

3.4.12 Local circuit analysis

Local circuit analysis was based on the connectivity data reporting the number of synapses between pairs of neurons or neurites in the P25 dataset. The synaptic connectivity between the four largest ExN axons, three fully reconstructed INs and 58 ExN targets that had their soma in the dataset was analyzed. Briefly, the connectivity matrix between these neurons was binarized to represent the presence or absence of synaptic connectivity. Then, indirect triadic connections ExN->IN->ExN were identified by squaring the connectivity matrix with all ExN->ExN connections set to zero. Then all full cFFI triads were identified by element-wise multiplication of the squared connectivity matrix with the ExN->ExN connectivity matrix. The resulting number of cFFI configurations (n=31) was then divided by the total number of ExN->ExN connections (n=41), yielding 76% cFFI ratio.

3.4.13 Axon diameter measurements

Contours of axonal cross sections (Fig. 3.9g) were reconstructed from all axonal branches at a distance of 170 µm from soma of 6 ExN axons (4 from P25, 2 from P90) and 4 IN axons (3 from P25, 1 from P90, 74 contours total) using webKnossos. Contours were traced in the orthogonal viewport most perpendicular to the local axon axis.

The diameter of axons was measured for the four excitatory axons with most path length and three interneuron axons in the P25 dataset; and for 3 excitatory neurons, 1 IN axon in the P90 dataset. To obtain the analyses shown in Fig. 3.9h, for the ExN axons, 4 synapses onto ExN targets were chosen, each (16 synapses in P25, 12 synapses in P90); of the four synapses chosen per axon, three were randomly drawn, and one was at a close-to-maximum path length distance from the soma. Then, for each synapse, skeleton nodes spaced 25 µm apart were selected along the path from that neuron's soma to the respective synapse and the diameter of the axon was measured at these locations in webKnossos. In case of myelinated segments the inner unmyelinated axon diameter was measured. In case of

branchpoints the diameter was measured slightly before the branchpoint. This procedure was similar for 6 synapses from each of the 3 inhibitory axons in P25 and 7 synapses from one inhibitory axon in P90. All measurements are shown in Fig. 3.9h (P25) and Fig. 3.10b (P90). For reporting mean and s.e.m., diameter measurements were linearly interpolated, and mean and s.e.m. were calculated for 0 to 400 µm distance from cell body in 25 µm intervals (Fig. 3.9h). For comparison of axon diameters between excitatory and inhibitory axons, the average diameters were computed between the point where the IN axons started their main branches, and the point where most synapses were made (defined as the range between the position of the 4th axonal branchpoint and the point at which 10% of the cumulative output synapses (from all IN) were reached; these ranges were 134 µm to 261 µm, P25; and 83 µm to 188 µm, P90).

3.4.14 Estimates of local circuit convergence and divergence

Bounds on local circuit convergence and divergence (used for circuit modeling, Fig. 3.6 and Fig. 3.11) were estimated as follows: for divergence of excitatory projections onto local interneurons, we used as a lower bound the number of unique INs (with identified soma in the dataset) that were targeted by the largest 6 presynaptic axons in P25 (each more than 600 µm in length), which was 5 per axon. Then we asked how many synapses were likely made between a given connected pair of excitatory and inhibitory neuron. This number was 2.6 in P25 for identified ExN-to-IN connections; but about 4 at P90 (assuming that single-hit connections were due to artificially pruned axons, since none such connections are reported in the literature). We then scaled the total number of synapses made onto INs per ExN axon to an expected local ExN axon path length of about 2 mm (based on the likely local truncations and inspection of single-cell fills in (Burgalossi et al., 2011)), and divided this by the number of synapses per connection (about 40-50 synapses onto INs divided by 4 yields a divergence of about 10-12 INs). We then screened the circuit models for an ExN-to-IN divergence of 5-10 INs. We did not use higher IN numbers, since at the same time the effective conductance in the IN-to-ExN connection was screened between 950-1950 pS per contact (see below), yielding an additional regime of factor 2. For the estimate of ExN-to-ExN convergence, we did not use the measured synapse numbers, because we had found that ExN outputs are positioned more distally in the presynaptic axons (Fig. 3.4), making it likely that most ExN-to-ExN connectivity is established beyond the local reconstructions. We rather used the reported connectivity in (Fuchs et al., 2016), which ranged from about 5-10% local ExN-to-ExN connectivity. Given about 600 local ExNs (about 90% of about

660, Fig. 3.1), this yields 30-60 ExN to converge onto a postsynaptic ExN. We used 60 and 40 in the two main simulations (Fig. 3.4 and 3.11), and screened stability over ExN populations from 20-80 (Fig. 3.7b,c).

3.4.15 Numerical simulations

As stated in the contributions, the numerical simulations used for a quantitative interpretation of the anatomical findings were not carried out by the author of this thesis. Please see (Schmidt et al., 2017) for methodological details.

3.4.16 Statistical tests

All statistical tests were performed using MATLAB and Statistics Toolbox Release 2014b, 2015b, or 2016a (The MathWorks, Inc., Natick, Massachusetts, US). The distributions of soma volume for pyramidal vs stellate cells (Fig. 3.1i) were compared using a two-sided t-test for unpaired samples (function ttest2) and, because of small sample sizes (n=15,14), using a Wilcoxon ranksum test (function ranksum). The distributions of output synapse locations for inhibitory vs excitatory targets (Fig. 3.4c,f; see also Fig. 3.5a) were compared using a two-sided t-test for unpaired samples (n=136 and 140, Fig. 3.4c; n=90 and 189, Fig. 3.4f); a Wilcoxon ranksum test (function ranksum) as well as a randomization test for 1,000 random draws (random shufflings of the target assignment for all measured synapse positions; none of 1000 draws yielded a class separation equal to or larger than the observed separation between synapses onto IN and ExN targets, Fig. 3.4c,f). Gaussian curves were fit to the initial peak of each distribution by constraining the fit range to 0-300 µm (output to INs) and 0-400 µm (output to ExNs) in Fig. 3.4c, and to 0-250 µm (output to INs) and 0-400 µm (output to ExNs) in Fig. 3.4f. The test of the Euclidean distances of the excitatory vs inhibitory synapses to the soma (Fig. 3.4g) was performed as a two-sided t-test for unpaired samples (n=136 and 140) as well as a Wilcoxon ranksum test. IN dendrite fraction over cortical depth (Fig. 3.4h; see also Fig. 3.5b) was fitted by a line fit (n=7 datapoints, fit in MATLAB) yielding a linear approximation of slope -0.08/100 µm and y-axis intersection at 0.36.

For the statistical comparison of cFFI vs opponent inhibition (Fig. 3.6a-c), the following model was used. Given a triad of connections ExN_i-to-ExN_j and ExN_i-to-IN (of which we had 114 in the data), only two cases can follow: either the connection IN-to-ExN_j also exists (corresponding to cFFI, 54 cases in the data), or not (corresponding to opponent inhibition, 60 cases in the data). Assume an underlying biological probability p_b that IN-to-ExN_j exists

(p_b=0 would correspond to strict opponent inhibition; p_b=1 to strict cFFI; p_b=0.25 could be interpreted as opponent inhibition with a biological wiring noise of 25%, a level of wiring noise e.g. seen in (Helmstaedter et al., 2013)). Furthermore, the truncation of IN axons yields a connection detection probability p_{det} (this we estimated to be about 70% based on the completeness of the axonal trees of the INs, Fig. 3.10a). Together, the model implies a probability $p_{meas}= p_b*p_{det}$ of finding the connection IN-to-ExN_j in a given triad. Then, 10^7 sets of 114 triads were drawn, and the cases recorded in which at least 54 of 114 triads had the additional ExN_j-to-IN connection, in dependence of p_b and p_{det}=[65%, 70%, 75%]. A strict opponent inhibition model ($p_b\approx0$) was refuted at $p<10^{-7}$, as were connection probabilities p_b up to 30% (interpretable as opponent inhibition with 30% wiring noise). But even the chance model p_b=0.5 was refuted at $p=7*10^{-4}$, $p=4*10^{-3}$, p=0.02 for p_{det}=[65%, 70%, 75%], respectively, due to the limited detection probabilities p_{det}.

The effect of cFFI vs pFFI on the width of the postsynaptic AP timing distribution (Fig 3.6j) and number of APs (Fig 3.6 k) was compared using a two-sided t-test for unpaired samples (function ttest2). There, the mean and s.d. was calculated by dividing the total of 8000 simulations (2000 trials/cell) into n=20 blocks of 400 trials each (100 trials/cell).

The comparison of pathlength positions of IN output synapses involved in cFFI circuits with all output synapses of INs (Fig. 3.9c) was performed using a two-sided t-test for unpaired samples (n=884 and 131). The distribution of excitatory vs inhibitory axon diameters (Fig. 3.9h, inset; Fig. 3.10b) were compared using a two-sided t-test for unpaired samples (n=15 and 18) and Wilcoxon ranksum test. The test of the bias in number of inhibitory (IN) synapses over excitatory (ExN) synapses in the convergent cFFI circuits (Fig. 3.11c) was performed as a one-sided, right tailed, t-test (function ttest) of the relative IN/ExN number per connection against 1 (n=54 circuits). The distribution of dendritic Euclidean distance of excitatory vs inhibitory synapses onto the converging cell (Fig. 3.11d), as well as the pathlength distribution of inhibitory vs excitatory synapses of the same presynaptic axon (Fig. 3.11e), were compared over all n=54 cFFI circuits using a two-sided t-test for paired samples (function ttest2).

4 General Discussion

This thesis provided data on the mechanistic basis of the circuit operations in medial entorhinal cortex. It contributed to the discovery of modular organization of layer 2 (L2) neurons in the medial entorhinal cortex (MEC) in rat (chapter 2, (Ray et al., 2014; Tang et al., 2014b)) and the anatomical relation to the parasubiculum (chapter 2, (Tang et al., 2016)). The thesis furthermore provides a first detailed connectomic study of L2 in MEC, reporting the discovery of high-precision axonal architecture (path-length dependent axonal synapse sorting, PLASS) of excitatory and inhibitory neurons and the circuitry they are embedded in (chapter 3, (Schmidt et al., 2017)).

4.1 Structural modules in the medial entorhinal cortex (MEC)

Layer 2 of the MEC, which has been shown to contain grid cells (Hafting et al., 2005) is populated by two major principle cell types: pyramidal cells and stellate cells. Based on their intrinsic properties (Alonso and Klink, 1993), long-range projections to the hippocampus (Lingenhohl and Finch, 1991), and the disruption of spatial memory formation after activity manipulations (Rowland et al., 2013; Yasuda and Mayford, 2006), mainly stellate cells had been considered to exhibit temporally precise grid-like discharges. The results presented in chapter 2 of this thesis, however, found that, conspicuously, pyramidal cells (marked by calbindin immunoreactivity) bundle their dendrites together and form regularly arranged clusters, resembling the hexagonal firing pattern of grid cells in the environment. These clusters were aligned to the parasubiculum and the parallel, axonal bundles of deep layer 1. Further, calbindin-positive pyramidal cells showed a high overlap with parasubicular axons (Tang et al., 2016) and cholinergic inputs, and showed 2-fold

stronger theta-modulation in comparison to stellate cells, properties that are considered essential for the generation of grid-cell activity (Boccara et al., 2010; Brandon et al., 2011; Koenig et al., 2011; Sargolini et al., 2006). These findings suggest that pyramidal cells may contribute to the grid-like representation of space. Future studies have to show if the structural modules as identified by the pyramidal cell patches correspond to functional units in the medial entorhinal cortex.

4.1.1 Comparison to modular organization of primary sensory cortices

In primary sensory cortices, a modular organization of neurons into presumed functional units, called cortical columns, has been a major concept in neuroscience (Hubel and Wiesel, 1963; Mountcastle, 1957; Woolsey and Van der Loos, 1970). One pinnacle example of such cortical modules is the somatosensory cortex of rodents, in which the representation of the primary large whiskers in vertically aligned cellular units has been found to be easily detectable (Woolsey and Van der Loos, 1970). In rat, the modular unit at the level of the input layer 4 ("barrel") has a size of about 300 µm diameter in the tangential plane and about 200-400 µm in height (Meyer et al., 2010b). At first sight, the discovery of modularly arranged cell clusters in L2 of MEC seems stunningly similar to the barrels in layer 4 of primary somatosensory cortex. Therefore, both types of modular units made the dense circuit analysis an attractive goal in connectomics, where the minimal volume containing entire circuits is strongly limited. When considering this equivalence in more detail, however, numerical differences occur. First, the number of neurons in each patch in MEC is ~200 (Ray et al., 2014), but the number of neurons per barrel is an order of magnitude more (2000-4000, (Meyer et al., 2010b)). Secondly, the barrel units are clearly defined by thalamic input axons (see e.g. (Wimmer et al., 2010)). In the case of MEC, calbindin^{+} patches co-localize with cholinergic and parasubicular innervation. Importantly, barrels have so far been found in rodents and a small set of other species (but for example not in cats, primates or humans) while the MEC patches have already been described in species ranging from the smallest land-borne mammals (shrews) to humans (Naumann et al., 2016). So, while both patches in MEC and barrels in S1 are indications of modular organization in the mammalian cerebral cortex, their quantitative composition and evolutionary generality may be rather different. In both cases, however, the interior structure of these modules at the level of neuronal circuits is largely unknown.

4.1.2 MEC layer 2 modules: Patches vs. islands

The results on hexagonally arranged modules in MEC (chapter 2, (Ray et al., 2014)) were accompanied by a back-to-back report on cellular clusters in MEC and their long-range connectivity (Kitamura et al., 2014). In (Kitamura et al., 2014), the authors report similar findings on cell-type specific segregation in MEC. They find clusters of cells ("curvilinear matrix of 130-µm-diameter bulblike structures in tangential MEC"), containing mostly pyramidal neurons that express the protein Wolframin (the product of the gene Wfs1 (Kawano et al., 2009) associated with the Wolfram syndrome, a rare genetic disorder with a broad neurological and non-neurological phenotype) and calbindin (the authors refer to these as "island cells"). Stellate cells, surrounding the "islands" and therefore called "ocean cells", were identified as reelin-positive, dentate-gyrus projecting cells, confirming previous studies (Couey et al., 2013; Tamamaki and Nojyo, 1993; Varga et al., 2010) and the results in (Ray et al., 2014).

While (Ray et al., 2014) mostly investigated the arrangement of cell clusters, their inputs and the functional contributions of stellate and pyramidal cells, Kitamura et al. focused on the long-range outputs of "island" neurons in hippocampus and their role in fear conditioning. They found these cells to primarily project to the CA1 subregion of the hippocampus, with weaker projections detected in the subiculum, parasubiculum, and the contralateral CA1 and entorhinal cortex. The main input from the MEC to CA1 pyramidal cells is known to arise mainly from layer 3 neurons. Interestingly, Kitamura et al discovered that island cell axons preferentially target interneurons in CA1, which inhibit the same apical dendrites of CA1 pyramidal cells that are excited by entorhinal layer 3 cells. Thus, pyramidal cell clusters in layer 2 MEC may be in place to control the excitation of CA1 neurons mediated through entorhinal layer 3 cells.

4.2 Connectomic analysis, path length-dependent axonal synapse sorting (PLASS)

Evidently, an investigation of the underlying circuits was required in order to make progress at a mechanistic level understanding of MEC modules (chapter 3, Schmidt et al, 2017). This study, the main focus of this thesis, discovered a novel level of specificity in neuronal circuits of the mammalian cerebral cortex: (1) Output synapses are sorted along the axonal path (PLASS) of excitatory neurons in L2 of MEC with respect to the postsynaptic target (excitatory vs inhibitory neurons). (2) These axons participate in a cellular feed-forward

inhibition circuit. (3) Synapses cluster on the postsynaptic partner, especially onto interneurons. (4) The involved inhibitory neurons appear to be optimized for fast AP transmission, possessing myelinated, large-diameter axons. (5) A 2-fold excess of inhibitory synapses converging onto the postsynaptic neuron, positioned closer to the soma. These unexpected findings point to an even more intricate wiring in L2 MEC and emphasize the importance of connectomic analysis.

4.2.1 Sample size and reproduction

An important advance of this study was to replicate findings from large-scale reconstructions in two datasets, one from a P25 animal and one from a P90 animal. Such replication reflects the fact that connectomic analysis becomes increasingly more manageable and is especially relevant in a field in which so far most dense reconstruction studies have to be performed on single datasets, since the acquisition and analysis of even one dataset are so time consuming.

4.2.2 Comparison to other species and systems

The utilization of differential axonal conduction delay for precise temporal computations has been theoretically predicted (Jeffress, 1948) and experimentally observed (Carr and Konishi, 1988, 1990) in the bird auditory system where interaural time differences are compensated by synapse sequences along antiparallel axons, thus utilizing morphologically implemented delay lines. In the mammalian auditory system, however, such computational employment of axonal conduction delay has not been found. Rather, alternative models for interaural processing are being discussed (Ashida and Carr, 2011; Grothe et al., 2010; McAlpine and Grothe, 2003). Thus, the discovery of path length-dependent synapse sorting in the cerebral cortex of a mammal was most surprising. PLASS is different from synaptic target sorting based only on the spatial arrangement of neuronal target populations, such as when an axon passes through several subcortical nuclei, makes synapses first in cortex and then millimeters away in thalamus for cortico-thalamic neurons, or synaptic targets depend on the origin of the axon (e.g. CA1 vs CA3 in the hippocampal formation, (Takacs et al., 2012)). Similarly, a recent study from the bird brain (Kornfeld et al., 2017) described differential target innervation by axons along their trajectory through HVC, first targeting interneurons, and at a larger distance presumably excitatory neurons. This effect was distance (not exclusively path-length) dependent, and operated on spatial scales that yielded an interpretation as a winner-take all (opponent inhibition) model (their Fig. 3h, (Kornfeld

et al., 2017)). In contrast, PLASS constitutes synapse sorting at the local circuit scale, obvious only when analyzing local axonal path length at high resolution and sufficient spatial extent. Further, PLASS in mammalian cortex operates in a cellular feed-forward, not opponent inhibition, circuit.

4.2.3 Axonal conduction velocity

The measured offset of about 120 µm between the output synapses onto inhibitory and excitatory neurons along the presynaptic excitatory axon appears marginal to compensate for the time required to generate and conduct APs in the inhibitory branch of the circuit. The performed simulations indicate that a PLASS based delay of 0.5-1 ms would be sufficient to reliably suppress the propagation of highly synchronous presynaptic activity. This would imply low axonal AP conduction velocities of about 120-240 µm/ms. In most studies, axons are reported to exhibit larger conduction velocities (230-270 µm/ms: dentate granule neurons, (Kress et al., 2008; Schmidt-Hieber et al., 2008); 360 µm/ms: CA3 pyramidal neurons at 25°C – 450 µm/ms at 33°C (Meeks and Mennerick, 2007). An indirect estimate from rat S1 cortex however also provided 190 µm/ms (Helmstaedter et al., 2008d). Together with the data on axon diameters this makes it possible that excitatory neurons in MEC L2 exhibit especially thin and unmyelinated axons for reduced conduction velocity, enhancing the effect of spatial synapse sorting on conduction delay.

4.2.4 Non-linear dendritic integration

The simplified model of the PLASS-cFFI circuit (Fig. 3.11f) did not yet include the effect of local nonlinearities along the postsynaptic dendrites – the degree of synaptic clustering along the postsynaptic dendrites makes it well possible that NMDA- and Ca2+-dependent dendritic nonlinearities (Branco and Hausser, 2011; Larkum et al., 2009; Major et al., 2013; Major et al., 2008; Nevian et al., 2007) could further contribute to precisely timed postsynaptic activation of interneurons and excitatory neurons in this circuit.

4.2.5 Fast inhibition

One class of theoretical models proposed for the generation of grid cell activity is that of the attractor models. Typically, attractor models are based on the collective behavior of a neuronal network that can be abstracted via a Mexican hat connectivity (Burak and Fiete, 2009; Fuhs and Touretzky, 2006; McNaughton et al., 2006), yielding a wide distribution of

connectivity strength. Based on the finding that stellate cells are interconnected via inhibitory interneurons, a contemporary study proposed an inhibitory attractor model for grid formation that follows an all-or-none inhibitory connectivity (Couey et al., 2013). In fact, the discovery of PLASS and the properties of the cellular feed-forward inhibition circuit confirm and strengthen the importance of inhibition in L2 MEC. In addition, however, it emphasizes that not only the existence or strength of synaptic connections matters but also the timing in which inhibition operates. Furthermore, the fact that the results of this thesis imply substantial connectivity between excitatory neurons, that is however paired by strong inhibition, makes a pure inhibition-based attractor model less likely. It can even be speculated, that the lack of excitatory connectivity in slice-based electrophysiological connectivity studies could be a result of the strong parallel inhibition and only distal excitatory connectivity as found in this thesis.

4.2.6 Comparison to Cerebellum

An important feed-forward inhibitory circuit has been described in the cerebellum. There, excitatory mossy fibers excite granule cells as well as Golgi cells that in turn inhibit granule cells. Unlike the cellular feed-forward circuit that was found in the MEC, where one and the same presynaptic cell targets the inhibitory and excitatory neuron, inhibition in the cerebellar circuit was found to precede the excitatory input, with the implication of segregated and functionally distinct mossy fiber inputs onto granule and Golgi cells (Duguid et al., 2015). This data reported an offset of inhibition and excitation at the level of synaptic potentials. Such an offset could not be plausibly caused by PLASS as found here. Rather, the effect of PLASS becomes most clear when the integration of dozens of postsynaptic potentials is considered, and inhibitory effects can modulate the sequential input from excitatory synaptic sources.

4.3 Overall Conclusion

This thesis explores the architecture of the rat medial entorhinal cortex layer 2 at the light microscopic level (chapter 2) and at a more detailed level of description using state-of the-art 3-dimensional electron microscopy (chapter 3). The first study investigated the structure-function dichotomy in layer 2 of the medial entorhinal cortex, challenging the view that stellate cells are the major principle cell type in generating grid cell activity. The second study performed for the first time a detailed connectomic analysis of L2 MEC. The findings of modular cellular organization, path length-dependent axonal synapse sorting and cellular

feed-forward inhibitory circuits provide a novel level of insight into an intricate neuronal system. They emphasize that detailed connectomic analysis is required to make progress on a mechanistic understanding of circuits in the cerebral cortex. Both studies inspire future research of the microcircuits underlying grid formation, their generality across species, with a focus on the contribution of inhibition to activity propagation in MEC.

References

Agnati, L.F., Leo, G., Zanardi, A., Genedani, S., Rivera, A., Fuxe, K., and Guidolin, D. (2006). Volume transmission and wiring transmission from cellular to molecular networks: history and perspectives. Acta physiologica *187*, 329-344.

Ahmed, B., Anderson, J.C., Martin, K.A., and Nelson, J.C. (1997). Map of the synapses onto layer 4 basket cells of the primary visual cortex of the cat. The Journal of comparative neurology *380*, 230-242.

Alger, B.E., and Nicoll, R.A. (1982). Feed-forward dendritic inhibition in rat hippocampal pyramidal cells studied in vitro. J Physiol *328*, 105-123.

Alonso, A., and Klink, R. (1993). Differential electroresponsiveness of stellate and pyramidal-like cells of medial entorhinal cortex layer II. J Neurophysiol *70*, 128-143.

Alonso, A., and Llinas, R.R. (1989). Subthreshold Na+-dependent theta-like rhythmicity in stellate cells of entorhinal cortex layer II. Nature *342*, 175-177.

Arellano, J.I., Benavides-Piccione, R., De Felipe, J. & Yuste, R. (2007). Ultrastructure of dendritic spines: correlation between synaptic and spine morphologies. Front. Neurosci. *1*, 131-143.

Ashida, G., and Carr, C.E. (2011). Sound localization: Jeffress and beyond. Curr Opin Neurobiol *21*, 745-751.

Barry, C., Ginzberg, L.L., O'Keefe, J., and Burgess, N. (2012a). Grid cell firing patterns signal environmental novelty by expansion. Proc Natl Acad Sci U S A *109*, 17687-17692.

Barry, C., Heys, J.G., and Hasselmo, M.E. (2012b). Possible role of acetylcholine in regulating spatial novelty effects on theta rhythm and grid cells. Front Neural Circuits *6*, 5.

Beed, P., Bendels, M.H., Wiegand, H.F., Leibold, C., Johenning, F.W., and Schmitz, D. (2010). Analysis of excitatory microcircuitry in the medial entorhinal cortex reveals cell-type-specific differences. Neuron *68*, 1059-1066.

Berning, M., Boergens, K.M., and Helmstaedter, M. (2015). SegEM: Efficient Image Analysis for High-Resolution Connectomics. Neuron *87*, 1193-1206.

Binzegger, T., Douglas, R.J., and Martin, K.A. (2004). A quantitative map of the circuit of cat primary visual cortex. J Neurosci *24*, 8441-8453.

Blackstad, T.W. (1956). Commissural connections of the hippocampal region in the rat, with special reference to their mode of termination. The Journal of comparative neurology *105*, 417-537.

Boccara, C.N., Sargolini, F., Thoresen, V.H., Solstad, T., Witter, M.P., Moser, E.I., and Moser, M.B. (2010). Grid cells in pre- and parasubiculum. Nat Neurosci *13*, 987-994.

Bock, D.D., Lee, W.C., Kerlin, A.M., Andermann, M.L., Hood, G., Wetzel, A.W., Yurgenson, S., Soucy, E.R., Kim, H.S., and Reid, R.C. (2011). Network anatomy and in vivo physiology of visual cortical neurons. Nature *471*, 177-182.

Boergens, K.M., Berning, M., Bocklisch, T., Braunlein, D., Drawitsch, F., Frohnhofen, J., Herold, T., Otto, P., Rzepka, N., Werkmeister, T.*, et al.* (2017). webKnossos: efficient online 3D data annotation for connectomics. Nat Methods *14*, 691-694.

Bonnot, A., Mentis, G.Z., Skoch, J., and O'Donovan, M.J. (2005). Electroporation loading of calcium-sensitive dyes into the CNS. J Neurophysiol *93*, 1793-1808.

Bopp, R., Holler-Rickauer, S., Martin, K. A. & Schuhknecht, G. F. (2017). An ultrastructural study of the thalamic input to layer 4 of primary motor and primary somatosensory cortex in the mouse. J. Neurosci. *37*, 2435–2448.

Braitenberg, V., and Schüz, A. (1998). Cortex: Statistics and Geometry of Neuronal Connectivity (Berlin Heidelberg: Springer).

Branco, T., and Hausser, M. (2011). Synaptic integration gradients in single cortical pyramidal cell dendrites. Neuron *69*, 885-892.

Brandon, M.P., Bogaard, A.R., Libby, C.P., Connerney, M.A., Gupta, K., and Hasselmo, M.E. (2011). Reduction of theta rhythm dissociates grid cell spatial periodicity from directional tuning. Science *332*, 595-599.

Brecht, M., Ray, S., Burgalossi, A., Tang, Q., Schmidt, H., and Naumann, R. (2014). An isomorphic mapping hypothesis of the grid representation. Philos Trans R Soc Lond B Biol Sci *369*, 20120521.

Brecht, M., Roth, A., and Sakmann, B. (2003). Dynamic receptive fields of reconstructed pyramidal cells in layers 3 and 2 of rat somatosensory barrel cortex. J Physiol *553*, 243-265.

Brecht, M., and Sakmann, B. (2002a). Dynamic representation of whisker deflection by synaptic potentials in spiny stellate and pyramidal cells in the barrels and septa of layer 4 rat somatosensory cortex. J Physiol *543*, 49-70.

Brecht, M., and Sakmann, B. (2002b). Whisker maps of neuronal subclasses of the rat ventral posterior medial thalamus, identified by whole-cell voltage recording and morphological reconstruction. J Physiol *538*, 495-515.

Brecht, M., and Sakmann, B. (2002c). Whisker maps of neuronal subclasses of the rat ventral posterior medial thalamus, identified by whole-cell voltage recording and morphological reconstruction. The Journal of physiology *538*, 495-515.

Briggman, K.L., and Bock, D.D. (2012). Volume electron microscopy for neuronal circuit reconstruction. Curr Opin Neurobiol *22*, 154-161.

Briggman, K.L., Helmstaedter, M., and Denk, W. (2011). Wiring specificity in the direction-selectivity circuit of the retina. Nature *471*, 183-188.

Brodmann, K. (1909). Vergleichende Lokalisationslehre der Grosshirnrinde in ihren Prinzipien dargestellt auf Grund des Zellenbaues (Barth).

Bruno, R.M. (2011). Synchrony in sensation. Curr Opin Neurobiol *21*, 701-708.

Bruno, R.M., and Simons, D.J. (2002). Feedforward mechanisms of excitatory and inhibitory cortical receptive fields. J Neurosci *22*, 10966-10975.

Burak, Y., and Fiete, I.R. (2009). Accurate path integration in continuous attractor network models of grid cells. PLoS Comput Biol *5*, e1000291.

Burgalossi, A., and Brecht, M. (2014). Cellular, columnar and modular organization of spatial representations in medial entorhinal cortex. Curr Opin Neurobiol *24*, 47-54.

Burgalossi, A., Herfst, L., von Heimendahl, M., Forste, H., Haskic, K., Schmidt, M., and Brecht, M. (2011). Microcircuits of functionally identified neurons in the rat medial entorhinal cortex. Neuron *70*, 773-786.

Buzsaki, G. (1984). Feed-forward inhibition in the hippocampal formation. Prog Neurobiol *22*, 131-153.

Canto, C.B., and Witter, M.P. (2012). Cellular properties of principal neurons in the rat entorhinal cortex. II. The medial entorhinal cortex. Hippocampus *22*, 1277-1299.

Canto, C.B., Wouterlood, F.G., and Witter, M.P. (2008). What does the anatomical organization of the entorhinal cortex tell us? Neural plasticity *2008*, 381243.

Cardona, A., Saalfeld, S., Preibisch, S., Schmid, B., Cheng, A., Pulokas, J., Tomancak, P., and Hartenstein, V. (2010). An integrated micro- and macroarchitectural analysis of the Drosophila brain by computer-assisted serial section electron microscopy. PLoS biology *8*.

Carr, C.E., and Konishi, M. (1988). Axonal delay lines for time measurement in the owl's brainstem. Proc Natl Acad Sci U S A *85*, 8311-8315.

Carr, C.E., and Konishi, M. (1990). A circuit for detection of interaural time differences in the brain stem of the barn owl. J Neurosci *10*, 3227-3246.

Catania, K.C., Northcutt, R.G., Kaas, J.H., and Beck, P.D. (1993). Nose stars and brain stripes. Nature *364*, 493.

Chapuis, J., Cohen, Y., He, X., Zhang, Z., Jin, S., Xu, F., and Wilson, D.A. (2013). Lateral entorhinal modulation of piriform cortical activity and fine odor discrimination. J Neurosci *33*, 13449-13459.

Couey, J.J., Witoelar, A., Zhang, S.J., Zheng, K., Ye, J., Dunn, B., Czajkowski, R., Moser, M.B., Moser, E.I., Roudi, Y.*, et al.* (2013). Recurrent inhibitory circuitry as a mechanism for grid formation. Nat Neurosci *16*, 318-324.

Cruikshank, S.J., Lewis, T.J., and Connors, B.W. (2007). Synaptic basis for intense thalamocortical activation of feedforward inhibitory cells in neocortex. Nat Neurosci *10*, 462-468.

de Kock, C.P., Bruno, R.M., Spors, H., and Sakmann, B. (2007). Layer- and cell-type-specific suprathreshold stimulus representation in rat primary somatosensory cortex. J Physiol *581*, 139-154.

Denk, W., Briggman, K.L., and Helmstaedter, M. (2012). Structural neurobiology: missing link to a mechanistic understanding of neural computation. Nat Rev Neurosci *13*, 351-358.

Denk, W., and Horstmann, H. (2004). Serial block-face scanning electron microscopy to reconstruct three-dimensional tissue nanostructure. PLoS biology *2*, e329.

Denk, W., Strickler, J.H., and Webb, W.W. (1990). Two-photon laser scanning fluorescence microscopy. Science *248*, 73-76.

Deshmukh, S.S., and Knierim, J.J. (2011). Representation of non-spatial and spatial information in the lateral entorhinal cortex. Front Behav Neurosci *5*, 69.

de Vivo, L., Bellesi, M., Marshall, W., Bushong, E.A., Ellisman, M.H., Tononi, G., Cirelli, C. (2017). Ultrastructural evidence for synaptic scaling across the wake/sleep cycle. Science *355*, 507-510.

Dhillon, A., and Jones, R.S. (2000). Laminar differences in recurrent excitatory transmission in the rat entorhinal cortex in vitro. Neuroscience *99*, 413-422.

Dorkenwald, S., Schubert, P.J., Killinger, M.F., Urban, G., Mikula, S., Svara, F., and Kornfeld, J. (2017). Automated synaptic connectivity inference for volume electron microscopy. Nat Methods *14*, 435-442.

Douglas, R.J., and Martin, K.A. (1991). A functional microcircuit for cat visual cortex. J Physiol *440*, 735-769.

Douglas, R.J., and Martin, K.A. (2004). Neuronal circuits of the neocortex. Annu Rev Neurosci *27*, 419-451.

Douglas, R.J., Martin, K.A., and Whitteridge, D. (1989). A canonical microcircuit for neocortex. Neural computation *1*, 480-488.

Duguid, I., Branco, T., Chadderton, P., Arlt, C., Powell, K., and Hausser, M. (2015). Control of cerebellar granule cell output by sensory-evoked Golgi cell inhibition. Proc Natl Acad Sci U S A *112*, 13099-13104.

Eccles, J., Llinas, R., and Sasaki, K. (1964). Golgi Cell Inhibition in the Cerebellar Cortex. Nature *204*, 1265-1266.

Eichler, K., Li, F., Litwin-Kumar, A., Park, Y., Andrade, I., Schneider-Mizell, C.M., Saumweber, T., Huser, A., Eschbach, C., Gerber, B.*, et al.* (2017). The complete connectome of a learning and memory centre in an insect brain. Nature *548*, 175-182.

Fatt, P., and Katz, B. (1950). Membrane potentials at the motor end-plate. J Physiol *111*, 46p-47p.

Feldmeyer, D., Egger, V., Lubke, J., and Sakmann, B. (1999). Reliable synaptic connections between pairs of excitatory layer 4 neurones within a single 'barrel' of developing rat somatosensory cortex. J Physiol *521 Pt 1*, 169-190.

Feldmeyer, D., Lubke, J., Silver, R.A., and Sakmann, B. (2002). Synaptic connections between layer 4 spiny neurone-layer 2/3 pyramidal cell pairs in juvenile rat barrel cortex: physiology and anatomy of interlaminar signalling within a cortical column. J Physiol *538*, 803-822.

Felleman, D.J., and Van Essen, D.C. (1991). Distributed hierarchical processing in the primate cerebral cortex. Cereb Cortex *1*, 1-47.

Feng, G., Mellor, R.H., Bernstein, M., Keller-Peck, C., Nguyen, Q.T., Wallace, M., Nerbonne, J.M., Lichtman, J.W., and Sanes, J.R. (2000). Imaging neuronal subsets in transgenic mice expressing multiple spectral variants of GFP. Neuron *28*, 41-51.

Fuchs, E.C., Neitz, A., Pinna, R., Melzer, S., Caputi, A., and Monyer, H. (2016). Local and Distant Input Controlling Excitation in Layer II of the Medial Entorhinal Cortex. Neuron *89*, 194-208.

Fuhs, M.C., and Touretzky, D.S. (2006). A spin glass model of path integration in rat medial entorhinal cortex. J Neurosci *26*, 4266-4276.

Fujimaru, Y., and Kosaka, T. (1996). The distribution of two calcium binding proteins, calbindin D-28K and parvalbumin, in the entorhinal cortex of the adult mouse. Neurosci Res *24*, 329-343.

Garaschuk, O., Linn, J., Eilers, J., and Konnerth, A. (2000). Large-scale oscillatory calcium waves in the immature cortex. Nat Neurosci *3*, 452-459.

Genoud, C., Quairiaux, C., Steiner, P., Hirling, H., Welker, E., and Knott, G.W. (2006). Plasticity of astrocytic coverage and glutamate transporter expression in adult mouse cortex. PLoS biology *4*, e343.

Germroth, P., Schwerdtfeger, W.K., and Buhl, E.H. (1989). Morphology of identified entorhinal neurons projecting to the hippocampus. A light microscopical study combining retrograde tracing and intracellular injection. Neuroscience *30*, 683-691.

Ghosh, S., Brinkman, C., and Porter, R. (1987). A quantitative study of the distribution of neurons projecting to the precentral motor cortex in the monkey (M. fascicularis). The Journal of comparative neurology *259*, 424-444.

Gilbert, C.D., and Wiesel, T.N. (1983). Clustered intrinsic connections in cat visual cortex. J Neurosci *3*, 1116-1133.

Grewe, B.F., Langer, D., Kasper, H., Kampa, B.M., and Helmchen, F. (2010). High-speed in vivo calcium imaging reveals neuronal network activity with near-millisecond precision. Nature methods *7*, 399-405.

Grothe, B., Pecka, M., and McAlpine, D. (2010). Mechanisms of sound localization in mammals. Physiological reviews *90*, 983-1012.

Gupta, A., Wang, Y., and Markram, H. (2000). Organizing principles for a diversity of GABAergic interneurons and synapses in the neocortex. Science *287*, 273-278.

Hafting, T., Fyhn, M., Bonnevie, T., Moser, M.B., and Moser, E.I. (2008). Hippocampus-independent phase precession in entorhinal grid cells. Nature *453*, 1248-1252.

Hafting, T., Fyhn, M., Molden, S., Moser, M.B., and Moser, E.I. (2005). Microstructure of a spatial map in the entorhinal cortex. Nature *436*, 801-806.

Harris, K.M., Perry, E., Bourne, J., Feinberg, M., Ostroff, L., and Hurlburt, J. (2006). Uniform serial sectioning for transmission electron microscopy. J Neurosci *26*, 12101-12103.

Harris, K.M., and Stevens, J.K. (1988). Dendritic spines of rat cerebellar Purkinje cells: serial electron microscopy with reference to their biophysical characteristics. J Neurosci *8*, 4455-4469.

Harris, K.M., and Stevens, J.K. (1989). Dendritic spines of CA 1 pyramidal cells in the rat hippocampus: serial electron microscopy with reference to their biophysical characteristics. J Neurosci *9*, 2982-2997.

Hasselmo, M.E., Giocomo, L.M., and Zilli, E.A. (2007). Grid cell firing may arise from interference of theta frequency membrane potential oscillations in single neurons. Hippocampus *17*, 1252-1271.

Hasselmo, M.E., and McGaughy, J. (2004). High acetylcholine levels set circuit dynamics for attention and encoding and low acetylcholine levels set dynamics for consolidation. Prog Brain Res *145*, 207-231.

Hausser, M., Stuart, G., Racca, C., and Sakmann, B. (1995). Axonal initiation and active dendritic propagation of action potentials in substantia nigra neurons. Neuron *15*, 637-647.

Hayworth, K.J., Kasthuri, N., Schalek, R., and Lichtman, J.W. (2006). Automating the Collection of Ultrathin Serial Sections for Large Volume TEM Reconstructions. Microsc Microanal *12 (Supp2)*, 86-87.

Helmchen, F., Fee, M.S., Tank, D.W., and Denk, W. (2001). A miniature head-mounted two-photon microscope. high-resolution brain imaging in freely moving animals. Neuron *31*, 903-912.

Helmstaedter, M. (2013). Cellular-resolution connectomics: challenges of dense neural circuit reconstruction. Nat Methods *10*, 501-507.

Helmstaedter, M., Briggman, K.L., and Denk, W. (2008a). 3D structural imaging of the brain with photons and electrons. Curr Opin Neurobiol *18*, 633-641.

Helmstaedter, M., Briggman, K.L., and Denk, W. (2011). High-accuracy neurite reconstruction for high-throughput neuroanatomy. Nat Neurosci *14*, 1081-1088.

Helmstaedter, M., Briggman, K.L., Turaga, S.C., Jain, V., Seung, H.S., and Denk, W. (2013). Connectomic reconstruction of the inner plexiform layer in the mouse retina. Nature *500*, 168-174.

Helmstaedter, M., and Mitra, P.P. (2012). Computational methods and challenges for large-scale circuit mapping. Curr Opin Neurobiol *22*, 162-169.

Helmstaedter, M., Sakmann, B., and Feldmeyer, D. (2008b). Neuronal Correlates of Local, Lateral, and Translaminar Inhibition with Reference to Cortical Columns. Cereb Cortex.

Helmstaedter, M., Sakmann, B., and Feldmeyer, D. (2008c). The Relation between Dendritic Geometry, Electrical Excitability, and Axonal Projections of L2/3 Interneurons in Rat Barrel Cortex. Cereb Cortex.

Helmstaedter, M., Staiger, J.F., Sakmann, B., and Feldmeyer, D. (2008d). Efficient recruitment of layer 2/3 interneurons by layer 4 input in single columns of rat somatosensory cortex. J Neurosci *28*, 8273-8284.

Hennig, P., and Denk, W. (2007). Point-spread functions for backscattered imaging in the scanning electron microscope. J Appl Phys *102*, 123101.

Heymann, J.A., Hayles, M., Gestmann, I., Giannuzzi, L.A., Lich, B., and Subramaniam, S. (2006). Site-specific 3D imaging of cells and tissues with a dual beam microscope. J Struct Biol *155*, 63-73.

Heys, J.G., Schultheiss, N.W., Shay, C.F., Tsuno, Y., and Hasselmo, M.E. (2012). Effects of acetylcholine on neuronal properties in entorhinal cortex. Front Behav Neurosci *6*, 32.

Hildebrand, D.G.C., Cicconet, M., Torres, R.M., Choi, W., Quan, T.M., Moon, J., Wetzel, A.W., Scott Champion, A., Graham, B.J., Randlett, O.*, et al.* (2017). Whole-brain serial-section electron microscopy in larval zebrafish. Nature *545*, 345-349.

Hodgkin, A.L., and Huxley, A.F. (1952). A quantitative description of membrane current and its application to conduction and excitation in nerve. J Physiol *117*, 500-544.

Hoffmann, J.H., Meyer, H.S., Schmitt, A.C., Straehle, J., Weitbrecht, T., Sakmann, B., and Helmstaedter, M. (2015). Synaptic Conductance Estimates of the Connection Between Local Inhibitor Interneurons and Pyramidal Neurons in Layer 2/3 of a Cortical Column. Cereb Cortex *25*, 4415-4429.

Holtmaat, A., Wilbrecht, L., Knott, G.W., Welker, E., and Svoboda, K. (2006). Experience-dependent and cell-type-specific spine growth in the neocortex. Nature *441*, 979-983.

Horikawa, K., and Armstrong, W.E. (1988). A versatile means of intracellular labeling: injection of biocytin and its detection with avidin conjugates. J Neurosci Meth *25*, 1-11.

Hua, Y., Laserstein, P., and Helmstaedter, M. (2015). Large-volume en-bloc staining for electron microscopy-based connectomics. Nat Commun *6*, 7923.

Hubel, D.H., and Wiesel, T.N. (1963). Shape and arrangement of columns in cat's striate cortex. J Physiol *165*, 559-568.

Ichinohe, N., Knight, A., Ogawa, M., Ohshima, T., Mikoshiba, K., Yoshihara, Y., Terashima, T., and Rockland, K.S. (2008). Unusual patch-matrix organization in the retrosplenial cortex of the reeler mouse and Shaking rat Kawasaki. Cereb Cortex *18*, 1125-1138.

Insausti, R., and Amaral, D.G. (2008). Entorhinal cortex of the monkey: IV. Topographical and laminar organization of cortical afferents. The Journal of comparative neurology *509*, 608-641.

Jährling, N., Becker, K., Kramer, E.R., and Dodt, H.-U. (2008). 3D-Visualization of nerve fiber bundles by ultramicroscopy. Medical Laser Application *23*, 209-215.

Jeffress, L.A. (1948). A place theory of sound localization. Journal of comparative and physiological psychology *41*, 35-39.

Jiang, X., Shen, S., Cadwell, C.R., Berens, P., Sinz, F., Ecker, A.S., Patel, S., and Tolias, A.S. (2015). Principles of connectivity among morphologically defined cell types in adult neocortex. Science *350*, aac9462.

Judkewitz, B., Rizzi, M., Kitamura, K., and Hausser, M. (2009). Targeted single-cell electroporation of mammalian neurons in vivo. Nat Protoc *4*, 862-869.

Kanichay, R.T., and Silver, R.A. (2008). Synaptic and cellular properties of the feedforward inhibitory circuit within the input layer of the cerebellar cortex. J Neurosci *28*, 8955-8967.

Kasthuri, N., Hayworth, K.J., Berger, D.R., Schalek, R.L., Conchello, J.A., Knowles-Barley, S., Lee, D., Vazquez-Reina, A., Kaynig, V., Jones, T.R., *et al.* (2015). Saturated Reconstruction of a Volume of Neocortex. Cell *162*, 648-661.

Kasthuri, N., and Lichtman, J.W. (2007). The rise of the 'projectome'. Nat Methods *4*, 307-308.

Kawano, J., Fujinaga, R., Yamamoto-Hanada, K., Oka, Y., Tanizawa, Y., and Shinoda, K. (2009). Wolfram syndrome 1 (Wfs1) mRNA expression in the normal mouse brain during postnatal development. Neurosci Res *64*, 213-230.

Kerr, J.N., Greenberg, D., and Helmchen, F. (2005). Imaging input and output of neocortical networks in vivo. Proc Natl Acad Sci U S A *102*, 14063-14068.

Kerr, K.M., Agster, K.L., Furtak, S.C., and Burwell, R.D. (2007). Functional neuroanatomy of the parahippocampal region: the lateral and medial entorhinal areas. Hippocampus *17*, 697-708.

Kitamura, K., Judkewitz, B., Kano, M., Denk, W., and Hausser, M. (2008). Targeted patch-clamp recordings and single-cell electroporation of unlabeled neurons in vivo. Nature methods *5*, 61-67.

Kitamura, T., Pignatelli, M., Suh, J., Kohara, K., Yoshiki, A., Abe, K., and Tonegawa, S. (2014). Island cells control temporal association memory. Science *343*, 896-901.

Klausberger, T., Magill, P.J., Marton, L.F., Roberts, J.D., Cobden, P.M., Buzsaki, G., and Somogyi, P. (2003). Brain-state- and cell-type-specific firing of hippocampal interneurons in vivo. Nature *421*, 844-848.

Klink, R., and Alonso, A. (1997). Muscarinic modulation of the oscillatory and repetitive firing properties of entorhinal cortex layer II neurons. J Neurophysiol *77*, 1813-1828.

Kloosterman, F., Van Haeften, T., Witter, M.P., and Lopes Da Silva, F.H. (2003). Electrophysiological characterization of interlaminar entorhinal connections: an essential link for re-entrance in the hippocampal-entorhinal system. Eur J Neurosci *18*, 3037-3052.

Knott, G., Marchman, H., Wall, D., and Lich, B. (2008). Serial section scanning electron microscopy of adult brain tissue using focused ion beam milling. J Neurosci *28*, 2959-2964.

Koelbl, C., Helmstaedter, M., Lubke, J., and Feldmeyer, D. (2015). A barrel-related interneuron in layer 4 of rat somatosensory cortex with a high intrabarrel connectivity. Cereb Cortex *25*, 713-725.

Koenig, J., Linder, A.N., Leutgeb, J.K., and Leutgeb, S. (2011). The spatial periodicity of grid cells is not sustained during reduced theta oscillations. Science *332*, 592-595.

Koganezawa, N., Gisetstad, R., Husby, E., Doan, T.P., and Witter, M.P. (2015). Excitatory Postrhinal Projections to Principal Cells in the Medial Entorhinal Cortex. J Neurosci *35*, 15860-15874.

Komiyama, T., Sato, T.R., O'Connor, D.H., Zhang, Y.X., Huber, D., Hooks, B.M., Gabitto, M., and Svoboda, K. (2010). Learning-related fine-scale specificity imaged in motor cortex circuits of behaving mice. Nature *464*, 1182-1186.

Kornfeld, J., Benezra, S.E., Narayanan, R.T., Svara, F., Egger, R., Oberlaender, M., Denk, W., and Long, M.A. (2017). EM connectomics reveals axonal target variation in a sequence-generating network. Elife *6*.

Kreshuk, A., Straehle, C.N., Sommer, C., Koethe, U., Cantoni, M., Knott, G., and Hamprecht, F.A. (2011). Automated detection and segmentation of synaptic contacts in nearly isotropic serial electron microscopy images. PLoS One *6*, e24899.

Kress, G.J., Dowling, M.J., Meeks, J.P., and Mennerick, S. (2008). High threshold, proximal initiation, and slow conduction velocity of action potentials in dentate granule neuron mossy fibers. J Neurophysiol *100*, 281-291.

Krupic, J., Burgess, N., and O'Keefe, J. (2012). Neural representations of location composed of spatially periodic bands. Science *337*, 853-857.

Langston, R.F., Ainge, J.A., Couey, J.J., Canto, C.B., Bjerknes, T.L., Witter, M.P., Moser, E.I., and Moser, M.B. (2010). Development of the spatial representation system in the rat. Science *328*, 1576-1580.

Larkum, M.E., Nevian, T., Sandler, M., Polsky, A., and Schiller, J. (2009). Synaptic integration in tuft dendrites of layer 5 pyramidal neurons: a new unifying principle. Science *325*, 756-760.

Larkum, M.E., Zhu, J.J., and Sakmann, B. (1999). A new cellular mechanism for coupling inputs arriving at different cortical layers. Nature *398*, 338-341.

Lee, A.K., Manns, I.D., Sakmann, B., and Brecht, M. (2006). Whole-cell recordings in freely moving rats. Neuron *51*, 399-407.

Lee, W.C., Bonin, V., Reed, M., Graham, B.J., Hood, G., Glattfelder, K., and Reid, R.C. (2016). Anatomy and function of an excitatory network in the visual cortex. Nature *532*, 370-374.

Lingenhohl, K., and Finch, D.M. (1991). Morphological characterization of rat entorhinal neurons in vivo: soma-dendritic structure and axonal domains. Exp Brain Res *84*, 57-74.

Lorente de No, R. (1922). La corteza cerebral de ratón Trabajos del Laboratorio de Investigaciones Biológicas de la Universidad de Madrid *20*, 41-78.

Lorente de No, R. (1992). The cerebral cortex of the mouse (A first contribution--the "acoustic" cortex). (Transl. A Fairén, J Regidor, L Kruger). Somat Mot Res *9*, 3-36.

Lorente de Nó, R. (1938). Cerebral cortex: architecture, intracortical connections, motor projections. In Physiology of the Nervous System, J.F. Fulton, ed. ((1949). London: Oxford University Press), p. 300.

Lubke, J., Egger, V., Sakmann, B., and Feldmeyer, D. (2000). Columnar organization of dendrites and axons of single and synaptically coupled excitatory spiny neurons in layer 4 of the rat barrel cortex. J Neurosci *20*, 5300-5311.

Lubke, J., Roth, A., Feldmeyer, D., and Sakmann, B. (2003). Morphometric analysis of the columnar innervation domain of neurons connecting layer 4 and layer 2/3 of juvenile rat barrel cortex. Cereb Cortex *13*, 1051-1063.

Lund, J.S., Henry, G.H., MacQueen, C.L., and Harvey, A.R. (1979). Anatomical organization of the primary visual cortex (area 17) of the cat. A comparison with area 17 of the macaque monkey. The Journal of comparative neurology *184*, 599-618.

Major, G., Larkum, M.E., and Schiller, J. (2013). Active properties of neocortical pyramidal neuron dendrites. Annu Rev Neurosci *36*, 1-24.

Major, G., Polsky, A., Denk, W., Schiller, J., and Tank, D.W. (2008). Spatiotemporally graded NMDA spike/plateau potentials in basal dendrites of neocortical pyramidal neurons. Journal of neurophysiology *99*, 2584-2601.

Margrie, T.W., Brecht, M., and Sakmann, B. (2002). In vivo, low-resistance, whole-cell recordings from neurons in the anaesthetized and awake mammalian brain. Pflugers Arch *444*, 491-498.

Markram, H., Lubke, J., Frotscher, M., Roth, A., and Sakmann, B. (1997a). Physiology and anatomy of synaptic connections between thick tufted pyramidal neurones in the developing rat neocortex. J Physiol *500 (Pt 2)*, 409-440.

Markram, H., Lubke, J., Frotscher, M., and Sakmann, B. (1997b). Regulation of synaptic efficacy by coincidence of postsynaptic APs and EPSPs. Science *275*, 213-215.

Markram, H., Toledo-Rodriguez, M., Wang, Y., Gupta, A., Silberberg, G., and Wu, C. (2004). Interneurons of the neocortical inhibitory system. Nat Rev Neurosci *5*, 793-807.

Marshel, J.H., Mori, T., Nielsen, K.J., and Callaway, E.M. (2010). Targeting single neuronal networks for gene expression and cell labeling in vivo. Neuron *67*, 562-574.

Marx, M., Gunter, R.H., Hucko, W., Radnikow, G., and Feldmeyer, D. (2012). Improved biocytin labeling and neuronal 3D reconstruction. Nat Protoc *7*, 394-407.

McAlpine, D., and Grothe, B. (2003). Sound localization and delay lines--do mammals fit the model? Trends Neurosci *26*, 347-350.

McNaughton, B.L., Battaglia, F.P., Jensen, O., Moser, E.I., and Moser, M.B. (2006). Path integration and the neural basis of the 'cognitive map'. Nat Rev Neurosci *7*, 663-678.

Meeks, J.P., and Mennerick, S. (2007). Action potential initiation and propagation in CA3 pyramidal axons. J Neurophysiol *97*, 3460-3472.

Meyer, H.S., Wimmer, V.C., Hemberger, M., Bruno, R.M., de Kock, C.P., Frick, A., Sakmann, B., and Helmstaedter, M. (2010a). Cell type-specific thalamic innervation in a column of rat vibrissal cortex. Cereb Cortex *20*, 2287-2303.

Meyer, H.S., Wimmer, V.C., Oberlaender, M., de Kock, C.P., Sakmann, B., and Helmstaedter, M. (2010b). Number and laminar distribution of neurons in a thalamocortical projection column of rat vibrissal cortex. Cereb Cortex *20*, 2277-2286.

Micheva, K.D., Wolman, D., Mensh, B.D., Pax, E., Buchanan, J., Smith, S.J., and Bock, D.D. (2016). A large fraction of neocortical myelin ensheathes axons of local inhibitory neurons. Elife *5*.

Mishchenko, Y., Hu, T., Spacek, J., Mendenhall, J., Harris, K.M., and Chklovskii, D.B. (2010). Ultrastructural analysis of hippocampal neuropil from the connectomics perspective. Neuron *67*, 1009-1020.

Mittmann, W., Wallace, D.J., Czubayko, U., Herb, J.T., Schaefer, A.T., Looger, L.L., Denk, W., and Kerr, J.N. (2011). Two-photon calcium imaging of evoked activity from L5 somatosensory neurons in vivo. Nature neuroscience *14*, 1089-1093.

Mizuseki, K., Sirota, A., Pastalkova, E., and Buzsaki, G. (2009). Theta oscillations provide temporal windows for local circuit computation in the entorhinal-hippocampal loop. Neuron *64*, 267-280.

Mountcastle, V.B. (1957). Modality and topographic properties of single neurons of cat's somatic sensory cortex. J Neurophysiol *20*, 408-434.

Murayama, M., Perez-Garci, E., Luscher, H.R., and Larkum, M.E. (2007). Fiberoptic system for recording dendritic calcium signals in layer 5 neocortical pyramidal cells in freely moving rats. Journal of neurophysiology *98*, 1791-1805.

Naumann, R.K., Ray, S., Prokop, S., Las, L., Heppner, F.L., and Brecht, M. (2016). Conserved size and periodicity of pyramidal patches in layer 2 of medial/caudal entorhinal cortex. The Journal of comparative neurology *524*, 783-806.

Nevian, T., and Helmchen, F. (2007). Calcium indicator loading of neurons using single-cell electroporation. Pflugers Archiv : European journal of physiology *454*, 675-688.

Nevian, T., Larkum, M.E., Polsky, A., and Schiller, J. (2007). Properties of basal dendrites of layer 5 pyramidal neurons: a direct patch-clamp recording study. Nat Neurosci *10*, 206-214.

Oberlaender, M., Boudewijns, Z.S., Kleele, T., Mansvelder, H.D., Sakmann, B., and de Kock, C.P. (2011). Three-dimensional axon morphologies of individual layer 5 neurons indicate cell type-specific intracortical pathways for whisker motion and touch. Proc Natl Acad Sci U S A *108*, 4188-4193.

Okabe, M., Ikawa, M., Kominami, K., Nakanishi, T., and Nishimune, Y. (1997). 'Green mice' as a source of ubiquitous green cells. FEBS Lett *407*, 313-319.

Pastoll, H., Solanka, L., van Rossum, M.C., and Nolan, M.F. (2013). Feedback inhibition enables theta-nested gamma oscillations and grid firing fields. Neuron *77*, 141-154.

Peters, A., and Jones, E.G. (1984a). Classification of Cortical Neurons. In Cerebral cortex: cellular components of the cerebral cortex, A. Peters, and E.G. Jones, eds. (New York: Plenum Press), pp. 107-120.

Peters, A., and Jones, E.G. (1984b). Cytoarchitectonics. In Cerebral cortex: cellular components of the cerebral cortex, A. Peters, and E.G. Jones, eds. (New York: Plenum Press), pp. 35-99.

Peters, A., and Palay, S.L. (1991). The fine structure of the nervous system: neurons and their supporting cells (Oxford University Press, USA).

Peterson, D.A., Lucidi-Phillipi, C.A., Murphy, D.P., Ray, J., and Gage, F.H. (1996). Fibroblast growth factor-2 protects entorhinal layer II glutamatergic neurons from axotomy-induced death. J Neurosci *16*, 886-898.

Petilla Interneuron Nomenclature, G., Ascoli, G.A., Alonso-Nanclares, L., Anderson, S.A., Barrionuevo, G., Benavides-Piccione, R., Burkhalter, A., Buzsaki, G., Cauli, B., Defelipe, J., *et al.* (2008). Petilla terminology: nomenclature of features of GABAergic interneurons of the cerebral cortex. Nat Rev Neurosci *9*, 557-568.

Pinault, D. (1996). A novel single-cell staining procedure performed in vivo under electrophysiological control: morpho-functional features of juxtacellularly labeled thalamic cells and other central neurons with biocytin or Neurobiotin. Journal of neuroscience methods *65*, 113-136.

Pouille, F., and Scanziani, M. (2001). Enforcement of temporal fidelity in pyramidal cells by somatic feed-forward inhibition. Science *293*, 1159-1163.

Preibisch, S., Saalfeld, S., and Tomancak, P. (2009). Globally optimal stitching of tiled 3D microscopic image acquisitions. Bioinformatics *25*, 1463-1465.

Quilichini, P., Sirota, A., and Buzsaki, G. (2010). Intrinsic circuit organization and theta-gamma oscillation dynamics in the entorhinal cortex of the rat. J Neurosci *30*, 11128-11142.

Ramón y Cajal, S. (1899). Textura del Sistema Nervioso del hombre y de los vertebrados, Vol 1 (Madrid: Moya).

Ramón y Cajal, S. (1995). Histology of the Nervous System (New York Oxford: Oxford University Press).

Ray, S., Burgalossi, A., Brecht, M., and Naumann, R.K. (2017). Complementary Modular Microcircuits of the Rat Medial Entorhinal Cortex. Frontiers in systems neuroscience *11*, 20.

Ray, S., Naumann, R., Burgalossi, A., Tang, Q., Schmidt, H., and Brecht, M. (2014). Grid-layout and theta-modulation of layer 2 pyramidal neurons in medial entorhinal cortex. Science *343*, 891-896.

Rowland, D.C., Weible, A.P., Wickersham, I.R., Wu, H., Mayford, M., Witter, M.P., and Kentros, C.G. (2013). Transgenically targeted rabies virus demonstrates a major

monosynaptic projection from hippocampal area CA2 to medial entorhinal layer II neurons. J Neurosci *33*, 14889-14898.

Sargolini, F., Fyhn, M., Hafting, T., McNaughton, B.L., Witter, M.P., Moser, M.B., and Moser, E.I. (2006). Conjunctive representation of position, direction, and velocity in entorhinal cortex. Science *312*, 758-762.

Schmidt-Hieber, C., Jonas, P., and Bischofberger, J. (2008). Action potential initiation and propagation in hippocampal mossy fibre axons. J Physiol *586*, 1849-1857.

Schuz, A., and Palm, G. (1989). Density of neurons and synapses in the cerebral cortex of the mouse. The Journal of comparative neurology *286*, 442-455.

Schwartz, S.P., and Coleman, P.D. (1981). Neurons of origin of the perforant path. Exp Neurol *74*, 305-312.

Sillitoe, R.V., and Hawkes, R. (2002). Whole-mount immunohistochemistry: a high-throughput screen for patterning defects in the mouse cerebellum. J Histochem Cytochem *50*, 235-244.

Smith, S.L., Smith, I.T., Branco, T., and Hausser, M. (2013). Dendritic spikes enhance stimulus selectivity in cortical neurons in vivo. Nature *503*, 115-120.

Solstad, T., Boccara, C.N., Kropff, E., Moser, M.B., and Moser, E.I. (2008). Representation of geometric borders in the entorhinal cortex. Science *322*, 1865-1868.

Sporns, O. (2013). Making sense of brain network data. Nat Methods *10*, 491-493.

Sporns, O., Tononi, G., and Kotter, R. (2005). The human connectome: A structural description of the human brain. PLoS Comput Biol *1*, e42.

Staffler, B., Berning, M., Boergens, K.M., Gour, A., van der Smagt, P., and Helmstaedter, M. (2017). SynEM, automated synapse detection for connectomics. Elife *6*, e26414.

Staubli, U., Gall, C., and Lynch, G. (1984a). The distribution of the commissural-associational afferents of the dentate gyrus after perforant path lesions in one-day-old rats. Brain Res *292*, 156-159.

Staubli, U., Ivy, G., and Lynch, G. (1984b). Hippocampal denervation causes rapid forgetting of olfactory information in rats. Proc Natl Acad Sci U S A *81*, 5885-5887.

Stensola, H., Stensola, T., Solstad, T., Froland, K., Moser, M.B., and Moser, E.I. (2012). The entorhinal grid map is discretized. Nature *492*, 72-78.

Steward, O., and Scoville, S.A. (1976). Cells of origin of entorhinal cortical afferents to the hippocampus and fascia dentata of the rat. The Journal of comparative neurology *169*, 347-370.

Stewart, M. (1999). Columnar activity supports propagation of population bursts in slices of rat entorhinal cortex. Brain Res *830*, 274-284.

Stuart, G., Schiller, J., and Sakmann, B. (1997). Action potential initiation and propagation in rat neocortical pyramidal neurons. The Journal of physiology *505 (Pt 3)*, 617-632.

Stuart, G.J., Dodt, H.U., and Sakmann, B. (1993). Patch-clamp recordings from the soma and dendrites of neurons in brain slices using infrared video microscopy. Pflugers Arch *423*, 511-518.

Stuart, G.J., and Sakmann, B. (1994). Active propagation of somatic action potentials into neocortical pyramidal cell dendrites. Nature *367*, 69-72.

Svoboda, K., Tank, D.W., and Denk, W. (1996). Direct measurement of coupling between dendritic spines and shafts. Science *272*, 716-719.

Swanson, L.W., and Cowan, W.M. (1977). An autoradiographic study of the organization of the efferent connections of the hippocampal formation in the rat. The Journal of comparative neurology *172*, 49-84.

Takacs, V.T., Klausberger, T., Somogyi, P., Freund, T.F., and Gulyas, A.I. (2012). Extrinsic and local glutamatergic inputs of the rat hippocampal CA1 area differentially innervate pyramidal cells and interneurons. Hippocampus *22*, 1379-1391.

Tamamaki, N., and Nojyo, Y. (1993). Projection of the entorhinal layer II neurons in the rat as revealed by intracellular pressure-injection of neurobiotin. Hippocampus *3*, 471-480.

Tamamaki, N., and Nojyo, Y. (1995). Preservation of topography in the connections between the subiculum, field CA1, and the entorhinal cortex in rats. The Journal of comparative neurology *353*, 379-390.

Tang, Q., Brecht, M., and Burgalossi, A. (2014a). Juxtacellular recording and morphological identification of single neurons in freely moving rats. Nat Protoc *9*, 2369-2381.

Tang, Q., Burgalossi, A., Ebbesen, C.L., Ray, S., Naumann, R., Schmidt, H., Spicher, D., and Brecht, M. (2014b). Pyramidal and stellate cell specificity of grid and border representations in layer 2 of medial entorhinal cortex. Neuron *84*, 1191-1197.

Tang, Q., Burgalossi, A., Ebbesen, C.L., Sanguinetti-Scheck, J.I., Schmidt, H., Tukker, J.J., Naumann, R., Ray, S., Preston-Ferrer, P., Schmitz, D.*, et al.* (2016). Functional Architecture of the Rat Parasubiculum. J Neurosci *36*, 2289-2301.

Teles-Grilo Ruivo, L.M., and Mellor, J.R. (2013). Cholinergic modulation of hippocampal network function. Front Synaptic Neurosci *5*, 2.

Tsuji, S. (1998). Electron microscopic localization of acetylcholinesterase activity in the central nervous system: chemical basis of a catalytic activity of Hatchett's brown (cupric ferrocyanide) precipitate revealed by 3,3'-diaminobenzidine. Folia histochemica et cytobiologica *36*, 67-70.

Usrey, W.M., and Fitzpatrick, D. (1996). Specificity in the axonal connections of layer VI neurons in tree shrew striate cortex: evidence for distinct granular and supragranular systems. J Neurosci *16*, 1203-1218.

van Haeften, T., Baks-te-Bulte, L., Goede, P.H., Wouterlood, F.G., and Witter, M.P. (2003). Morphological and numerical analysis of synaptic interactions between neurons in deep and superficial layers of the entorhinal cortex of the rat. Hippocampus *13*, 943-952.

Varga, C., Lee, S.Y., and Soltesz, I. (2010). Target-selective GABAergic control of entorhinal cortex output. Nat Neurosci *13*, 822-824.

Wanner, A.A., Genoud, C., and Friedrich, R.W. (2016a). 3-dimensional electron microscopic imaging of the zebrafish olfactory bulb and dense reconstruction of neurons. Sci Data *3*, 160100.

Wanner, A.A., Genoud, C., Masudi, T., Siksou, L., and Friedrich, R.W. (2016b). Dense EM-based reconstruction of the interglomerular projectome in the zebrafish olfactory bulb. Nature neuroscience.

White, J.G., Southgate, E., Thomson, J.N., and Brenner, S. (1986). The Structure of the Nervous System of the Nematode Caenorhabditis elegans. Philos Trans R Soc Lond B Biol Sci *314*, 1-340.

Wimmer, V.C., Bruno, R.M., de Kock, C.P., Kuner, T., and Sakmann, B. (2010). Dimensions of a projection column and architecture of VPM and POm axons in rat vibrissal cortex. Cereb Cortex *20*, 2265-2276.

Winterer, J., Maier, N., Wozny, C., Beed, P., Breustedt, J., Evangelista, R., Peng, Y., D'Albis, T., Kempter, R., and Schmitz, D. (2017). Excitatory Microcircuits within Superficial Layers of the Medial Entorhinal Cortex. Cell Rep *19*, 1110-1116.

Witter, M.P. (2007). The perforant path: projections from the entorhinal cortex to the dentate gyrus. Prog Brain Res *163*, 43-61.

Witter, M.P., Groenewegen, H.J., Lopes da Silva, F.H., and Lohman, A.H. (1989). Functional organization of the extrinsic and intrinsic circuitry of the parahippocampal region. Prog Neurobiol *33*, 161-253.

Woolsey, T.A., and Van der Loos, H. (1970). The structural organization of layer IV in the somatosensory region (SI) of mouse cerebral cortex. The description of a cortical field composed of discrete cytoarchitectonic units. Brain Res *17*, 205-242.

Yasuda, M., and Mayford, M.R. (2006). CaMKII activation in the entorhinal cortex disrupts previously encoded spatial memory. Neuron *50*, 309-318.

Acknowledgements

First, I want to thank my supervisor, Prof. Dr. Michael Brecht, for his guidance into exciting scientific projects; curiosity and passion for scientific research; encouraging words; great patience; as well as the freedom to follow up on my own ideas.

Most of the work on the Connectomics project was conducted in the laboratory of Prof. Dr. Moritz Helmstaedter (MPI for Brain Research, Frankfurt), where I had the opportunity to learn so much about electron microscopes – thanks to all the lab members! And thank you Moritz for believing in the sorted synapses.

Further, I would like to express my gratitude to colleagues and friends who helped along the way:

Dr. Robert Naumann - a dedicated scientist, who taught me everything about neuroanatomy, and how to find the MEC.

Special thanks to Kevin Boergens, for his knowledge and experience with electron microscopes and creativity in solving technical challenges.

To Dr. Andrea Burgalossi - who introduced me into tracing experiments and had the extra enthusiasm available.

Brigitte Geue, Undine Schneeweiss, Juliane Steger, and Dr. Iris Wolf - for excellent technical assistance. Special thanks to Undine, who ensured that even the smallest brain samples were stained and aligned accurately.

Manuel Berning, Benedikt Staffler, and Emmanuel Klinger - for their push for image alignment.

Heiko Wissler – especially for great help in coordinating tracing students. His support ensured that every Hiwi got the right tasks at the right time and that Amira is still partly a myth to me.

Dr. Rajnish Rao – for comments and discussions (scientific and not) – always helpful, interested, and truly funny.

Andreea Neukirchner, Sylvia Kraus–Fernando, and Margret Franke for help with almost all problems.

The Brecht lab – for a great atmosphere, and continued hospitality for the renegade student returning from scientific exile.

Statement of Contribution

The relative contributions of the author of this doctoral thesis to the presented studies are stated in the following.

(1) Ray, S.*, Naumann, R.*, Burgalossi, A.*, Tang, Q.*, Schmidt, H.*, Brecht, M. „Grid-layout and theta-modulation of layer 2 pyramidal neurons in medial entorhinal cortex“, Science, 2014 (*: equally contributing first authors). This study was performed in a collaborative approach. The author of this thesis contributed to the visualization of pyramidal cell clusters (calbindin stainings), performed retrograde neuronal labelling experiments, and analysed the alignment of the calbindin grid to the parasubiculum, the probability of hexagonal arrangement, as well as the proximity of cholinergic boutons to calbindin-positive dendrites.

(2) Tang, Q., Burgalossi, A., Ebbesen, CL., Ray, S., Naumann R., Schmidt, H, Spicher, D., Brecht, M. “Pyramidal and stellate cell specificity of grid and border representations in layer 2 of medial entorhinal cortex”, Neuron 2014. The author of this thesis contributed the spine density measurements.

(3) Tang, Q., Burgalossi, A., Ebbesen, C.L., Sanguinetti-Scheck, J.I., Schmidt, H., Tukker, J.J., Naumann, R., Ray, S., Preston-Ferrer, P., Schmitz, D., Brecht, M. “Functional Architecture of the Rat Parasubiculum“, Journal of Neuroscience, 2016. The author of this thesis contributed to the anterograde tracing experiments.

(4) Schmidt, H., Gour, A., Straehle, J., Boergens, K.M., Brecht, M., Helmstaedter, M. „Axonal synapse sorting in medial entorhinal cortex“, Nature, 2017. The author of this thesis performed all experiments and analyses in this work, with contributions from A.G. to the P90 experiment, and with the exception of the numerical simulations, and co-wrote the paper.

Publications

Brecht, M., Ray, S., Burgalossi, A., Tang, Q., **Schmidt, H**. and Naumann, R. (2013). An isomorphic mapping hypothesis of the grid representation. Philos Trans R Soc Lond B Biol Sci. 369(1635):20120521.

Ray, S.*, Naumann, R.*, Burgalossi, A.*, Tang, Q.*, **Schmidt, H.***, Brecht, M. (2014). Grid-layout and theta-modulation of layer 2 pyramidal neurons in medial entorhinal cortex. Science 343:891-6.
* These authors contributed equally.

Tang, Q.*, Burgalossi, A.*, Ebbesen, C.L.*, Ray, S., Naumann, R., **Schmidt, H.**, Spicher, D., Brecht, M. (2014). Pyramidal and stellate cell specificity of grid and border representations in layer 2 of medial entorhinal cortex. Neuron 84:1191-1197.

Tang, Q., Burgalossi, A., Ebbesen, C.L., Sanguinetti-Scheck, J.I., **Schmidt, H.**, Tukker, J.J., Naumann, R., Ray, S., Preston-Ferrer, P., Schmidtz, D., Brecht, M. (2016). Functional architecture of the rat parasubiculum. Journal of Neuroscience 36 (7) 2289-2301.

Schmidt, H., Gour, A., Straehle, J., Boergens, K., Brecht, M., Helmstaedter, M. (2017). Axonal synapse sorting in medial entorhinal cortex. Nature 549 (7673):469-475.

Eigenständigkeitserklärung

Hiermit versichere ich, dass ich die vorliegende Arbeit selbständig verfasst und keine anderen als die angegebenen Quellen und Hilfsmittel verwendet habe. Ich erkläre, dass ich sämtliche in der Arbeit verwendeten fremden Quellen als solche kenntlich gemacht habe und gemäß den mir bekannten gängigen wissenschaftlichen Regeln korrekt zitiert habe. Ich bestätige, dass ich bei wörtlich übernommenen Aussagen bzw. bei unverändert übernommenen Grafiken als auch bei in eigenen Worten wiedergegebenen Aussagen bzw. von mir abgewandelten Grafiken anderer Autoren die Quelle angegeben habe. In dem Zusammengang muss nochmals betont werden, dass die in der vorgelegten Arbeit behandelten Themen und Ergebnisse bereits in wissenschaftlichen Zeitschriften veröffentlicht wurden. Aus diesem Grund sind Übereinstimmungen in Inhalt, Text und Abbildung zwangsläufig. Zu Beginn eines jeden Kapitels sowie bei jeder Abbildung wurde deshalb nochmals explizit darauf verwiesen, dass diese Ergebnisse bereits von mir zusammen mit anderen Autoren veröffentlicht wurden.

Ich habe diese Arbeit nicht anderweitig zu Prüfungszwecken vorgelegt und habe mich nicht anderwärts um einen Doktorgrad beworben. Des weiteren versichere ich, dass keine Zusammenarbeit mit gewerblichen Promotionsberatern stattgefunden hat. Bei Anfertigung der Arbeit wurden die Grundsätze der Humboldt-Universität zu Berlin zur Sicherung guter wissenschaftlicher Praxis eingehalten. Die dem Promotionsverfahren zugrundeliegende Promotionsordnung ist mir bekannt.

Datum:

Unterschrift: